DEVELOPMENT AND BENCHMARK OF AN ELECTROSTATIC PIC/MCC NUMERICAL CODE FOR SIMULATION OF GAS DISCHARGE PLASMAS

A THESIS SUBMITTED TO
THE GRADUATE SCHOOL OF NATURAL AND APPLIED SCIENCES
OF
MIDDLE EAST TECHNICAL UNIVERSITY

BY

İBRAHİM ARDA

IN PARTIAL FULFILLMENT OF THE REQUIREMENTS
FOR
THE DEGREE OF MASTER OF SCIENCE
IN
PHYSICS

JANUARY 2023

Approval of the thesis:

DEVELOPMENT AND BENCHMARK OF AN ELECTROSTATIC PIC/MCC NUMERICAL CODE FOR SIMULATION OF GAS DISCHARGE PLASMAS

submitted by **İBRAHİM ARDA** in partial fulfillment of the requirements for the degree of **Master of Science in Physics Department, Middle East Technical University** by,

Prof. Dr. Halil Kalıpçılar
Dean, Graduate School of **Natural and Applied Sciences**

Prof. Dr. Seçkin Kürkcüoğlu
Head of Department, **Physics**

Prof. Dr. İsmail Rafatov
Supervisor, **Physics, METU**

Examining Committee Members:

Prof. Dr. Nevsan Şengil
Astronautical Engineering, UTAA

Prof. Dr. İsmail Rafatov
Physics, METU

Assoc. Prof. Dr. Mehmet Atakan Gürkan
Physics, METU

Date:10.01.2023

I hereby declare that all information in this document has been obtained and presented in accordance with academic rules and ethical conduct. I also declare that, as required by these rules and conduct, I have fully cited and referenced all material and results that are not original to this work.

Name, Surname: İbrahim Arda

Signature :

ABSTRACT

DEVELOPMENT AND BENCHMARK OF AN ELECTROSTATIC PIC/MCC NUMERICAL CODE FOR SIMULATION OF GAS DISCHARGE PLASMAS

Arda, İbrahim
M.S., Department of Physics
Supervisor: Prof. Dr. İsmail Rafatov

January 2023, 104 pages

This work deals with the development of the Particle-in-Cell/Monte Carlo Collision (PIC/MCC) numerical code for simulations of gas discharge plasmas. The study of these discharges is stimulated by various scientific and technological applications, which include surface modification, etching, lasers, spacecraft thrusters, plasma displays, and biomedicine. The efficient adoption of these discharges as sources of plasma for these applications depends on the ability to control plasma properties in the relevant systems. This implies a knowledge of the dependence of plasma properties in these systems on external factors (such as the amplitude and frequency of the applied voltage, nature, pressure and flow rate of the gas, geometry of the discharge setup, etc.). Such knowledge can be gained from the numerical modelling of the processes occurring in the gas discharge plasmas.

The present work includes development of the Particle-in-Cell (PIC) module of the numerical code and its application to the simulation of two-stream instability arising in the system of two cold electron beams travelling in opposite directions. Next, the Monte-Carlo Collision (MCC) module is developed and verified by its application to the simulation of an electron swarm in a steady-state Townsend discharge. Then, PIC and MCC modules are combined into a self-consistent PIC/MCC numerical code, which is first verified with the simulation of a radiofrequency capacitively coupled plasma (RF CCP) in argon. Finally, this code is benchmarked with simulations of a low-pressure RF CCP in helium.

Keywords: Gas discharge, low-temperature plasma, PIC/MCC, RF CCP

ÖZ

GAZ DEŞARJ PLAZMALARI BENZETİMİ İÇİN ELEKTROSTATİK BİR PIC/MCC SAYISAL KODUNUN GELİŞTİRİLMESİ VE KIYASLANMASI

Arda, İbrahim
Yüksek Lisans, Fizik Bölümü
Tez Yöneticisi: Prof. Dr. İsmail Rafatov

Ocak 2023 , 104 sayfa

Bu çalışma gaz deşarj plazmalarının benzetimleri için Hücrede Parçacık/Monte Carlo Çarpışma (PIC/MCC) sayısal kodunun geliştirilmesini ele almaktadır. Bu deşarjların çalışılması, yüzey modifikasyonu, dağlama, lazerler, uzay aracı iticileri, plazma ekranları ve biyotıp gibi çeşitli bilimsel ve teknolojik uygulamalarla teşvik edilmektedir. Bu uygulamalar için plazma kaynakları olarak bu deşarjların verimli bir şekilde uyarlanması, ilgili sistemlerde plazma özelliklerini kontrol etme yeteneğine bağlıdır. Bu, plazma özelliklerinin bu sistemlerdeki dış etkenlere (uygulanan gerilimin genliği ve frekansı, gazın türü, basıncı ve akış hızı, deşarj düzeneğinin geometrisi vb.) bağlılığın bilinmesi anlamına gelir. Bu bilgi ise gaz deşarj plazmalarında meydana gelen süreçlerin sayısal modellemesinden elde edilebilir.

Mevcut çalışma, sayısal kodun Hücrede Parçacık (PIC) modülünün geliştirilmesini ve bu modülün zıt yönlerde hareket eden iki soğuk elektron demeti sisteminde ortaya çıkan iki akım kararsızlığının benzetimine uygulanmasını içermektedir. Ardından, Monte Carlo Çarpışma (MCC) modülü geliştirilmiştir ve kararlı durumdaki Townsend deşarjında elektron sürüsü benzetimine uygulanarak doğrulanmıştır. Daha sonra, PIC ve MCC modülleri, ilk olarak radyofrekans kapasitif bağlaşımlı argon plazma (RF CCP) benzetimi ile doğrulanan öz uyumlu PIC/MCC sayısal kodunda birleştirilmiştir. Son olarak, bu kod düşük basınçlı helyum RF CCP benzetimleri ile kıyaslanmıştır.

Anahtar Kelimeler: Gaz deşarj, düşük sıcaklıklı plazma, PIC/MCC, RF CCP

To my beloved ones

ACKNOWLEDGMENTS

First and foremost, I would like to express my sincerest thanks to my supervisor Professor İsmail Rafatov for always kindly guiding me. Our meetings have always been instructive and fun to me. Thanks to the physical intuition he gave me in these meetings, I was able to progress by solving the problems I was stuck with.

I am also grateful to the examining committee members Professor Nevsan Şengil and Dr. Mehmet Atakan Gürkan for their valuable comments and suggestions regarding my thesis study.

Special thanks to Professor Tahsin Çağrı Şişman for encouraging me to pursue an M. S. degree in physics. He has made important contributions to my academic life, starting with my undergraduate education.

I am grateful to all of the professors who taught the courses I took during my graduate studies at METU's Department of Physics for everything they contributed. I would also like to express my gratitude to Professor İsmail Turan for his assistance with the department's scientific preparation program.

I am thankful to all of my colleagues, especially my superiors Professor Nevsan Şengil and Professor Uğur Murat Leloğlu, for their support and tolerance during my thesis study.

Lastly, I am deeply grateful to my dear family —my mother, father, and brother —for their endless love, faith and support.

TABLE OF CONTENTS

ABSTRACT v

ÖZ vii

ACKNOWLEDGMENTS x

TABLE OF CONTENTS xi

LIST OF TABLES xiv

LIST OF FIGURES xvi

LIST OF ABBREVIATIONS xix

CHAPTERS

1 INTRODUCTION 1

  1.1 The Basics of Plasmas and Discharges 1

    1.1.1 Plasma Frequency 2

    1.1.2 Debye Length 3

    1.1.3 Degree of Ionization 7

    1.1.4 Magnetization in Plasma 8

    1.1.5 Plasma Energy 9

    1.1.6 Practical Interest of GDPs 12

  1.2 Simulation Approaches of GDPs 13

    1.2.1 Kinetic and Particle Models 13

1.2.2 Fluid Models 14

1.2.3 Hybrid Models 15

1.3 An Overview of the Origin and Development of the PIC/MCC Method 15

1.4 Motivation and the Outline of the Thesis 19

2 DEVELOPMENT OF THE PIC MODULE AND ITS APPLICATION TO THE TSI PROBLEM 23

2.1 The Two-Stream Instability 23

2.2 The Basics of PIC Method 29

2.2.1 Particle Densities 30

2.2.2 Potential and Electric Field 33

2.2.3 Forces on Particles 34

2.2.4 Particle Motion 35

2.2.5 Boundary Effects 35

2.3 The PIC Simulation of TSI 36

2.4 Accuracy, Convergence, and Stability Conditions of PIC Simulations 43

3 DEVELOPMENT AND ANALYSES OF MONTE CARLO SIMULATION 45

3.1 Collision Probability 46

3.2 Monte Carlo Collision Method 50

3.3 Electron Transport in Steady State Townsend Discharge 56

4 PIC/MCC SIMULATIONS OF RADIOFREQUENCY CAPACITIVELY COUPLED PLASMA 63

4.1 Modelling of RF CCP and the Need for A Kinetic Model 63

4.2 Ion-Neutral Collisions 64

4.3 A Case Study: Comparison to eduPIC Single-Frequency RF CCP Simulation Results 65

4.4 Benchmarking the Code 71

5 CONCLUSIONS 81

LIST OF TABLES

TABLES

Table 1.1 Classification of GDPs [16]. 11

Table 2.1 Basic parameters of PIC simulation of TSI in [94]. Parameters are dimensionless. 37

Table 3.1 Parameters for SSTD simulation. 57

Table 3.2 Plasma-chemical model of the SSTD simulation. 59

Table 4.1 Basic parameters of single-frequency RF CCP simulation. 66

Table 4.2 Basic parameters of benchmark in [68]. 72

Table 4.3 Plasma-chemical model of the electron-neutral collisions in the benchmark study. 73

Table 4.4 Relative errors for some basic physical parameters of the discharge in comparison to reference values given in [68]. The values of the ion density n_i and the electron temperature T_e are evaluated at the centre of the discharge region. S_e and S_i are the line integrals of electrical power of electrons and ions through the discharge region, respectively. Ion current J_i is calculated at the grounded electrode. 73

Table 4.5 Relative errors for some basic numerical parameters of the discharge in comparison to reference values given in [68]. The time-averaged values are taken at the centre of the discharge, except N_P. N_P is the total number of super particles in the discharge region. 74

Table 4.6 The maximum relative errors in ion number densities with respect to the reference values from [68]. 77

Table 4.7 Comparison of X^2 values for the statistical distinguishability test with benchmark study from [68]. Given in the second line are the ranges of values that cover 99% of the area under the X^2 distributions given in [68]. 77

LIST OF FIGURES

FIGURES

Figure 1.1 Plasma slab for the description of plasma frequency and oscillations [4]. 2

Figure 1.2 Schematic of the PIC/MCC cycle introduced by the Berkeley simulation community [48]. 18

Figure 2.1 The cycle of the PIC procedure 29

Figure 2.2 Schematic of NGP method for particle weighting[66]. Particles effectively behave as rectangles. 30

Figure 2.3 Schematic of CIC method for particle weighting [66]. Particles effectively behave as triangles and thence the noises introduced by the rectangular shape of NGP method are smoothed. 32

Figure 2.4 Simulation results of Fitzpatrick's study [94] for electron phase space distributions at specified times. 38

Figure 2.5 Simulation results of current study for electron phase space distributions at specified times. 39

Figure 2.6 Initial and final electric field and potential profiles obtained from the TSI simulation of the present study. The parameters are dimensionless. 40

Figure 2.7 Initial and final electron density profiles and electron energy distribution functions obtained from the TSI simulation of the present study. The parameters are dimensionless. 41

Figure 2.8 Phase space distributions for $v_0 = 20$ at times $t = 0$, $t = 160$, and $t = 320$. TSI formation is not observed at such high speeds, as it was expected by the analytical solution. 41

Figure 2.9 Phase space distributions for $v_0 = 3$ and $v_{th} = 10^{-6}$ at times $t = 0$, $t = 10$, and $t = 17.5$. 42

Figure 2.10 Initial and final electric field and electron density profiles obtained from the TSI simulation of the present study for $v_{th} = 10^{-6}$. . . . 42

Figure 3.1 Intervals of collisional processes. P_j is the probability for the j-th process, calculated from Eq. (3.23). The processes are arranged in ascending order of threshold energies, from lowest to highest. If the random number R falls into the shown interval, then the l-th collisional process occurs. 51

Figure 3.2 Spherical coordinates used in SSTD study 58

Figure 3.3 Computed transport parameters in comparison to those from [95] 60

Figure 3.4 Error bars are utilized to obtain the maximum relative errors in transport parameter results in comparison to results from [95]. Error bars correspond to 15% of the data obtained in the thesis study. 61

Figure 3.5 Electron VDFs at various positions of discharge region obtained from SSTD simulations of this thesis study. The scales of color bars are logaritmic. 62

Figure 3.6 Electron VDFs at various regions of the discharge obtained from the simulations in [95]. 62

Figure 4.1 The evolution of superparticles against RF cycles as compared to the results from [87]. 67

Figure 4.2 Time-averaged electron and ion number densities with respect to the position in discharge region as compared to the results from [87]. 68

Figure 4.3 Time-averaged distribution functions of electrons and ions. EEPF is binned with 2000 data points corresponding to a resolution of 0.05 eV, whereas IFEDF is binned with 200 data points corresponding to a resolution of 1 eV as in [87]. Discharge conditions are given in Table 4.1. 69

Figure 4.4 The spatio-temporal distributions of the (a) electron number density (n_e), (b) ion number density (n_i), (c) potential (Φ), (d) electric field (E), (e) electron current density (j_e), (f) ion current density (j_i), (g) electron power density (P_e), (h) ion power density (P_i), (i) electron mean energy $(\langle\varepsilon_e\rangle)$, (j) ion mean energy $(\langle\varepsilon_i\rangle)$, and (k) rate of ionization $(R_{ion.})$ obtained in the present study. On the horizontal axis is the time through one RF period and on the vertical axis is the distance from the powered electrode. The discharge conditions are given in Table 4.1. 70

Figure 4.5 Time evolution of number of superparticles. 75

Figure 4.6 Distribution of ion number densities in comparison to results from [68]. 76

Figure 4.7 Temporally averaged ionization source terms in comparison to results from [68]. 78

Figure 4.8 Temporally averaged electron power densities in comparison to results from [68]. 79

Figure 4.9 Temporally averaged ion power densities in comparison to results from [68]. 79

Figure 4.10 Temporally and spatially averaged electron energy probability functions in comparison to results from [68]. 80

LIST OF ABBREVIATIONS

1D	1 Dimensional
Ar	Argon
BE	Boltzmann Equation
CCP	Capacitively Coupled Plasma
CFL	Courant-Friedrichs-Lewy
CIC	Cloud-In-Cell
CoM	Centre of Mass
COVID-19	Coronavirus Disease of 2019
DC	Direct Current
EEDF	Electron Energy Distribution Function
EEPF	Electron Energy Probability Function
EOM	Equations of Motion
FFT	Fast Fourier Transform
GDP	Gas Discharge Plasma
GPU	Graphics Processing Unit
He	Helium
HPC	High Performance Computing
ICP	Inductively Coupled Plasma
IFEDF	Ion Flux-Energy Distribution Function
LAB	Laboratory
LTE	Local Thermal Equilibrium
LTP	Low-Temperature Plasma
LUT	Lookup Table
MCC	Monte Carlo Collision

MKL	Math Kernel Library
MPI	Message Passing Interface
NGP	Nearest Grid Point
PC	Personal Computer
PIC	Particle-In-Cell
PM	Particle-Mesh
RF	Radiofrequency
RK4	The Fourth-Order Runge-Kutta Method
SSTD	Steady-State Townsend Discharge
TFLOPS	Tera Floating Point Operations per Second
TSI	Two-Stream Instability
VDF	Velocity Distribution Function

CHAPTER 1

INTRODUCTION

1.1 The Basics of Plasmas and Discharges

Plasma is a state of matter consisting of various charged and neutral particles. The term, which is a Greek word meaning *moldable substance*, was first introduced in a scientific context to describe a part of the blood by a Czech medical scientist, Jan Evangelista Purkynje [1]. In an attempt to explain the high frequency oscillations observed by him and his colleagues in their laboratory experiments, Irving Langmuir proposed using this term in 1928 [2] to describe the region of a strongly ionized gas with nearly equal numbers of charged particles. The first observations of the plasma phenomenon, however, were done even earlier and are attributed to William Crookes [3], who is the inventor of Crookes tubes —very early versions of discharge tubes.

Plasma is essentially an ionized gas, but unlike an ordinary gas, its dynamics are dominated by electromagnetic forces since a large number of charged particles are present. Another important feature of plasmas is that the number densities of electrons and positive ions are nearly equal in the bulk plasma away from the boundaries. So, while plasma is overall a neutral environment, the presence of charged particles reveals electromagnetic effects throughout the entire plasma. This property of plasmas is called *quasi-neutrality*. Owing to the quasi-neutrality, densities of charged particles can be equated to a common density called *plasma density*. That is, $n_e \simeq n_i \simeq n$, where n_e, n_i, and n_0 are electron, ion, and plasma densities, respectively.

Plasmas can be characterized according to several parameters, such as energy, Debye length, plasma frequency, degree of ionization, and whether they are magnetized or not. These characteristics have utmost significance in identifying plasma as a distinct state of matter and in classifying various types of plasma. Hence, it is worthwhile to elaborate on these characteristics in the following subsections.

1.1.1 Plasma Frequency

Plasma frequency is the fundamental time scale of a plasma and is defined as the plasma's response to electric field oscillations developing within the plasma. Consider a uniform and homogeneous plasma, and imagine that the electrons in some region of this plasma are displaced by a small distance Δx from their equilibrium positions. This leads to charge separation since ions are much less mobile than electrons. As a result, an electric field arises due to the imbalance of charges, and this field acts on electrons as a *restoring force*, pulling them back into their equilibrium positions. To describe this procedure quantitatively, consider a slab model given in Figure 1.1.

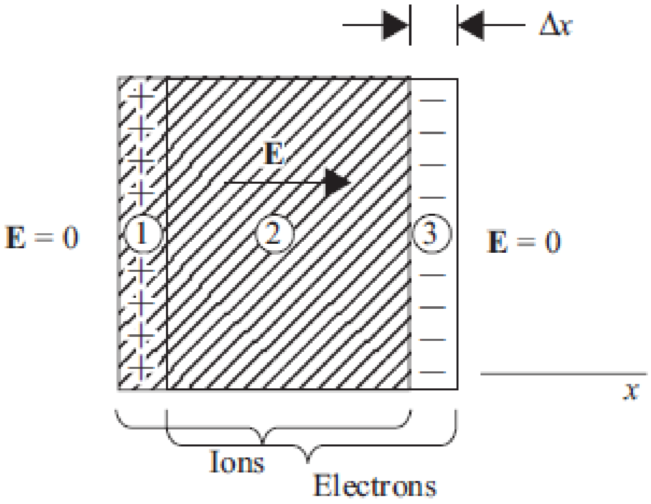

Figure 1.1: Plasma slab for the description of plasma frequency and oscillations [4].

Apparently, this model turns the situation into the problem of two parallel planes with equal but opposite charge densities. Recall from electrostatics that the electric field in region 2 in such a case is given by

$$\mathbf{E} = \frac{\sigma}{\varepsilon_0}\hat{\mathbf{x}}. \tag{1.1}$$

Here σ is the surface charge density and is given by $\sigma = en_0\Delta x$, where n_e is electron number density and e is the elementary charge. The Lorentz force relation is then used to obtain the equation of motion:

$$m_e \frac{\mathrm{d}^2 (\Delta x)}{\mathrm{d}t^2} = -eE_x, \tag{1.2}$$

where m_e is electron mass. Inserting the field from Eq. (1.1) into Eq. (1.2) and rearranging the equation yields

$$\frac{\mathrm{d}^2 (\Delta x)}{\mathrm{d}t^2} + \left(\frac{e^2 n_e}{\varepsilon_0 m_e}\right) \Delta x = 0. \tag{1.3}$$

Beware that Eq. (1.3) is the equation of a harmonic oscillator with frequency

$$\omega_e = \sqrt{\frac{e^2 n_e}{\varepsilon_0 m_e}}, \tag{1.4}$$

where ω_e and ε_0 are the plasma frequency and permittivity of free space, respectively. So, Eq. (1.4) gives the plasma frequency, which is the plasma's response to electric field oscillations that are shown to be in the form of harmonic oscillations in the above analysis. These oscillations were discovered by Tonks and Langmuir in 1929 [5]; thus, they are also called *Langmuir oscillations*. Observe that the plasma frequency depends only on the square root of electron density as the other terms in Eq. (1.4) are merely physical constants.

1.1.2 Debye Length

One of the fundamental characteristics of plasma is that it tends to shield itself against externally applied potential differences. To investigate this quantitatively, consider a test charge Q placed in a homogeneous plasma with electron density n_e and ion density n_i, and electron temperature T_e. Once the test charge is placed in the plasma, electrons and ions rearrange their positions, and the opposite charges of the test charge create a charge cloud around it. Then, the potential inside the plasma can be calculated through Poisson's equation:

$$\nabla^2\Phi = -\frac{\rho}{\varepsilon_0}, \tag{1.5}$$

where Φ is potential and ρ is charge density. The charge density in Eq. (1.5) can be written in terms of number densities as

$$\nabla^2\Phi = -\frac{e}{\varepsilon_0}\left(n_i - n_e\right). \tag{1.6}$$

For simplicity, it is reasonable to assume that ions are not moving. Considering the mass ratio of electrons and ions, this assumption makes sense, especially for short time scales such as in this case. Because of the quasi-neutrality, the ion density can then be equated to the plasma density; that is, $n_i = n_0$. Furthermore, far from the test charge, electron velocity distribution is assumed to be Maxwellian, with the potential and electron number density tending to zero and n_0, respectively. This distribution is given as [4]

$$f_e(v) = n_0\left(\frac{m_e}{2\pi k_B T_e}\right)^{3/2}\exp\left(-\frac{\frac{1}{2}m_e v^2 + q\Phi}{k_B T_e}\right), \tag{1.7}$$

where k_B is the Boltzmann constant, and T_e is electron temperature. Because according to the kinetic theory $n\left(\mathbf{x}, t\right) = \int_{-\infty}^{\infty} f\left(\mathbf{x}, \mathbf{v}, t\right) d\mathbf{v}$, integrating Eq. (1.7) over velocity space gives the electron number density in terms of Φ:

$$n_e = n_0\left(\frac{m_e}{2\pi k_B T_e}\right)^{3/2}\exp\left(-\frac{q\Phi}{k_B T_e}\right)\int_{-\infty}^{\infty}\exp\left(-\frac{m_e v^2}{2k_B T_e}\right) d^3v. \tag{1.8}$$

In Eq. (1.8), let $\beta \equiv m_e/(2k_B T_e)$ and divide the velocity in the integrand into its components to get for the integral term

$$\int_{-\infty}^{\infty}\exp\left(-\frac{m_e v^2}{2k_B T_e}\right) d^3v = \int_{-\infty}^{\infty} e^{-\beta v_x^2} dv_x \int_{-\infty}^{\infty} e^{-\beta v_y^2} dv_y \int_{-\infty}^{\infty} e^{-\beta v_z^2} dv_z. \tag{1.9}$$

Using the integral solution

$$\int_{-\infty}^{\infty} e^{-\beta\xi^2} d\xi = \frac{\sqrt{\pi}\,\mathrm{erf}(\sqrt{\beta}\xi)}{2\sqrt{\beta}}\bigg|_{-\infty}^{\infty} = \sqrt{\frac{\pi}{\beta}} \quad (\beta \geq 0) \tag{1.10}$$

in Eq. (1.9) gives

$$\int_{-\infty}^{\infty} \exp\left(-\frac{m_e v^2}{2k_B T_e}\right) d^3v = \left(\frac{2\pi k_B T_e}{m_e}\right)^{\frac{3}{2}}. \tag{1.11}$$

Once this inserted back into Eq. (1.8) along with $q = -e$, electron number density finally becomes

$$n_e = n_0 \exp\left(\frac{e\Phi}{k_B T_e}\right). \tag{1.12}$$

Then, using this expression of electron density in terms of the potential and the relation $n_i = n_0$ coming from the quasi-neutrality, Eq. (1.6) becomes

$$\nabla^2\Phi = -\frac{en_0}{\varepsilon_0}\left[1 - \exp\left(\frac{e\Phi}{k_B T_e}\right)\right]. \tag{1.13}$$

Eq. (1.13) is a nonlinear differential equation. In order to solve it for the potential, the exponential term can be expanded in a Taylor series, and the second and higher-order terms can be disregarded by assuming that $(e\Phi/k_B T_e) \ll 1$:

$$\nabla^2\Phi = -\frac{en_0}{\varepsilon_0}\left[1 - \left(1 + \frac{e\Phi}{k_B T_e}\right)\right], \tag{1.14}$$

and

$$\nabla^2\Phi = \frac{e^2 n_0}{\varepsilon_0 k_B T_e}\Phi. \tag{1.15}$$

It is easier to solve this equation by writing the Laplacian in spherical coordinates. This is because the isotropy of plasma [1] enables one to assume that the potential is

---

[1] Because magnetized plasmas are anisotropic, this assumption restricts the scope of the discussion to unmagnetized plasmas. A recent discussion of Debye length in magnetized plasmas can be found in [6].

spherically symmetric. Then, the angular derivative terms can be dropped and Eq. (1.15) becomes

$$\frac{1}{r^2}\frac{\partial}{\partial r}\left(r^2\frac{\partial \Phi}{\partial r}\right) = \frac{e^2 n_0}{\varepsilon_0 k_B T_e}\Phi. \tag{1.16}$$

Multiplying both sides of Eq. (1.16) by r and utilizing the equivalence

$$\frac{1}{r^2}\frac{\partial}{\partial r}\left(r^2\frac{\partial \psi}{\partial r}\right) \equiv \frac{1}{r}\frac{\partial^2}{\partial r^2}(r\psi) \tag{1.17}$$

on the left hand side of Eq. (1.16) yields

$$\frac{\partial^2}{\partial r^2}(r\Phi) - \frac{e^2 n_0}{\varepsilon_0 k_B T_e}(r\Phi) = 0. \tag{1.18}$$

The solution of Eq. (1.18) is

$$\Phi = \frac{1}{4\pi\varepsilon_0}\frac{Q}{r}e^{-r/\lambda_D}, \tag{1.19}$$

where the constant of the general solution is obtained from the condition that the solution should give the Coulomb potential of the test charge Q as r tends to zero. The term λ_D, on the other hand, is called the *Debye length* and is equal to

$$\lambda_D = \sqrt{\frac{\varepsilon_0 k_B T_e}{e^2 n_0}}. \tag{1.20}$$

As seen in Eq. (1.19), the Debye length acts as the length-scale of potential decay. So, the Debye length is actually a measure for the distance of shielding applied by plasma against the potential of test charge. From Eq. (1.20) the dependency of the Debye length on two factors can be deduced: electron temperature and plasma density. The product $k_B T_e$ appoints the extent of the charge cloud such that the particles with energies $\epsilon \gtrsim k_B T_e$ can escape the potential well created by the cloud. The boundaries of the cloud therefore coincide where the thermal energy of the particles is approximately equal to the potential energy. Thus, it is an expected result that the Debye length increases as the product $k_B T_e$ increases. By the way, the reason why electron temperature is used instead of ion temperature is that electrons are much more mobile than ions, and the charge cloud is basically formed by the movement of electrons. On the other hand, since plasma density is directly proportional to the number of electrons, it is straightforward that as plasma density increases, more and more electrons are contained in a given volume, and the shielding can be achieved over a shorter distance.

1.1.3 Degree of Ionization

The presence of charged particles plays a key role in the occurrence of various interesting features of plasmas, as has been discussed so far. The proportion of these charged particles with respect to the neutral particles is also important, especially in the collisional behaviour of plasmas. This proportion is determined by the *degree of ionization*, which can be defined as the ratio of the number density of charged particles to that of neutral particles. Since the quasi-neutrality requires $n_e \simeq n_i$, either the electron number density or the ion number density can be used to calculate this ratio:

$$\alpha = \frac{n_e}{n_e + n_n} \simeq \frac{n_i}{n_i + n_n}, \tag{1.21}$$

where α is the degree of ionization and n_n is the number density of neutral particles.

Depending on the plasma conditions, the degree of ionization can be well below 1% or almost 100%; however, very low values might be sufficient for a plasma to obtain a considerable amount of electrical conductivity. For instance, a plasma with $\alpha \simeq 0.1\%$ attains around half of its maximum conductivity, whereas $\alpha \simeq 1\%$ is sufficient for it to achieve its fully ionized conductivity level [7].

A plasma is usually identified as *weakly ionized* if the degree of ionization is below 10^{-4} and as *strongly ionized* otherwise [7]. In a *fully ionized* plasma, on the other hand, the ionization is complete. Examples of strongly and fully ionized plasmas include the solar wind, stellar interiors, and fusion plasmas, whereas high-pressure arcs, ionospheric plasmas, process plasmas, and gas discharge plasmas belong to the family of weakly ionized plasmas. Even though the progression from weakly to fully ionized plasma (and vice versa) is frequently abrupt [8], the distinction between the two is important since unless the plasma is weakly ionized, the collisions occurring between the charged particles dominate those occurring between the charged and neutral particles.

1.1.4 Magnetization in Plasma

If there is a sufficiently strong magnetic field in a plasma that affects the motions of charged particles significantly, then the plasma is said to be *magnetized*. The behaviour of a plasma in the presence of a magnetic field can be utterly different from that in an electrostatic medium. For instance, for a uniform magnetic field $\mathbf{B}$, it can be deduced from the Lorentz force equation that the charged particles undergo a circular motion in the plane perpendicular to $\mathbf{B}$, whereas the centres of these circles stream with no acceleration through the direction of $\mathbf{B}$. This motion is called a *gyro-motion* or *gyration*. The solutions of equations of motion for gyration yield a frequency expression [7]:

$$\omega_c = -\frac{qB}{m}, \tag{1.22}$$

where q and m are the charge and mass of the particle, B is the magnetic field strength, and ω_c is the *cyclotron frequency* (or *gyrofrequency*). The radius of the circular motion, on the other hand, is given by [7]

$$r_c = -\frac{mv_\perp}{qB} = \frac{v_\perp}{\omega_c}, \tag{1.23}$$

where $v_\perp$ is the component of particle velocity perpendicular to the magnetic field, and r_c is called *Larmor radius* (or *gyroradius*). Note that the cyclotron frequency and the Larmor radius are the characteristic time and length scales of a magnetized plasma. This indicates that processes occurring over far shorter time periods and at much shorter distances than the cyclotron frequency and the Larmor radius are virtually unaffected by the presence of a magnetic field. In that case, the plasma could be considered unmagnetized.

Furthermore, there might be some phenomena (e.g., in the magnetosphere layer of the Earth's atmosphere) for which the electrons are magnetized, whereas the ions are unmagnetized [9].

One of the most important features that make magnetized plasmas attractive for application is that the magnetic field can be used to confine the plasma and its species. The magnetic confinement of plasma has been an important part of fusion energy research, which has been seeking clean and environmentally friendly ways of energy production since the mid-20th century. A brief history and more detailed information about the fusion energy research can be found in, e.g., [10], [11].

1.1.5 Plasma Energy

The energy of a plasma is stored in the motions of plasma species occurring in various degrees of freedom, e.g., translation, rotation, vibration, and excitation. The state of plasma species can be described by a distribution function for each degree of freedom. For instance, in the case of kinetic energy, the velocity distribution function (VDF) $f\left(\mathbf{x}, \mathbf{v}, t\right)$ expresses the probability that a given species is located in position $\mathbf{x}$ with velocity $\mathbf{v}$ at time t. The shape of the VDF may take various forms depending on the homogeneity and isotropy of the velocity distribution. If a species of plasma has reached *thermal equilibrium*, its VDF attains a homogeneous and isotropic form called the Maxwell-Boltzmann distribution. The width of this distribution yields the temperature at which the thermal equilibrium is attained. In the case of a thermal equilibrium, the temperature is directly related to the average kinetic energy through the relation $E_{\text{av}} = \frac{1}{2}k_B T$ per degree of freedom [12]. Since plasmas consist of various species, they can have multiple temperature values. Actually, plasmas can also be classified based on their thermal equilibrium state. If the temperatures of all species of a plasma are the same, it is said to be in thermal equilibrium. The species of a plasma are sometimes in thermal equilibrium only locally. In that case, the term *local thermal equilibrium* (LTE) is used to describe the plasma. These plasmas are classified as *thermal plasmas*. In order to obtain thermal plasmas, either high temperatures (ranging from 4000 to 20000 K [13]) or high gas pressures are required. Thermal plasmas have some attractive features such as high temperature, high intensity nonionizing radiation and high-energy density [14]. Hence, they have a wide range of application areas including coating technology, fine powder synthesis, metallurgy applications such as welding and cutting, and treatment of hazardous waste materials [15].

When the temperatures of various species are different, the plasma is not in thermal equilibrium, and in this case it is described as a *non-local thermal equilibrium* (non-LTE) plasma. Non-LTE plasmas are also known as *cold plasmas*. Since electrons are the lightest and most mobile species, their energies are much higher than those of other species in a non-LTE plasma. One simple way to generate non-LTE plasma, among others, is to apply a potential difference through a gas. Even though gases are not conductive under normal conditions, there exist a very low number of charged particles all the time due to the effects of cosmic rays, radioactivity, ultraviolet radiation, etc. Because the ionization process caused by these effects is normally extremely low and rare, the gas remains an insulator medium. When, however, a sufficient amount of potential difference is applied, the charged particles accelerate under the effect of the electric field and may lead to additional ionization events. As the potential is increased beyond a certain point, an event called *breakdown* takes place and the gas becomes an electrically conducting medium; that is, a gas discharge plasma (GDP) is obtained. The necessary voltage for a breakdown to take place depends on various conditions, such as the gas pressure and the size of the discharge region. For conditions of gas pressure $p \approx 1$ Torr and of discharge region length $L \approx 1$ cm a few hundreds volts of potential difference might be necessary [16]. In fact, *Pashcen's law* gives the breakdown potential for various gases as a function of the product pL assuming a uniform electric field within the discharge region [16]:

$$V_b = \frac{BpL}{\ln\left[\frac{ApL}{\ln(1+1/\gamma))}\right]}, \tag{1.24}$$

where A, B and γ are constants whose values can be determined experimentally for various gases.

There exist a vast number of various types of GPDs; hence, going through all of them requires a whole, detailed study in itself. A rather detailed description of numereous

Table 1.1: Classification of GDPs [16].

State / Freq. Range	**Breakdown**	**Nonequilibrium Plasma**	**Equilibrium Plasma**
Constant Electric Field	Initiation of glow discharge in tubes	Positive column of glow discharge	Positive column of high-pressure arc
Radio Frequency	Initiation of RF discharge of rarefied gases	Capacitively coupled plasma (CCP) discharge	Inductively coupled plasma (ICP) torch
Microwave Range	Breakdown in waveguides and resonators	Microwave discharges in rarefied gases	Microwave plasmatron
Optical Range	Gas breakdown by laser radiation	Final stages of optical breakdown	Continuous optical discharge

types of discharges and their characteristics are already present in many textbooks, review articles and other resources, e.g., [13], [16]–[22]. A concise, convenient, and practical classification, however, can be made based on the two fundamental properties of GDPs: the state of the ionized gas and the frequency range of the field [16]. The former provides a subdivision for (i) breakdown, (ii) nonequilibrium and (iii) equilibrium stages, whereas the latter leads to (i) DC, low-frequency, and pulsed fields, (ii) radiofrequency fields (of frequencies about $10^5 - 10^8$ Hz), (iii) microwave fields (of frequencies about $10^9 - 10^{11}$ Hz and wavelengths about $10^2 - 10^{-1}$ cm), and (iv) optical fields (of frequencies from infrared to ultraviolet) [16]. Table 1.1 provides an overview of the typical circumstances for these classifications.

This thesis study focuses on unmagnetized GDPs that are weakly ionized and non-LTE. In such plasmas, collisions of the charged particles with neutral particles dominate. Hence, the collisions between the charged particles will be neglected. The main focus will be on radiofrequency capacitively coupled plasma (RF CCP) discharges, which are nonequilibrium plasmas as can be seen in Table 1.1. This means that electron dynamics, in particular, are nonlocal, discharge parameters are complicated, and distribution functions are highly anisotropic [23]. As a result, the correct description of such plasmas can only be obtained by kinetic methods, as will be discussed later in this study.

1.1.6 Practical Interest of GDPs

GDPs have a great number of application areas, such as surface modification, environmental applications, lasers, spacecraft thrusters, lamps, display technologies, biomedical technologies [22]. Surface modification applications of GDP have important usage especially in microelectronics. For instance, in the development of integrated circuits, GDP is used in some production steps such as film deposition, etching, resist development, and removal [24]. Surface modification techniques by GDP are also used in various parts of materials technology. The environmental applications of GDP include, for example, water treatment to obtain clean water by eliminating various harmful compounds in wastewater sources. A recent review [25] investigates the issue in detail and presents the advantages and disadvantages of the proposed techniques. GDPs can also be used in laser technology for the production of gas lasers. Common to various types of gas lasers, such as atomic, ion, and molecular lasers, is the use of GDP in producing the population inversion that is the necessary mechanism for laser activity [22]. Electric propulsion devices, such as ion thrusters, Hall-effect thrusters, pulsed plasma thrusters, etc., use GDP in a variety of ways to accelerate and eject heavy ions, transferring momentum to the spacecraft and allowing it to achieve thrust. Plenty of recently published review articles demonstrate the current states of various electric propulsion mechanisms, e.g. [26]–[32]. In the case of lamps, the fact that an excited atom emits light as a result of the de-excitation event is utilized to obtain a source of light. They might be categorized as electroded and electrodeless discharge lamps, both of which contain low-pressure and high-pressure types [22]. GDPs have also been increasingly used in biomedical technologies for purposes such as modifying the surfaces of biomedical polymers, sterilization of samples against various microorganisms, and accelerating the wound healing [22], [33]–[35]. The use of LTP technology against COVID-19 has also been investigated [33]. Eventually, it is not difficult to comprehend why GDP has been studied by numerous research groups and scientists throughout the world over the years given its diverse and wide range of applications.

1.2 Simulation Approaches of GDPs

Modeling and simulation are essential aspects of the study of GDPs. Various simulation approaches of GDP can be categorized in one of the following three models: fluid models, kinetic and particle models, and hybrid models.

1.2.1 Kinetic and Particle Models

Kinetic models are based on the solution of the Boltzmann equation (BE) given in Eq. (1.25) [36] for the velocity distribution function $f_j\left(\mathbf{r},\mathbf{v},t\right)$:

$$\frac{\partial f_j}{\partial t}+\nabla_r\cdot\mathbf{v}f_j+\frac{q_j}{m_j}\nabla_v\cdot\left[\left(\mathbf{E}+\mathbf{v}\times\mathbf{B}\right)f_j\right]=\sum_k C_k f_k. \tag{1.25}$$

Here, the subscript j points out the species of plasma. The term on the right-hand side of the equation includes all collisional effects through the operator C_k. The kinetic model provides the most exact solution, and it is inevitable to use it to obtain the correct description of the discharge, especially in the case of non-local plasma. However, it is a rather challenging task to solve the kinetic BE, primarily due to the complexity of the collisional terms and the high-dimensional structure of the equation. Thus, several simplifying assumptions are generally followed when possible. These include the elimination of the right-hand side all together for collisionless plasmas [37], the reduction of the six-dimensional BE to four-dimensional *Fokker-Planck equation* [38], and the simplification of the VDF into a form $f\left(\mathbf{r},\mathbf{v},t\right)=f_0\left(\mathbf{r},v,t\right)+f_1\left(\mathbf{r},v,t\right)\cos\theta$, where θ is the angle between the velocity of the particle and the electric field, which is called a *two-term approximation* [39], [40].

The particle method is another way to simulate GDP using a kinetic approach. The PIC/MCC model, specifically, introduces the idea of representing real particles by *superparticles*, each of which consists of a large number of real particles in a computer environment. The use of an appropriate computational grid, on the other hand, makes it unnecessary to consider the mutual interactions of every particle. Rather, physical parameters such as the potential and electric field are distributed onto the grid, and the forces on particles are calculated accordingly. The collisional interactions of the particles are accomplished stochastically through random numbers. One of the most attractive features of the PIC/MCC method is that distribution functions (either the velocity or energy distribution functions of electrons and ions) are the output of the method. Hence, neither a simplification nor an estimation of the shapes of these functions is required. However, they may become computationally quite demanding, even in one-dimensional problems. The PIC/MCC method is the main focus of this thesis study.

1.2.2 Fluid Models

The equations of fluid models are obtained from the velocity moments of BE. When Eq. (1.25) is integrated over the velocity space, the zeroth-order moment is taken and the continuity equation is obtained [36]:

$$\frac{\partial n_j}{\partial t} + \nabla \cdot (n_j \mathbf{u}_j) = S_j. \tag{1.26}$$

Here, $\mathbf{u}_j$ is the fluid velocity that is mass-averaged, and S_j is the term that accounts for the inelastic collisions, which effect the number of species j. If Eq. (1.25) is first multiplied by $\mathbf{v}$ and then integrated over the velocity space, then the first-order moment is taken and eventually the momentum conservation equation can be obtained [36]:

$$m_j n_j \frac{\mathrm{d}\mathbf{u}_j}{\mathrm{d}t} = q_j n_j \left(\mathbf{E} + \mathbf{u}_j \times \mathbf{B}\right) - \nabla p_j - \nabla \cdot \boldsymbol{\pi}_j + \mathbf{R}_j, \tag{1.27}$$

where m_j and q_j are the mass and charge of the species j, p_j is the partial pressure, $\boldsymbol{\pi}_j$ is a traceless pressure tensor where $\mathbf{P}_j = p_j \mathbf{1} + \boldsymbol{\pi}_j$, and $\mathbf{R}$ represents the rate of momentum exchange through collisions. Lastly, if Eq. (1.25) is first multiplied by v^2 and then integrated over the velocity space, the second-order moment is taken and it leads to the energy conservation equation [36]:

$$\frac{3}{2} n_j \frac{\mathrm{d}}{\mathrm{d}t} \left(k_B T_j \right) + p_j \nabla \cdot \mathbf{u}_j = -\boldsymbol{\pi}_j \cdot \nabla \mathbf{u}_j - \nabla \cdot \mathbf{q}_j + Q_j, \tag{1.28}$$

where k_B and T_j are the Boltzmann constant and the temperature such that $p_j = n_j k_B T_j$, $\mathbf{q}_j$ is the heat flow vector, and Q_j is the term that accounts for the collisions. So, Eqs. (1.26), (1.27), and (1.28) constitute the system of equations, which is actually not complete, for the species j in the fluid approach. To make this system a complete set, it is necessary that the functions $\boldsymbol{\pi}_j$, $\mathbf{R}_j$, $\mathbf{q}_j$, and Q_j are defined.

When compared to kinetic models, the fluid model is less complicated and has a much lower computational cost. The accuracy of the solution, however, is not always satisfying. The main condition that a discharge must meet for the fluid approach to be applicable is that the system size, L, be greater than the mean free path, λ, which is the average distance a particle travels between collisions.

1.2.3 Hybrid Models

Hybrid models bring together the desirable aspects of the kinetic and fluid models. Accordingly, only highly energetic particles are treated with the kinetic approach. These are usually fast electrons, but occasionally they can also be high-energy ions or neutral particles. Slow electrons and other low-energy particles are treated according to the fluid approach. The source terms accounting for the generation and annihilation of particles that are necessary in the fluid part are obtained from the kinetic part. As a result, the computational cost is reduced while maintaining the accuracy of fully kinetic models at an acceptable level. More detailed information about both the fluid and hybrid models can be found, e.g., in [41]–[45].

1.3 An Overview of the Origin and Development of the PIC/MCC Method

Plasma is one of the four fundamental states of matter, and the most of the known matter in the Universe consists of plasma. So, the idea of being able to develop and conduct simulation studies on such an important topic is fascinating and exciting. Thus, not surprisingly, the beginning of plasma simulation studies roughly coincides with the birth of the first programmable computers. In the literature, the first PIC studies were traced back to the late 1950s and the beginning of the 1960s by Buneman [46] and Dawson [47], even though particle methods had already been applied in the 1940s to trace particle motions in vacuum electronic devices by Hartree, Buneman, Nordsieck and others [48]. Obviously, the computational technologies were in their infancy, and the resources were limited at the time. Hence, certain simplifications were indispensable in order to implement simulations. For instance, the boundaries were disregarded by the assumption of periodic boundary conditions, and the forces between the particles were calculated through Coulomb's law, which greatly limited the number of particles that could be included in the model, along with the limitations arising from the low memories of hardware. Nevertheless, they successfully demonstrated basic plasma behaviour in one dimension and led the way for further and more advanced applications. In the following couple of years, the particle-mesh methods were introduced to reduce the number of operations required for the calculation of forces on particles. The number of operations for calculations of force through Coulomb's law in a system of N particles is N^2. So, as the number of particles increases, it becomes exceedingly computationally expensive for the code to conduct these calculations. For example, in their iconic book, Hockney and Eastwood [49] estimated the time required in such a case according to the computer circa 1978. Assuming a nominal time of $10\ \mu$s per each operation in a medium-sized computer, which were typically found at British universities at the time, only the force calculations for 10^5 particles per each time step would take about one month. On the other hand, using a typical particle-mesh method on the same computer for the same number of particles with 32 mesh points would reduce the computation time to only 45 seconds per each time step. This is a quite impressive example to demonstrate how the use of the particle-mesh approach led to a significant advance in plasma simulations. Thence, Dawson [50] verified the theoretical expectations of the effects of Landau damping on the thermal relaxations of a one-species and one-dimensional plasma through a simulation even before the experimental verifications. In 1965, Hockney published his article [51], in which he proposed a fast direct solution to the Poisson equation in two dimensions through Fourier analysis. This paved the way for two-dimensional simulations. By the end of the 1960s, the scope of the simulations was already broadened to include electromagnetic simulations for bounded plasma, e.g., [52] and [53]. One of the most important realizations about the nature of the plasma simulations was that the cross-sections of close-range Coulomb collisions were much less for the finite-size particles compared to point particles and that the Coulomb scattering events were taking place at small angles mostly [48]. That made it possible to develop simulations with much more particles through the utilization of clouds (finite-size particles). Some attempts to include collisions to simulations had already begun at the end of 1960s. Burger [54] introduced his paper in 1967 in which he included electron-neutral elastic collisions through a procedure that is quite similar to the methods followed by contemporary PIC/MCC codes. Birdsall [48] points out this study as the first PIC/MCC work. In the same year, Shanny *et al.* [55] published a paper demonstrating the *Lorentz gas model* where the collisions between electrons and ions were included through the implementation of MCC method. But it was computationally rather demanding to apply these procedures at that time with limited computational resources. Even with advanced technology, this is still true, and most of the time the MCC part is optimized with efficient algorithms. In 1968, Skullerud [56] introduced an algorithm, now known as *null-collision* method, that accelerated the MCC procedure. According to that, he introduced a fictitious collision procedure such that when the collision frequency of this procedure was added to the total collision frequency, it yielded a constant maximum collision frequency. So the time that passes between each collision event would be calculated much more efficiently. But even a more efficient algorithm of Skullerud's method introduced by Lin and Bardsley [57] in 1977. During that time period, the binary Coulomb collisions were also adapted to the simulations [58]–[60]. As the plasma simulation community appreciated the importance and the incomplete understanding of discharge boundaries, significant progress was achieved during the 1980s. Some notable studies of the late 1980s and the early 1990s can be found in [61]–[65]. Combined with all the knowledge from those notable studies, the Berkeley simulation community at the time gave the PIC/MCC model the form of approach that is still contemporary: propagate the field solver and the particle mover routines for a specified time step size, handle the collisions based on the probabilities calculated for each colliding particle during that time step, and calculate the post-collision velocities [48]. This sequence is summarized in Figure 1.2.

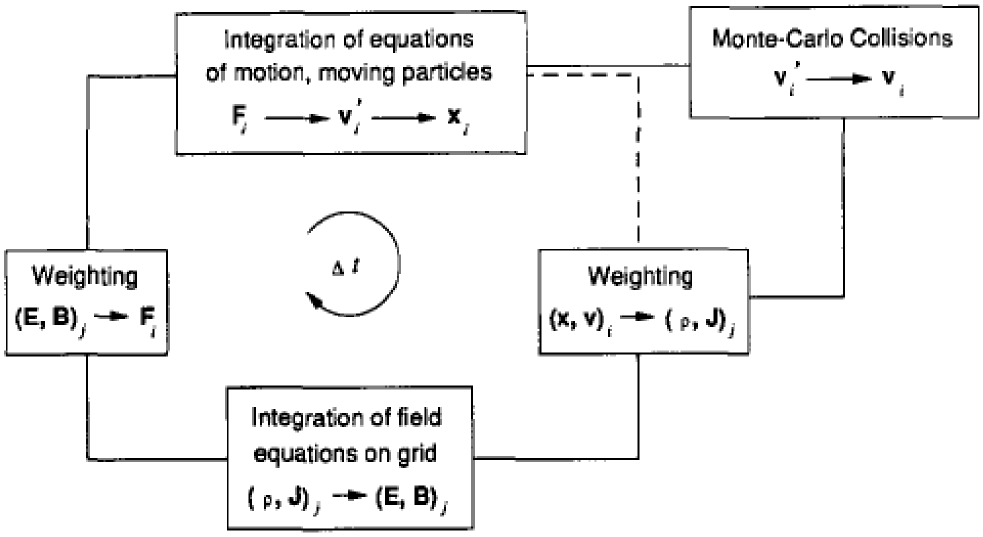

Figure 1.2: Schematic of the PIC/MCC cycle introduced by the Berkeley simulation community [48].

In 1988 Hockney and Eastwood [49], in 1991 Birdsall and Langdon [66] published the textbooks “Computer Simulation Using Particles” and “Plasma Physics via Computer Simulation”, respectively. These are canonical books and are still among the first-resorted resources for those initiating their studies in this field. In 1995, Surendra [67] published a very important pioneering benchmark study in which the studies of several researchers from a total of 13 institutions were involved. The methods and approaches of these participants include swarm parameters, experimental measurements, PIC/MCC method, fluid method, and hybrid method. Although according to Turner *et al.* [68] the codes involved in the study contained differences more than expected and the main reasons of those differences were unknown, it served well for the following studies for years.

The flourishing of the method continued into the new millennium, as well. With the progress of computational technologies, the method solidified and was applied to numerous problems in various fields, such as the electric propulsion for spacecraft [69]–[71], energy distribution of ions at the boundaries [72]–[76], electron power absorption [18], [77]–[80], resonance oscillations of plasma [81], [82], the afterglow dynamics [83], and the roles of the secondary electrons on discharge parameters [84]–[86].

It is worthwhile to specifically mention two studies that have important contributions to this thesis study. One is the benchmark study by Turner *et al.* [68]. It gives comprehensive and statistically rigorous results for the benchmarking of RF CCP in helium. The simulation results developed in various programming languages and architectures by researchers who have made significant contributions to this field are used to benchmark and verify the code developed in this thesis study. The other study to mention is the paper by Donkó *et al.* [87], in which they provided a clear and concise tutorial of the PIC/MCC method and also shared their programme code "eduPIC" with a thorough manual. It was quite helpful in the debugging process of the programme code developed in the current thesis study. One of the simulations given in their paper is also taken as a case study to verify the developed code, as well.

It is observed in the literature that there has been an increase in attention to massively parallel computing applications of PIC/MCC simulations through graphics processing units (GPUs) lately. Considering that the computation speeds can reach up to several TFLOPS [88], this is not surprising. Some recent studies with GPU based computations can be found in [88]–[92].

1.4 Motivation and the Outline of the Thesis

Although computationally demanding, the particle methods yield a quite detailed description of a GDP. In fact, if the discharge conditions bring about kinetic effects, it becomes inevitable to incorporate the kinetic approach into the solution. Fortunately, recent advances in computational capabilities, as well as ongoing improvements in the accessibility of high-performance computing tools (for example, Intel® HPC tools are now free for all), provide excellent support in the endeavour of developing more involved applications of kinetic models. Moreover, the accelerated uptrend in computational technologies seems to paint a bright picture about the future of this subject. On the other hand, LTP technologies continue to have a wide application area. In the most recent plasma roadmap about the low temperature plasma science and technology [33], the expressions of the U.S. National Academies of Sciences, Engineering, and Medicine [93] about the importance of the computational modeling of LTP are quoted as: “computational modeling capabilities are critically important in advancing LTP science and technologies”. All of these demonstrate that expertise in high-performance modeling, such as PIC/MCC, is a highly valued qualification in the field of LTP science and technology today and in the near future.

As the main objective of this thesis study is to develop a fully-kinetic PIC/MCC simulation code, it would be wise to begin with a simple problem and gradually add more complex procedures one at a time, validating each step along the way. The phenomenon of two-stream instability (TSI) serves well at that point as almost a canonical example of such a problem. TSI is an appropriate starting point for a couple of reasons. First of all, it is a kinetic phenomenon of plasma that incorporates non-Maxwellian distribution functions. This is desirable for the purpose of establishing a fully-kinetic PIC/MCC simulation. Furthermore, it can be simulated by cold streams of electron beams. This means that the simulation can be conducted by simplifying assumptions such as stationary background ions (i.e., the ions are not required to be considered as particles) and no collisions [94]. This is particularly useful as it enables us to validate the PIC procedure only prior to including the MCC procedure in the method. In this manner, Chapter 2 begins with a basic overview of TSI. The 1D electrostatic PIC simulation is then described step by step, developed and validated with the TSI problem given in [94]. Subsequently, the chapter is concluded with the accuracy, convergence, and stability conditions of PIC simulations.

The collision handling procedure is the main subject of Chapter 3. In this chapter, the concept of collision probability is introduced and discussed first. Then, the classical MCC method is explained in detail. As a performance improvement for the method, the *null-collision* procedure is also introduced. In order to test and verify the correct implementation of the MCC method, the problem of electron transport in steady-state Townsend discharge (SSTD), which is studied in [95], concludes the chapter.

In Chapter 4, the PIC/MCC numerical code is developed and the method is expanded with the inclusion of ion-neutral collisions. Then the code is implemented for the capacitively coupled radio frequency argon simulation that is studied in [87] as a case study. Then, the code is verified and validated through the benchmark study given in [68].

Finally, the conclusions of the thesis are listed in Chapter 5.

CHAPTER 2

DEVELOPMENT OF THE PIC MODULE AND ITS APPLICATION TO THE TSI PROBLEM

2.1 The Two-Stream Instability

The two-stream instability (TSI) is one of the well-known instabilities that may occur in plasma waves whose velocity distribution is non-Maxwellian. TSI is a kinetic phenomenon of plasma and it can be studied analytically through linearized Vlasov equation. To that end, consider high-frequency electrostatic plasma waves, which are also known as Langmuir waves. These are actually the propagating oscillations of electron densities resulting from the rapid response of electrons to the restoring forces arising from perturbing effects. The ions are rather massive compared to electrons, so for high-frequency oscillations the ions may be treated as stationary. For simplicity, consider the waves propagating along the x direction in an unmagnetized plasma, i.e., 1D plane electrostatic waves, that can be written in a scalar form as

$$E(x,t) = \mathcal{E} e^{i(kx-\omega t)}, \tag{2.1}$$

where $\mathcal{E}$, ω and k are the amplitude, frequency and the wave number of the wave, respectively.

For a given electron distribution function f, the Vlasov equation for such a plasma wave is given in scalar form as

$$\frac{\partial f}{\partial t} + v\frac{\partial f}{\partial x} - \frac{eE}{m_e}\frac{\partial f}{\partial v} = 0, \tag{2.2}$$

where m_e is electron mass, and e is the elementary charge.

Further assume that the wave oscillations and perturbations are small. Then

$$f\left(x,v,t\right) = f_0\left(v\right) + f_1\left(x,v,t\right), \tag{2.3}$$

where $f_0(v)$ is the equilibrium distribution, and f_1 is the small perturbation around the equilibrium distribution. For high-frequency small oscillations, it is reasonable to assume that the equilibrium distribution is spatially uniform since the amplitudes are rather small. Inserting Eq. (2.3) into the Vlasov equation, given in Eq. (2.2), yields

$$\frac{\partial}{\partial t}\left(f_0 + f_1\right) + v\frac{\partial}{\partial x}\left(f_0 + f_1\right) - \frac{eE}{m_e}\frac{\partial}{\partial v}\left(f_0 + f_1\right) = 0. \tag{2.4}$$

Since f_0 is only a function of velocity, $\partial f_0/\partial t = 0$ and $\partial f_0/\partial x = 0$. Then, Eq. (2.4) reduces to

$$\frac{\partial f_1}{\partial t} + v\frac{\partial f_1}{\partial x} - \frac{eE}{m_e}\frac{\partial}{\partial v}\left(f_0 + f_1\right) = 0. \tag{2.5}$$

Now, the term involving the multiplication of E and f_1 in Eq. (2.5) introduces a nonlinearity to the equation. Limiting our interest only on up to the first order terms, we can simply eliminate this second order nonlinear term to obtain a linearized form of the Vlasov equation as

$$\frac{\partial f_1}{\partial t} + v\frac{\partial f_1}{\partial x} - \frac{eE}{m_e}\frac{\partial f_0}{\partial v} = 0. \tag{2.6}$$

It is important to explicitly mention that, due to quasi-neutrality, the electric field is zero in the equilibrium state. The high-frequency (small-wave) electric field E emerges as a result of small perturbations. Furthermore, to obtain a self-consistent description, we need to couple the Maxwell equations to the system as well. For the problem at hand, however, it suffices to couple the Poisson equation:

$$\nabla \cdot \mathbf{E} = \frac{\rho}{\varepsilon_0}, \tag{2.7}$$

where ρ is the charge density and ε_0 is the permittivity of free space. Recall that in kinetic approach of plasma, the number density of particles, n, is represented by the distribution function:

$$n(\mathbf{x},t) = \int_{-\infty}^{\infty} f(\mathbf{x},\mathbf{v},t)\, d\mathbf{v}. \tag{2.8}$$

As the ions are assumed to be stationary in our analysis, only the electrons contribute significantly to oscillations in the charge density. The oscillating charge density is then given by

$$\rho = -e \int_{-\infty}^{\infty} f_1 dv, \tag{2.9}$$

and hence the Poisson equation becomes

$$\varepsilon_0 \frac{\partial E}{\partial x} = -e \int_{-\infty}^{\infty} f_1 dv. \tag{2.10}$$

So, the system now consists of the Eqs. (2.6) and (2.10). To solve this system of equations, Vlasov assumed a solution for f_1 in the same wave form as the electric field [96]:

$$f_1(x,v,t) = \mathcal{F}_1(v) e^{i(kx-\omega t)}. \tag{2.11}$$

Substituting wave form expressions of f_1 and E, given in Eq. (2.11) and Eq. (2.1) respectively, into the linearized Vlasov equation in Eq. (2.6) yields

$$-i\omega \mathcal{F}_1 e^{i(kx-\omega t)} + ikv\mathcal{F}_1 e^{i(kx-\omega t)} - \frac{e\mathcal{E}}{m_e}\frac{\partial f_0}{\partial v} e^{i(kx-\omega t)} = 0,$$

and hence

$$i(kv-\omega)\mathcal{F}_1 = \frac{e\mathcal{E}}{m_e}\frac{\partial f_0}{\partial v}.$$

Beware that for the given type of wave forms, the operators $\partial/\partial t$ and $\partial/\partial x$ simply act as multiplication by $-i\omega$ and ik, respectively. Rearranging this for $\mathcal{F}_1$ gives

$$\mathcal{F}_1 = \frac{ie\mathcal{E}}{m_e\left(\omega - kv\right)}\frac{\partial f_0}{\partial v}. \tag{2.12}$$

Putting this expression into the Poisson equation, Eq. (2.10), we have

$$ik\varepsilon_0\mathcal{E}e^{i(kx-\omega t)} = -e\int_{-\infty}^{\infty}\frac{ie\mathcal{E}}{m_e\left(\omega - kv\right)}\frac{\partial f_0}{\partial v}e^{i(kx-\omega t)}dv,$$

and

$$ik\varepsilon_0\mathcal{E}e^{i(kx-\omega t)} = -\frac{ie^2\mathcal{E}}{m_e}e^{i(kx-\omega t)}\int_{-\infty}^{\infty}\left(\omega - kv\right)^{-1}\frac{\partial f_0}{\partial v}dv.$$

Rearranging the terms, we have

$$i\left[k\varepsilon_0 + \frac{e^2}{m_e}\int_{-\infty}^{\infty}\left(\omega - kv\right)^{-1}\frac{\partial f_0}{\partial v}dv\right]\mathcal{E} = 0. \tag{2.13}$$

The non-trivial solution of this equation, after factoring out $k\varepsilon_0$, reads

$$1 + \frac{e^2}{m_e k\varepsilon_0}\int_{-\infty}^{\infty}\left(\omega - kv\right)^{-1}\frac{\partial f_0}{\partial v}dv = 0. \tag{2.14}$$

Eq. (2.14) is the *dispersion relation* for high-frequency electrostatic waves in an unmagnetized plasma according to the kinetic approach. The left-hand side of Eq. (2.14) is termed the *plasma dispersion function* and denoted as $\mathcal{D}(k,\omega)$.

Having obtained the dispersion relation, we now consider two electron beams traveling in opposing directions at the same speed, say $\pm v_0$. We can speak of a single speed value for a beam consisting of many particles because it is assumed that the thermal spread of electrons in the beam is negligible; that is, the beams are considered to be *cold*. Then, the velocity distribution function for these beams can be written as

$$f_0\left(v\right) = \frac{n}{2}\left[\delta\left(v - v_0\right) + \delta\left(v + v_0\right)\right]. \tag{2.15}$$

Here, $\delta(v)$ is the Dirac delta function, and n is the number density of electrons. We can now insert this distribution function into the dispersion relation in Eq. (2.14), but the integral would be rather complicated to solve. Hence, we first work on the integral term in Eq. (2.14) so that it becomes easier to deal with it. Integration by parts as $u \equiv (\omega - kv)^{-1}$ and $d\nu \equiv f_0$ yields,

$$\int_{-\infty}^{\infty} (\omega - kv)^{-1} \partial f_0 = \left. \frac{f_0}{\omega - kv} \right|_{v \to -\infty}^{v \to \infty} - \int_{-\infty}^{\infty} f_0 \frac{\partial}{\partial v} \left[(\omega - kv)^{-1} \right] dv.$$

The first term on the right hand side of this equation vanishes. Also, the partial derivative in the integrand of the right-hand side integral gives $\partial \left[(\omega - kv)^{-1} \right] / \partial v = k (\omega - kv)^{-2}$. Then,

$$\int_{-\infty}^{\infty} (\omega - kv)^{-1} \frac{\partial f_0}{\partial v} dv = -k \int_{-\infty}^{\infty} \frac{f_0}{(\omega - kv)^2} dv.$$

Further applying the property $\int_{-\infty}^{\infty} f(x) \delta (x - a)\, dx = f(a)$, and inserting the distribution function given in Eq. (2.15) into the above expression, we obtain

$$\int_{-\infty}^{\infty} (\omega - kv)^{-1} \frac{\partial f_0}{\partial v} dv = -\frac{kn}{2} \left[\frac{1}{(\omega - kv_0)^2} + \frac{1}{(\omega + kv_0)^2} \right].$$

Finally, substituting this for the integral term in Eq. (2.14), the dispersion relation for the given oppositely streaming beams become

$$\mathcal{D}(k, \omega) = 1 - \frac{ne^2}{2m_e \varepsilon_0} \left[\frac{1}{(\omega - kv_0)^2} + \frac{1}{(\omega + kv_0)^2} \right] = 0. \tag{2.16}$$

Recall that the characteristic plasma frequency for electron waves is $\omega_p^2 = ne^2/(\varepsilon_0 m_e)$. Rearranging Eq. (2.16) to include ω_p yields

$$\mathcal{D}(k, \omega) = 1 - \frac{1}{2} \left[\frac{\omega_p^2}{(\omega - kv_0)^2} + \frac{\omega_p^2}{(\omega + kv_0)^2} \right] = 0. \tag{2.17}$$

Eq. (2.17) is a fourth-order polynomial equation in parameters k and ω, which is also known as a *quartic* equation. To solve this quartic equation for ω, we rearrange it further by equalising the denominators to obtain

$$1-\omega_p^2\left(\frac{\omega^2+k^2v_0^2}{\omega^4-2\omega^2k^2v_0^2+k^4v_0^4}\right)=0,$$

and

$$\omega^4-\left(2k^2v_0^2-\omega_p^2\right)\omega^2+k^4v_0^4-\omega_p^2k^2v_0^2=0. \tag{2.18}$$

By letting $\chi\equiv\omega^2$, we can transform Eq. (2.18) into a quadratic equation, and thence obtain solutions readily. Accordingly, we get

$$\chi^2-\left(2k^2v_0^2-\omega_p^2\right)\chi+k^4v_0^4-\omega_p^2k^2v_0^2=0. \tag{2.19}$$

The discriminant of Eq.(2.19) is $\Delta=\omega_p^4$ and the solutions become

$$\begin{aligned}\chi_1&=k^2v_0^2-\omega_p^2,\\ \chi_2&=k^2v_0^2,\end{aligned}$$

from which the roots of ω are obtained as

$$\begin{aligned}\omega_1&=\sqrt{(k^2v_0^2-\omega_p^2)}, &\omega_2&=\left|kv_0\right|,\\ \omega_3&=-\sqrt{(k^2v_0^2-\omega_p^2)}, &\omega_4&=-\left|kv_0\right|.\end{aligned} \tag{2.20}$$

Observe from Eq. (2.20) that when $k^2v_0^2<\omega_p^2$, the frequency ω has two complex roots: $i\gamma$ and $-i\gamma$ corresponding to roots ω_1 and ω_3, respectively, where $\gamma\equiv\left|k^2v_0^2-\omega_p^2\right|^{1/2}$. Then, inserting ω_1 into Eq. (2.1) gives

$$E=\mathcal{E}e^{ikx}e^{\gamma t}. \tag{2.21}$$

Since $\gamma>0$, the waves grow exponentially as time passes. Hence, we conclude that the dispersion relation for the given distribution in Eq. (2.15) of two oppositely streaming beams suggests an instability for sufficiently long wavelengths. The physical picture, on the other hand, can be depicted as follows: upon the encounter of two oppositely streaming beams, electrons tend to gather and create spatial inhomogeneity if their oscillation frequencies are less than the plasma oscillation frequency. Subsequently, these electron bundles effectively dissipate their energies to the plasma waves and hence induce an instability, which is called the two-stream instability.

2.2 The Basics of PIC Method

The PIC method is one of the particle methods that belongs to the class of particle-mesh (PM) methods as identified by Hockney and Eastwood [49]. According to that, a spatial mesh is constructed into which some parameters (e.g., particle and charge densities) may be distributed according to various schemes. In this way, the continuous fields can be assigned to the grid points with discrete values and the forces can be calculated accordingly. The entire PIC procedure consists of several steps and the main algorithm constructs a cycle, as in Figure 2.1. All these steps are explained and detailed below.

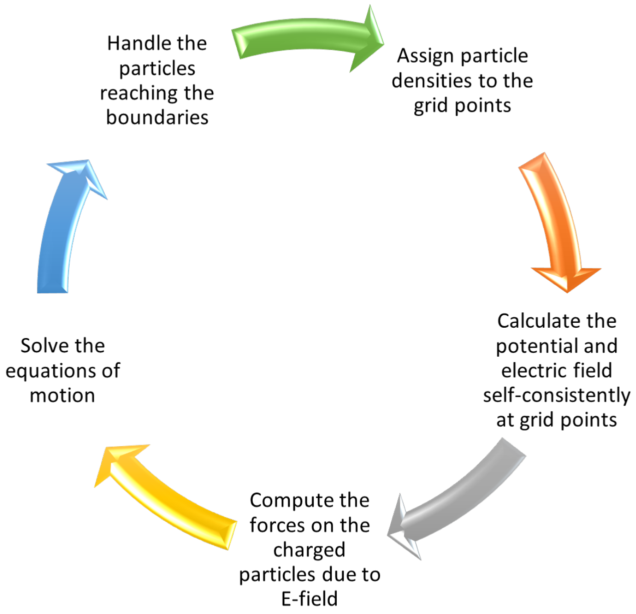

Figure 2.1: The cycle of the PIC procedure

2.2.1 Particle Densities

After the spatial mesh is constructed and the simulation is initialized according to the specific initial conditions of a given problem, the cycle starts with the assignment of charge densities to grid points. This stage is sometimes called particle weighting [66] (not to be confused with particle weight which controls the ratio between the number of real particles and superparticles). This can be achieved through several approaches; for instance, the total number of superparticles within the width of a cell could be counted at a grid point, which is called the *nearest grid point* (NGP) method and corresponds to the zero-order weighting [66].

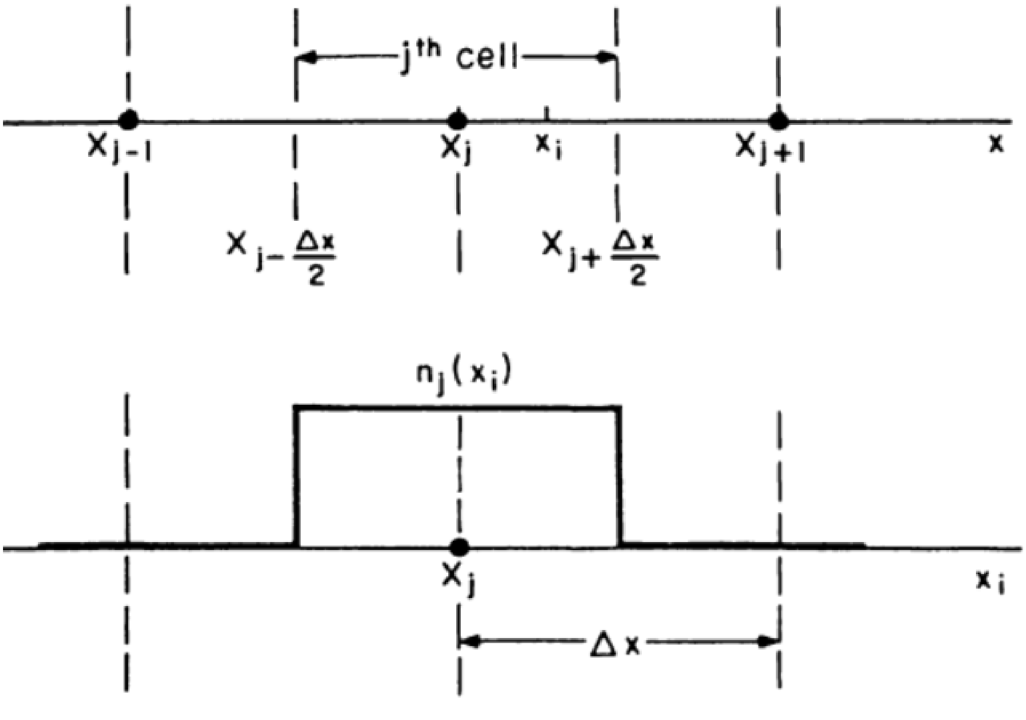

Figure 2.2: Schematic of NGP method for particle weighting[66]. Particles effectively behave as rectangles.

One immediate result emerging from this approach is that the particles effectively behave as if they had a rectangular shape of the width of a grid cell; that is, the superparticles are considered as finite-size particles. One may doubt the correctness of this approach, but since very close interactions occur rarely in a plasma and when the longe-range interactions dominate, this assumption does not significantly violate the validity of the model. The NGP method, however, introduces significant noises and fluctuations to the densities and thus to the calculation of potentials and fields as the rectangle-shaped superparticles pass through grid points. Hence, a better approach is the first-order weighting, in which the superparticles considered as triangular-shaped clouds whose charge is uniformly distributed within the cloud. This model is appropriately called the cloud-in-cell (CIC) model [97] . The visualizations of these two methods are given in Figures 2.2 and 2.3. For such a cloud with its centre point positioned at x_i, where x_i lies somewhere in between the grid points X_j and X_{j+1}, the assignment of number density to the grid points is done as follows according to the CIC model:

$$\delta n_j = \frac{X_{j+1} - x_i}{\Delta x} \frac{W}{A\Delta x}, \tag{2.22}$$

$$\delta n_{j+1} = \frac{x_i - X_j}{\Delta x} \frac{W}{A\Delta x}. \tag{2.23}$$

Here, W is the particle weight, A and Δx are the cross-sectional area and the length of each grid cell, respectively. The first quotient terms, $\frac{X_{j+1}-x_i}{\Delta x}$ and $\frac{x_i-X_j}{\Delta x}$, on the right hand side of Eqs. (2.22) and (2.23) correspond to the linear interpolation operation, whereas the second one, $\frac{W}{A\Delta x}$ on both equations, corresponds to the operation of converting the superparticles to real particle densities. Hence, considering the entire cloud as a single point particle with position x_i and interpolating its number density to the nearest grid points with the first-order (linear interpolation) approach would give an equivalent result. The latter approach is called the particle-in-cell (PIC) method and the assignment of number density is done as follows:

$$\delta n_j = \left[(j+1) - \frac{x_i}{\Delta x}\right] \frac{W}{A\Delta x}, \tag{2.24}$$

$$\delta n_{j+1} = \left(\frac{x_i}{\Delta x} - j\right) \frac{W}{A\Delta x}. \tag{2.25}$$

Further improvements can be obtained through higher-order methods, but the higher

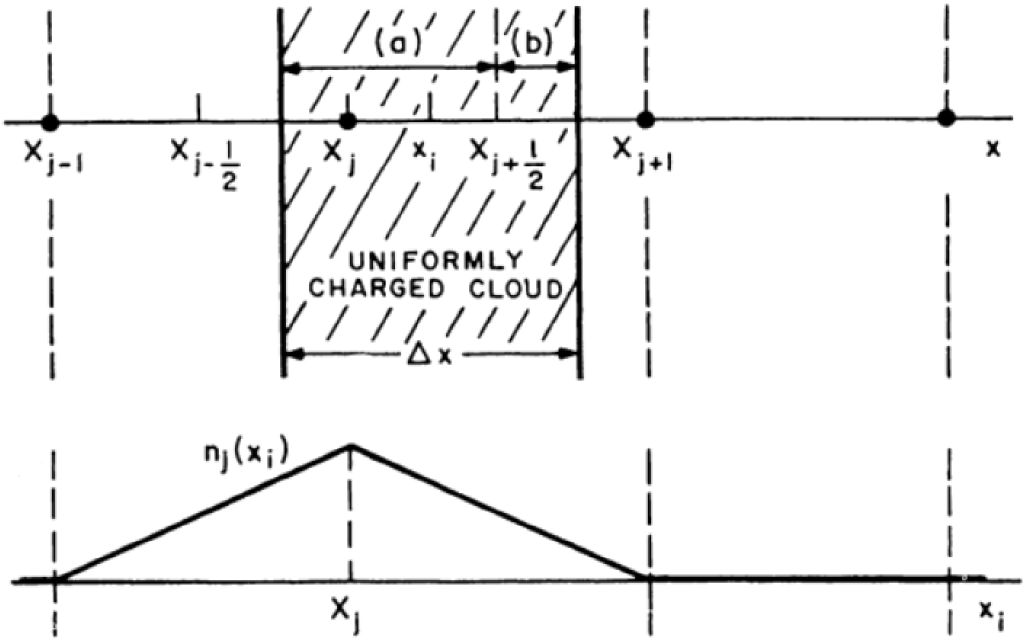

Figure 2.3: Schematic of CIC method for particle weighting [66]. Particles effectively behave as triangles and thence the noises introduced by the rectangular shape of NGP method are smoothed.

the order of the method, the more complicated and computationally expensive it becomes. Generally, the first-order method is sufficient and it will be used in this study.

When applied for all superparticles of each species, Eqs. (2.24) and (2.25) lead to the total number densities on grid points. If there are a total of M superparticles of species s which contribute to j-th grid point, the total number density of that species on that grid point is simply obtained by addition of each individual contribution:

$$n_{j,s} = \sum_{k=1}^{M} \delta n_{k,s}. \tag{2.26}$$

Consequently, the total charge density on j-th grid point becomes

$$\rho_j = \sum_{s} q_s n_{j,s}. \tag{2.27}$$

2.2.2 Potential and Electric Field

The presence of charged particles does modify the potential and electric field distributions within the discharge region. Hence, a comprehensive model shall consider this fact when solving the equations of motion (EOM). At this stage, Poisson's equation is coupled with the system to obtain a self-consistent description of the discharge. To this end, the Poisson equation needs to be discretized with a suitable model. Second order centered finite difference scheme is generally the choice for the internal nodes, which yields

$$\frac{\phi_{j-1} - 2\phi_j + \phi_{j+1}}{\Delta x^2} = -\frac{\rho_j}{\varepsilon_0}. \tag{2.28}$$

When put into a matrix form, Eq. (2.28) constitutes a tridiagonal system of equations. Thomas algorithm is usually used to solve such a system in 1D problems as its complexity is only $\mathcal{O}(n)$, where n is the number of equations in the system. The potentials on the electrodes, on the other hand, are included to the system as boundary conditions. After the tridiagonal system is solved and the solutions for potentials on the grid points are obtained, the electric field can be calculated through the relation $\mathbf{E} = -\nabla\phi$. This is also discretized through the second order centered finite difference scheme:

$$E_j = \frac{\phi_{j-1} - \phi_{j+1}}{2\Delta x}. \tag{2.29}$$

Eq. (2.29) shall only be applied to internal grids; grid points standing on the boundaries require special treatment as the centered finite differences would involve addition of non-existing grid points beyond boundaries. Let us pretend for a moment that these grid points beyond boundaries exist and apply the centered finite differences for boundary grid points. For $j = 0$, we obtain

$$E_0 = \frac{\phi_{-1} - \phi_1}{2\Delta x}. \tag{2.30}$$

If existed, the term ϕ_{-1} would have been obtained through Eq. (2.28) by letting $j = 0$.

Then, substituting the resulting expression into Eq. (2.30) would yield

$$E_0 = \frac{\phi_0 - \phi_1}{\Delta x} - \frac{\rho_0 \Delta x}{2\varepsilon_0}. \tag{2.31}$$

A similar treatment for the right boundary (for $j = N - 1$) gives

$$E_{N-1} = \frac{\phi_{N-2} - \phi_{N-1}}{\Delta x} + \frac{\rho_{N-1} \Delta x}{2\varepsilon_0}. \tag{2.32}$$

2.2.3 Forces on Particles

After the electric field distribution is obtained, it is possible to calculate the force exerted on particle i located at position x_i through Lorentz force equation (for $\mathbf{B} = \mathbf{0}$):

$$F_i = q_i E_i. \tag{2.33}$$

However, care must be taken that Eq. (2.33) requires the electric field at particle positions, and not at grid points. Thus, electric field values calculated at grid points should be interpolated back to particle positions. At this point, it is advised that an interpolation scheme should be used with the same order as that of used in distributing the particle densities to grid points, in order to prevent development of a self-force [66]. Consequently, the electric field at position x_i that falls within grid points j and $j + 1$ is expressed as:

$$E_i = E_j \frac{X_{j+1} - x_i}{\Delta x} + E_{j+1} \frac{x_i - X_j}{\Delta x}. \tag{2.34}$$

Thanks to PIC modelling, at this stage, we obtained self-consistent force acting on each particle without accounting for pair interactions of each and every particle, which would be a hopeless task indeed.

2.2.4 Particle Motion

Now that the forces are obtained, the EOM can be solved to move particles and obtain updated positions and velocities. Among various integration methods, explicit leapfrog integration [66], [98] is usually chosen as it is a simple yet second-order accurate method. In this method, the positions are calculated at usual (i.e., integer) time steps, whereas the velocities are calculated at half integer time steps:

$$v^{k+1/2} = v^{k-1/2} + \frac{q}{m} E^k \Delta t, \tag{2.35}$$

$$x^{k+1} = x^k + v^{k+1/2} \Delta t. \tag{2.36}$$

Observe from Eqs. (2.35) and (2.36), where the superscripts show time steps, that the position and velocity are not in phase in time for a given time step. Hence, the velocity is necessary to be propagated for a half step size, when the plasma state at a given time step is to be determined, for example. This can be accomplished through

$$v^{k+1} = v^{k+1/2} + \frac{qE^{k+1}}{m} \frac{\Delta t}{2}. \tag{2.37}$$

2.2.5 Boundary Effects

Boundary effects, in this context, point out interactions between boundary surfaces of the discharge region (i.e., electrodes, dielectric walls, etc.) and those particles reaching the surfaces. These interactions may be in a variety of ways. For example, particles may be absorbed by electrodes, reflected off of surfaces, or interact with surfaces to release new (secondary) particles. Reflection and secondary particle emission processes are stochastically included in PIC/MCC simulations through relevant coefficient values that depend on the material of boundary surfaces. Particle reflection and secondary particle emission processes may play significant roles on various discharge characteristics depending on the discharge conditions. Hence, it is important to perceive the extent of the study and include necessary boundary processes correctly. The effects of boundary processes for various discharge characteristics have been studied in the literature, e.g., [41], [99]–[103].

2.3 The PIC Simulation of TSI

There exist various PIC simulations of TSI in the literature, e.g., [49], [66], [94], [104]–[107]. Among those, Fitzpatrick's study [94] stands out as a rather useful and tractable introductory example. Hence, the first PIC simulation will be conducted for this study.

In Fitzpatrick's study [94], an electron distribution function for two oppositely streaming beams is given in the following form:

$$f\left(x, v\right) = \frac{n_0}{2\sqrt{2\pi} v_{th}} \left[e^{-(v-v_0)^2/2v_{th}^2} + e^{-(v+v_0)^2/2v_{th}^2} \right], \tag{2.38}$$

where n_0 is the uniform background ion density, v_{th} is the thermal spread of electron beams, and v_0 is the mean speed of each Maxwellian electron beam. Note that, even though the velocity distribution of each beam is Maxwellian on their own, the total resulting distribution function is non-Maxwellian. Moreover, the distribution function is normalized and the governing equations are non-dimensionalized for convenience. We also follow the same convention here for a better correspondence. Accordingly, the non-dimensionalized governing equations and the normalized distribution function takes the following forms:

$$\begin{aligned} \frac{\mathrm{d}x}{\mathrm{d}t} &= v, \\ \frac{\mathrm{d}v}{\mathrm{d}t} &= -E(x), \\ E(x) &= -\frac{\mathrm{d}\phi(x)}{\mathrm{d}x}, \\ \frac{\mathrm{d}^2\phi(x)}{\mathrm{d}x^2} &= \frac{n(x)}{n_0} - 1, \end{aligned} \tag{2.39}$$

and

$$f\left(x,v\right)=\frac{n_0}{2\sqrt{2\pi}}\left[e^{-(v-v_0)^2/2}+e^{-(v+v_0)^2/2}\right]. \tag{2.40}$$

Furthermore, periodic boundary conditions are utilized in [94], such that $n(0) = n(L)$, $\phi(0) = \phi(L)$, and $E(0) = E(L)$. This suggests that any particle reaching the boundaries may be rejoined to the simulation region from the opposite boundary. The parameters utilized in the simulation are given in Table 2.1.

Table 2.1: Basic parameters of PIC simulation of TSI in [94]. Parameters are dimensionless.

Parameter	**Symbol**	**Value**
Number of electrons	$n_{el.}$	2×10^4
Number of grid points	N_G	1000
Length of simulation region	L	100
Mean speed of beams	v_0	3
Time step size	δt	0.1

The simulation results of Fitzpatrick's study [94] for phase space distributions of electrons at various times are given in Figure 2.4. The same results from the simulation of the present study, on the other hand, are given in Figure 2.5, in the same format for direct comparison. In [94], the EOM of electrons are solved by the fixed step Runge-Kutta (RK4) method and the Poisson equation is solved by a 1D Fast Fourier Transform (FFT) algorithm. In the present study, however, the EOM are solved by the explicit leapfrog integrator, and the Poisson equation is solved by the 1D tridiagonal matrix algorithm. This way, it is possible to verify the correct use of the modules of these solvers prior to being used in a full-scale PIC/MCC code. Moreover, Fitzpatrick utilized rejection method [108] in generating randomly initialized velocity distributions, whereas the Gaussian Boxmuller method of the Mersenne-Twister 19937 generator of Math Kernel Library (MKL) of Intel Fortran® [109] is used for the same purpose in the present study.

In Figures 2.4 and 2.5, the characteristic circular clustering of particles in the phase space is readily observed. Even though some small differences exist between the

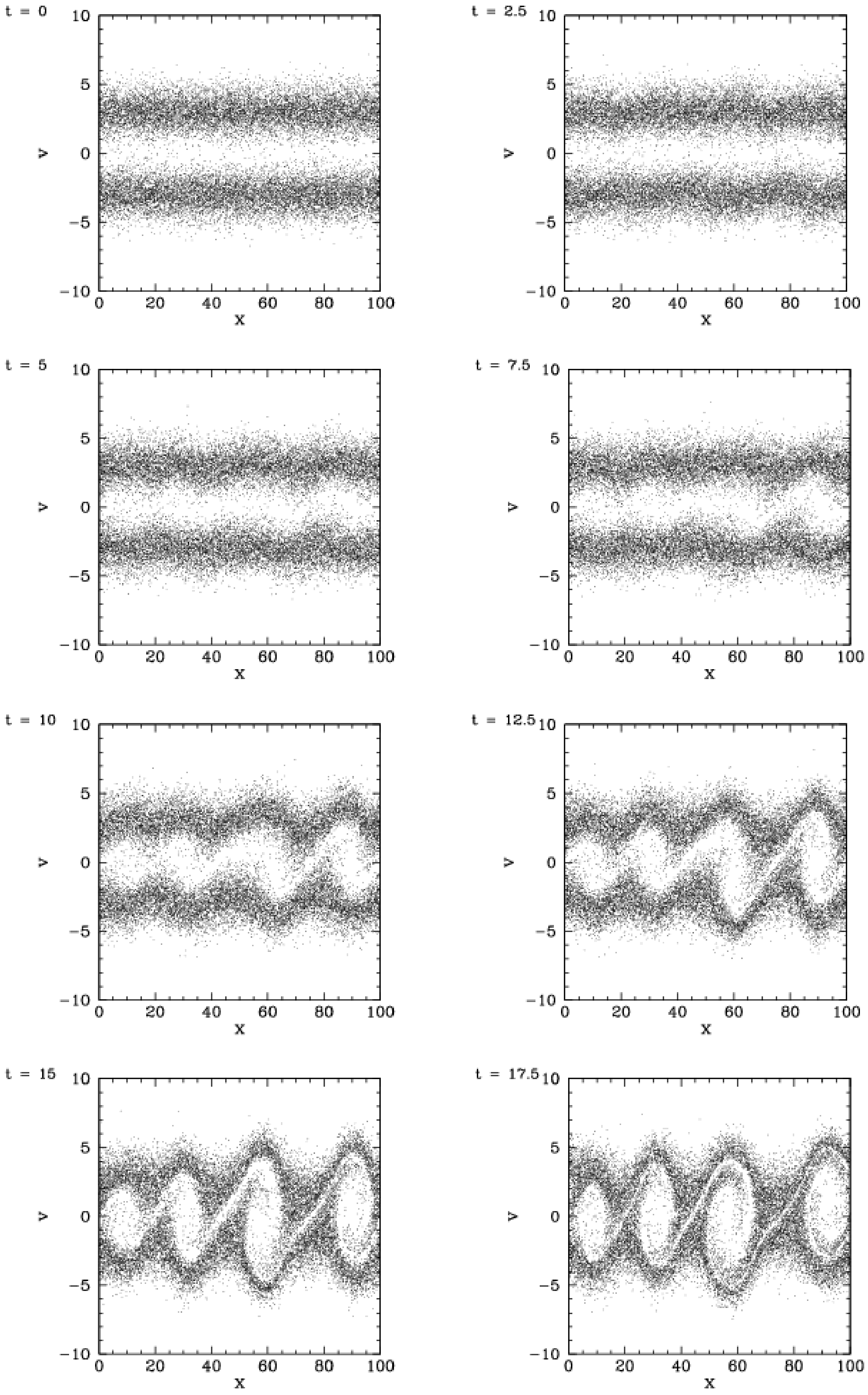

Figure 2.4: Simulation results of Fitzpatrick's study [94] for electron phase space distributions at specified times.

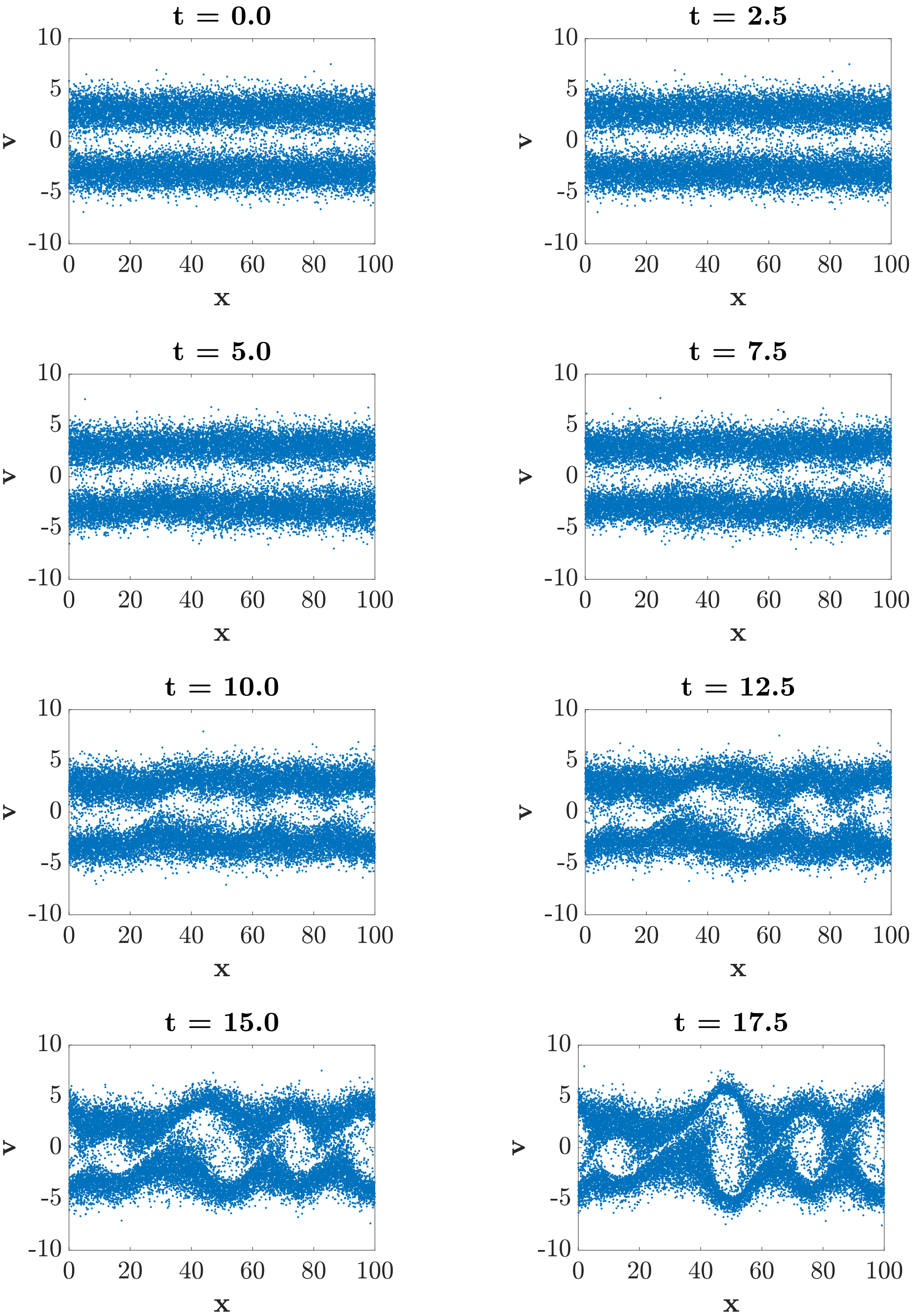

t = 0.0
t = 2.5
t = 5.0
t = 7.5
t = 10.0
t = 12.5
t = 15.0
t = 17.5

Figure 2.5: Simulation results of current study for electron phase space distributions at specified times.

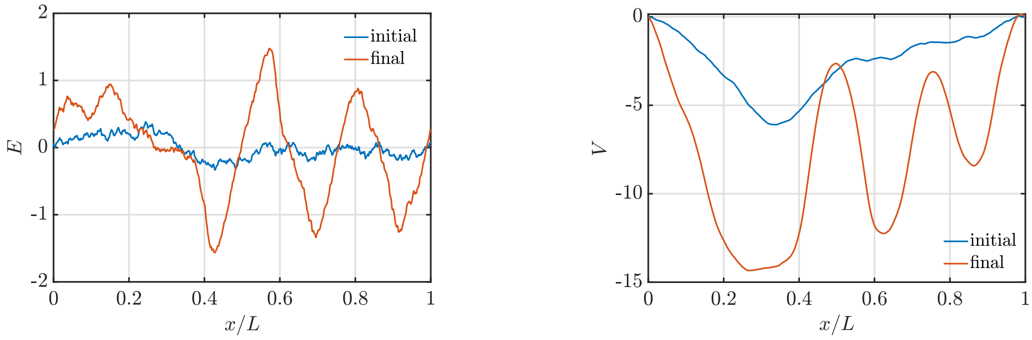

(a) Initial and final electric field profiles.

(b) Initial and final potential profiles.

Figure 2.6: Initial and final electric field and potential profiles obtained from the TSI simulation of the present study. The parameters are dimensionless.

results, which is probably due to the use of different random numbers and solution methods, the general scheme suggests a good agreement. Figure 2.6 illustrates the initial and final potentials and electric fields. In Figure 2.6a, it is seen that initially stable and near-zero electric field evolves into an oscillatory form at the end of the simulation as a result of the instability. Figure 2.7, on the other hand, gives the initial and final electron densities and electron energy distribution functions. Clustering and depletion regions of electrons can be seen in Figure 2.7a as crests and troughs of the oscillating waves of number density. A comparison of Figures 2.6a and 2.7a demonstrates that the positions of these crests and troughs correspond to the positions where the electric field becomes stronger. The electron energy distribution functions (EEDFs) in Figure 2.7b demonstrate an increase in the tails of the curve, which is a result of energy exchange between electrons and the plasma waves. Recall that collisional processes are not included in this simulation, thus the only mechanism of energy transfer is through the interactions of electrons with the electric field in the discharge region.

To further verify the applicability and compatibility of the code, the mean speed of beams is increased so that the condition for the instability that was suggested by Eq. (2.20) is violated. The phase space distributions of electrons for such a case, where the mean speed of beams are set to $v_0 = 20$ with all other conditions kept identical, are given at times $t = 0$, $t = 160$, and $t = 320$ in Figure 2.8. Just as the analytical

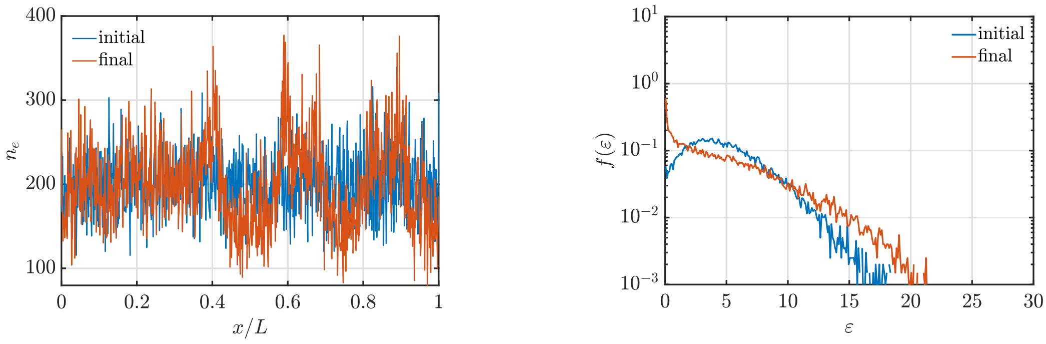

(a) Initial and final electron density profiles.

(b) Initial and final EEDFs.

Figure 2.7: Initial and final electron density profiles and electron energy distribution functions obtained from the TSI simulation of the present study. The parameters are dimensionless.

results suggested, no instability is observed even for about 20 times longer simulation duration.

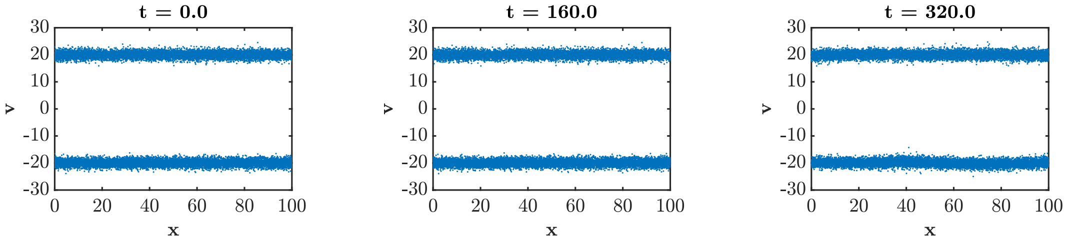

Figure 2.8: Phase space distributions for $v_0 = 20$ at times $t = 0$, $t = 160$, and $t = 320$. TSI formation is not observed at such high speeds, as it was expected by the analytical solution.

One last point about TSI simulation in this study could be the investigation of the effect of thermal spread. In deriving the dispersion relation for the TSI, we assumed that the thermal spread of the beams is negligible. In Fitzpatrick's study [94], the thermal spread value is normalized to 1 and accordingly, in obtaining the initial random speeds of electrons in the beam, the thermal spread value is taken as 1 in the present study. To observe the effect of thermal spread, simulations for lower values of v_{th} are also implemented. In Figure 2.9, the phase space distributions are illustrated for $v_0 = 3$ and $v_{th} = 10^{-6}$ at times $t = 0$, $t = 10$, and $t = 17.5$. In Figure 2.10,

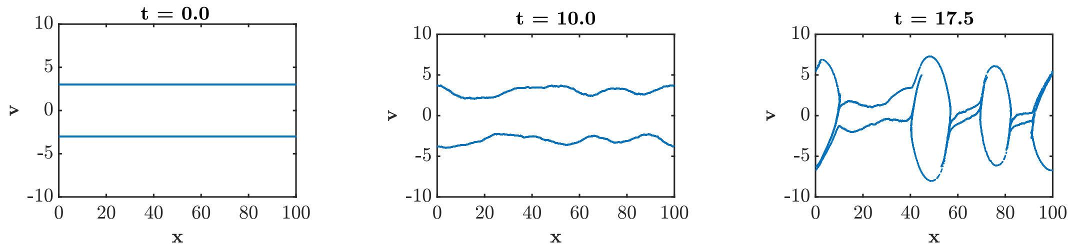

Figure 2.9: Phase space distributions for $v_0 = 3$ and $v_{th} = 10^{-6}$ at times $t = 0$, $t = 10$, and $t = 17.5$.

on the other hand, the electric field and electron density distributions are given. A comparison of Figures 2.10 and 2.7 reveals that the clustering of electrons are more pronounced when the thermal spread of the beams is smaller. Consequently, the energy dissipation from electrons to the plasma wave occur more effectively and thus stronger electric fields are observed at the spatial positions of electron clustering and depletion.

Since the results of TSI PIC simulations are consistent with the reference results of Fitzpatrick's study [94] and the analytical results, it is concluded from this first simulation study that the modules developed so far can be used in further development of the code.

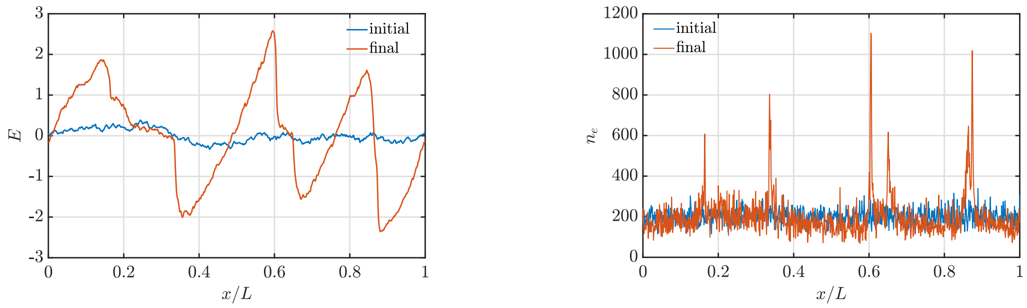

Figure 2.10: Initial and final electric field and electron density profiles obtained from the TSI simulation of the present study for $v_{th} = 10^{-6}$.

2.4 Accuracy, Convergence, and Stability Conditions of PIC Simulations

As a closure, it is worthwhile to mention that the PIC method is subjected to some accuracy, convergence, and stability conditions. First, the size of the grid cells should not be larger than the Debye length. In fact, it was shown by Birdsall and Langdon in [66] that for a grid cell of size Δx, the short-range Coulomb interactions of particles can be disregarded and the clouds of finite-size particles can be assumed to be able to pass through each other with acceptably low noise levels provided that the relation $\lambda_D \gg \Delta x$ holds. Moreover, the longitudinal waves of plasma and the Debye shielding phenomenon can be successfully demonstrated if the cloud size, which is the same as the size of grid cell Δx in PIC scheme, is less than or equal to the Debye length. Hence, the condition $\lambda_D/\Delta x \gtrsim 1$ should be satisfied throughout the entire grid.

Second, the time step size Δt used for the solution of EOM should be sufficiently small so that it resolves the characteristic time scale of the plasma, that is the plasma frequency ω_p. Birdsall and Langdon [66] also showed that when applied to the problem of simple harmonic oscillator, the explicit leap-frog integrator scheme leads to a numerical instability as the product $\omega_p \Delta t$ obtains a value that is greater than 2. As this provides a limiting case on the stability of the scheme, satisfying the condition $\omega_p \Delta t \approx 0.2$ is suggested [66] for obtaining further reduced errors.

Third, the number of superparticles should be sufficiently large so that there exist around 10–100 superparticles per Debye length, as recommended by Hockney and Eastwood [49]. Although ideally it might be expected from a PIC (and also PIC/MCC) simulation that the number of superparticles should not significantly affect the simulation results [87], it is already shown in the literature, e.g. [110], [111], that the number of superparticles can have significant effects on the accuracy and the convergence of the simulations.

It has been reported that a phenomenon called numerical self-heating [112] causes this failure [87]. The numerical self-heating basically emerges as a result of the fluctuations in the number of superparticles within various grid cells, which increase the kinetic energies of the particles throughout simulation iterations [113]. Some filtering or smoothing operations applied to the charge densities at the grid points prior to solving the Poisson equation would reduce the errors caused by self-heating [113]. The effects of self-heating on numerical parameters of plasma simulations are also invesitaged at length in [49] and [66].

Lastly, for PIC methods using the explicit schemes, it is also necessary to check whether the particles travel distances longer than the spatial step size Δx within each time step. This condition is known as the Courant-Friedrichs-Lewy (CFL) condition and requires to satisfy $\Delta t < \Delta x / v_{max}$, where v_{max} is the speed of the fastest particle [114].

CHAPTER 3

DEVELOPMENT AND ANALYSES OF MONTE CARLO SIMULATION

Handling the collisions is one of the key stages of the computational description of plasma processes. Even with advanced recent technology, it is practically not possible in a computer simulation, especially in two or three dimensional analysis, to include as many particles as a real plasma contains. Hence, some suitable models shall be incorporated to simulations. The validity and limitations of developed models, however, should be well understood. In the development of PIC simulation, it was shown that the computational particles (i.e., superparticles, each of which represents many real or physical particles) are treated as having a finite size rather than being point particles. Starting from the very early stages of the development of finite-size particle simulation theory, numerous studies (e.g., [47], [115]–[117]) have shown the validity of using clouds or equivalently superparticles and ignoring (i.e., smoothing) the very short-range collisional interactions of particles in the kinetic simulations of plasma. In a broad sense, various kinds of collisions can be considered in a simulation, such as collisions of charged-charged, charged-neutral, or charged-excited particles. In this chapter, collisions between electrons and neutral atoms will be studied to develop the MCC procedure that to be included in the fully-kinetic PIC/MCC code that is developed in this thesis study. To that end, the mathematical construction of the model will be discussed first. Subsequently, the numerical application of the model will be compared to an electron transport study in steady-state Townsend discharge of argon that was conducted in [95].

3.1 Collision Probability

In a computer simulation that utilizes the kinetic description of a plasma, collisions are handled in a stochastic manner. Hence, it is desired to be known what is the probability that an electron makes a collision with a background gas atom/molecule. For sufficiently short or long time intervals, however, this probability would range from zero to unity. So, this probability should be considered for a specific time interval, which conveniently leads one to the utilization of the concept of a collision frequency in expressing the collision probability:

$$P = \nu \Delta t, \tag{3.1}$$

where

$$\nu = n_g v_r \sigma_T(\varepsilon). \tag{3.2}$$

Here, n_g is the number density of neutral background gas molecules, v_r is the relative speed of incident electron with respect to the background gas molecule, $\sigma_T(\varepsilon)$ is the total collision cross section, and ε is kinetic energy corresponding to the reduced system of the incident electron and the background gas molecule. The total collision cross section is obtained by simply summing the corresponding cross sections of all collisional processes considered in the plasma-chemical model of the problem at hand. Observe that the collision frequency ν shall be time-dependent as the relative speed is a function of time. Even n_g might be a function of both time and position for temporally and spatially inhomogeneous density distributions. Thus, a more rigorous treatment is required to involve the explicit time dependence in the collision probability as well. To this end, following the work of Nanbu [118], consider a time interval from $t = 0$ to $t + \Delta t$, which is denoted as $(0, t + \Delta t)$. Let $Q(t + \Delta t)$ be the probability that an electron makes *no collision* throughout its motion in the time interval $(0, t + \Delta t)$. Then, by the general multiplication rule of probability

$$Q(t + \Delta t) = Q(0, t) Q(t, t + \Delta t). \tag{3.3}$$

It is known from Eq. (3.2) that the probability of an electron to make a collision in a time interval Δt is $P = \nu \Delta t$. Thus, $Q(t, t + \Delta t) \equiv Q(\Delta t) = 1 - \nu(t)\Delta t$. Hence,

$$Q(t + \Delta t) = Q(t)[1 - \nu(t)\Delta t]. \tag{3.4}$$

Beware from Eq. (3.4) that $Q(0, t) \equiv Q(t)$. Let us subtract $Q(t)$ from both sides of Eq. (3.4) and divide both sides by Δt as $\Delta t \to 0$, to have

$$\lim_{\Delta t \to 0} \frac{Q(t + \Delta t) - Q(t)}{\Delta t} = \lim_{\Delta t \to 0} \frac{Q(t)[\cancel{1} - \nu(t)\Delta t - \cancel{1}]}{\Delta t}, \tag{3.5}$$

which reduces to

$$\frac{dQ(t)}{dt} = -Q(t)\nu(t). \tag{3.6}$$

Solving this for $Q(t)$ yields,

$$\int_0^t \frac{dQ(t')}{Q(t')} = -\int_0^t \nu(t')dt', \tag{3.7}$$

$$\ln |Q(t')|_0^t = -\int_0^t \nu(t')dt', \tag{3.8}$$

$$\ln |Q(t)| - \cancelto{0}{\ln Q(0)} = -\int_0^t \nu(t')dt', \tag{3.9}$$

$$Q(t) = \exp\left[-\int_0^t \nu(t')dt'\right]. \tag{3.10}$$

So, what is obtained in Eq. (3.10) is an expression for the probability that an electron makes no collisions in the time interval $(0, t)$. Then, the time dependent form of the probability that an electron makes a collision with a neutral particle simply becomes,

$$\boxed{P(t) \equiv 1 - Q(t) = 1 - \exp\left[-\int_0^t \nu(t')dt'\right]} \tag{3.11}$$

For a more informative form of Eq. (3.10), the averaging of collision frequency may be considered. From calculus, the mean of $\nu(t)$ is written as,

$$\overline{\nu} = \frac{1}{t}\int_0^t \nu(t')dt', \tag{3.12}$$

and hence

$$\int_0^t \nu(t')dt' = \overline{\nu}\Delta t. \tag{3.13}$$

Substituting $\overline{\nu} = n_g\overline{v_r\sigma_T}$, the integral becomes

$$\int_0^t \nu(t')dt' = n_g\overline{v_r\sigma_T(v_r)}\Delta t. \tag{3.14}$$

It is worthwhile to note that since a scalar analysis is conducted here, information about directions is included through the sign of the corresponding vector quantity. Note also that a uniform number density for the background gas is assumed here. Now, Eq. (3.11) can be rewritten as

$$P(\Delta t) = 1 - \exp\left[-n_g\overline{v_r\sigma_T(v_r)}\Delta t\right]. \tag{3.15}$$

Average is taken over all possible background gas molecule velocities (and hence corresponding cross-sections) [119]. Assuming a Maxwellian distribution for the background gas with temperature T_g, the average can be expressed as [95]

$$\begin{aligned}\overline{v_r\sigma_T(v_r)} = \iiint \left(\frac{m_g}{2\pi kT_g}\right)^{3/2} |v_e - v_g|\,\sigma_T(|v_e - v_g|)\\ \times \exp\left(-\frac{m_g v_g^2}{2kT_g}\right) dv_{gx}dv_{gy}dv_{gz},\end{aligned} \tag{3.16}$$

where m_g is the mass of gas molecules, k is the Boltzmann constant, v_e and v_g are velocities of incident electron and colliding gas molecule, respectively. Eq. (3.16) can be simplified assuming that the background gas molecules are at rest. This is a commonly applied assumption, known as *cold gas approximation*, in electron transport studies [95]. Substituting $v_g = 0$ in Eq. (3.16) yields

$$\begin{aligned}\overline{v_r\sigma_T(v_r)} = \left(\frac{m_g}{2\pi kT_g}\right)^{3/2} & |v_e|\sigma_T(|v_e|) \\ & \times \iiint \exp\left(-\frac{m_g(v_{gx}^2+v_{gy}^2+v_{gz}^2)}{2kT_g}\right) dv_{gx}dv_{gy}dv_{gz}. \end{aligned} \tag{3.17}$$

Consider the integral (denoted by I) now:

$$I = \int_{-\infty}^{\infty} e^{-\frac{m_g v_{gx}^2}{2kT_g}} dv_{gx} \int_{-\infty}^{\infty} e^{-\frac{m_g v_{gy}^2}{2kT_g}} dv_{gy} \int_{-\infty}^{\infty} e^{-\frac{m_g v_{gz}^2}{2kT_g}} dv_{gz}. \tag{3.18}$$

Let $\beta \equiv \frac{m_g}{2kT_g}$. Then, using

$$\int_{-\infty}^{\infty} e^{-\beta x^2} dx = \left.\frac{\sqrt{\pi}\,\mathrm{erf}(\sqrt{\beta}x)}{2\sqrt{\beta}}\right|_{-\infty}^{\infty} = \frac{\sqrt{\pi}}{\sqrt{\beta}} \quad (\beta \geq 0), \tag{3.19}$$

the integral I in Eq. (3.18) becomes

$$I = \left(\sqrt{\frac{\pi}{\beta}}\right)^3 = \left(\frac{2kT_g\pi}{m_g}\right)^{3/2}. \tag{3.20}$$

Then, inserting this integral solution into Eq. (3.17) yields

$$\overline{v_r\sigma_T(v_r)} = \sigma_T(|v_e|)|v_e| \cancel{\left(\frac{m_g}{2\pi kT_g}\right)}^{\cancel{3/2}} \cancel{\left(\frac{2\pi kT_g}{m_g}\right)}^{\cancel{3/2}}. \tag{3.21}$$

So, the time dependent probability expression in Eq. (3.15) becomes

$$\boxed{P(\Delta t) = 1 - \exp\left[-n_g\left|v_e\right|\sigma_T\left(\left|v_e\right|\right)\Delta t\right]}. \tag{3.22}$$

It is important to keep in mind that this equation is valid under the cold gas approximation.

3.2 Monte Carlo Collision Method

MCC method is based on comparing random numbers with the collision probabilities. To determine whether the particle under investigation is to experience a collision event, a random number from a uniform distribution on the interval $[0, 1)$ is compared with the collision probability of the particle calculated through Eq. (3.22). If the collision probability is greater than the random number, the particle participates in a collision event. It is important to notice from Eq. (3.22) that the time step size utilized in the simulation directly affects the collision probability along with its effect on the frequency of checking for collision events, that is, how frequently a particle is examined to determine whether it experiences a collision. It is also important to remark that in the classical MCC method, only one collision is allowed per particle per time step, if a collision is to occur. This means, not surprisingly, that an error is introduced as some collisions are probably going to be missed. Hence, the choice of time step size, Δt, has a crucial role in the reliability of the simulation. Vahedi and Surendra [120] advised that Δt shall be determined so that the absolute value of the argument of exponent in Eq. (3.22) is less than (or at worst equal to) 0.1. Donko et al. [87], on the other hand, suggested to keep the collision probability below about 0.05. The stability and accuracy criteria of the PIC/MCC method have been recently revisited and investigated thoroughly in [98].

For a particle that experiences a collision at the current time step, the next task is to determine the type of collision. For this, another random number is picked from again a uniform distribution on the interval $[0, 1)$ and compared with the probability of each individual collisional process. Depending on the interval into which the random number belongs to, the type of collision is determined. The probability of, for example, j-th collisional process can be calculated as

$$P_j = \frac{\sigma_j}{\sigma_T}. \tag{3.23}$$

Considering a total number of N collisional processes, the interval $[0, 1)$ is divided into N segments, of length P_j for the j-th process. Then, saying that a random number R belongs to the first interval means that it satisfies the inequality $0 < R \leq P_1$.

Similarly, if R belongs to the second interval, then $P_1 < R \leq P_1 + P_2$, and so on. Hence, if the random number has a value that satisfies

$$\sum_{k=1}^{l-1} P_k < R \leq \sum_{k=1}^{l} P_k, \tag{3.24}$$

then the l-th collisional process occurs. A visual representation of this procedure is given in Figure 3.1.

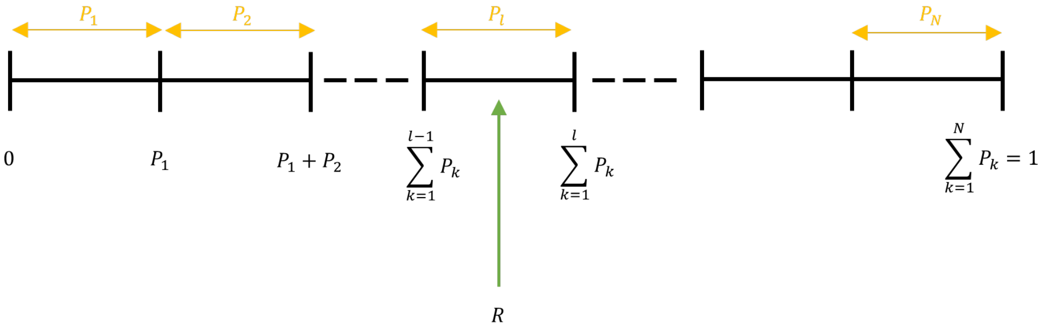

Figure 3.1: Intervals of collisional processes. P_j is the probability for the j-th process, calculated from Eq. (3.23). The processes are arranged in ascending order of threshold energies, from lowest to highest. If the random number R falls into the shown interval, then the l-th collisional process occurs.

After the collisional process is determined, the collision and energy transfers needs to be handled according to the process, and the velocities of the particles after the collision should be calculated. This involves determining the deflection angles (for both elastic and inelastic collisions) and magnitudes of velocities of scattered particles (for inelastic collisions only). Deflection angles consist of the scattering angle χ, which is the angle between the velocity vectors of the incoming particle before and after the scattering, and the azimuth angle η, which is the angle between the post-collisional velocity and the normal to the pre-collisional velocity. It is important to note that the collisions and deflection angles are resolved in the centre of mass (CoM) frame. Hence, the velocities of particles should be written in the CoM frame when handling the collisions. From the definition of CoM, the velocity of CoM for an electron-neutral particle system that consists of constant masses is given by

$$\mathbf{v}_{CoM} = \frac{m_e \mathbf{v}_e + m_n \mathbf{v}_n}{m_e + m_n}, \tag{3.25}$$

where m_e, m_n, $\mathbf{v}_e$, and $\mathbf{v}_n$ are the masses and velocities of electron and neutral particle, respectively. Eq. (3.25) can be written for post-collisional velocities, as well:

$$\mathbf{v}'_{CoM} = \frac{m_e \mathbf{v}'_e + m_n \mathbf{v}'_n}{m_e + m_n}, \tag{3.26}$$

where $\mathbf{v}'_e$ and $\mathbf{v}'_n$ are the velocities of electron and neutral particle after the collision. Eq. (3.26) can be solved for $\mathbf{v}'_e$ to have

$$\mathbf{v}'_e = \frac{m_e + m_n}{m_e}\mathbf{v}'_{CoM} - \frac{m_n}{m_e}\mathbf{v}'_n = \left(1 + \frac{m_n}{m_e}\right)\mathbf{v}'_{CoM} - \frac{m_n}{m_e}\left(\mathbf{v}'_e - \mathbf{v}'_r\right),$$

where $\mathbf{v}'_r \equiv \mathbf{v}'_e - \mathbf{v}'_n$ is the relative velocity of colliding particles after the collision. Further rearrangements yield

$$\left(1 + \frac{m_n}{m_e}\right)\mathbf{v}'_e = \left(1 + \frac{m_n}{m_e}\right)\mathbf{v}'_{CoM} + \frac{m_n}{m_e}\mathbf{v}'_r,$$

and

$$\mathbf{v}'_e = \mathbf{v}'_{CoM} + \frac{m_n}{m_e + m_n}\mathbf{v}'_r. \tag{3.27}$$

Note that since the total momentum is conserved and we consider a closed system, the velocity of the CoM does not change after the collision, i.e., $\mathbf{v}'_{CoM} = \mathbf{v}_{CoM}$ and hence

$$\mathbf{v}'_e = \mathbf{v}_{CoM} + \frac{m_n}{m_e + m_n}\mathbf{v}'_r. \tag{3.28}$$

Similarly, solving Eq. (3.26) for $\mathbf{v}'_n$ with $\mathbf{v}'_{CoM} = \mathbf{v}_{CoM}$ yields,

$$\mathbf{v}'_n = \frac{m_e + m_n}{m_n}\mathbf{v}_{CoM} - \frac{m_e}{m_n}\mathbf{v}'_e = \left(1 + \frac{m_e}{m_n}\right)\mathbf{v}_{CoM} - \frac{m_e}{m_n}\left(\mathbf{v}'_n + \mathbf{v}'_r\right),$$

$$\left(1+\frac{m_e}{m_n}\right)\mathbf{v}_n' = \left(1+\frac{m_e}{m_n}\right)\mathbf{v}_{CoM} - \frac{m_e}{m_n}\mathbf{v}_r',$$

and

$$\mathbf{v}_n' = \mathbf{v}_{CoM} - \frac{m_e}{m_e+m_n}\mathbf{v}_r'. \tag{3.29}$$

Note that in the case of the cold-gas approximation, $\mathbf{v}_n = 0$, and hence the relative velocity simply equates to the electron velocity, $\mathbf{v}_r = \mathbf{v}_e$.

The determination of the deflection angles and the relative velocity after the collision differ for elastic and inelastic collisions. Moreover, various approaches might be used to calculate the scattering angle χ depending on whether an isotropic or anisotropic scattering case is considered. In cases where a model or some experimental data exist for the differential cross section as a function of both energy and the scattering angle, one can consider the anisotropic scattering case [1] and obtain the scattering angle χ through the relation given in Eq. (3.30) [95].

$$\frac{\int_0^{\chi}\sigma\left(\varepsilon,\chi'\right)\sin\chi' d\chi'}{\int_0^{\pi}\sigma\left(\varepsilon,\chi'\right)\sin\chi' d\chi'} = R. \tag{3.30}$$

For instance, in [121], an analytical expression is given for an anisotropic scattering case in an attempt to correct an erroneous approach that had been given in a previous study in [62].

Here, however, the isotropic scattering case is considered. For elastic collisions, the scattering angle χ and the azimuth angle η are calculated through Eqs. (3.31) and (3.32) [95], respectively:

$$\chi = \cos^{-1}\left(1-2R\right), \tag{3.31}$$

$$\eta = 2\pi R, \tag{3.32}$$

---

[1] Note that in the case of an anisotropic scattering, a transformation of the velocity vector of the incoming particle is necessary prior to and after the collision event. A detailed explanation is given in [87].

where R is a random number from a uniform distribution on the interval $[0,1)$. The magnitude of the relative velocity does not change in the case of an elastic collision, hence ${v_r}' = v_r$.

For inelastic collisions, on the other hand, the magnitude of the relative velocity is not constant, and the change is calculated through the change in energy. In an inelastic collision case for which the threshold energy of the chemical process is $\varepsilon_{th.}$, the energy of the system of colliding particles after the collision event is given by

$$\varepsilon' = \varepsilon - \varepsilon_{th.}. \tag{3.33}$$

It is important to recall that the collisions events are handled in the CoM frame. Hence, the energies in Eq. (3.33) are calculated for the reduced system of the colliding particles:

$$\varepsilon = 0.5\mu(v_r)^2, \tag{3.34}$$

$$\varepsilon' = 0.5\mu({v_r}')^2, \tag{3.35}$$

where μ is the reduced mass of the system of colliding electron and neutral particle. In an excitation collision, the deflection angles are determined from Eqs. (3.31) and (3.32), whereas in an ionization collision, they are obtained through [87]

$$\chi_{sc.} = \cos^{-1}\left(\sqrt{\frac{\varepsilon_{sc.}}{\varepsilon'}}\right), \quad \eta_{sc.} = 2\pi R, \tag{3.36}$$

and

$$\chi_{ej.} = \cos^{-1}\left(\sqrt{\frac{\varepsilon_{ej.}}{\varepsilon'}}\right), \quad \eta_{ej.} = \eta_{sc.} + \pi, \tag{3.37}$$

where the subscripts *sc.* and *ej.* indicate scattered and ejected electrons after the collision event, respectively. This requires a choice of sharing the remaining energy ε'

between the scattered and ejected electrons. This is done according to the expression in Eq. (3.38) that is given in [87] as produced from the experimental data in [122]:

$$\varepsilon_{ej.} = c \tan\left[R \tan^{-1}\left(\frac{\varepsilon'}{2c}\right)\right], \tag{3.38}$$

where c is a parameter whose value depends on the background gas. Then, the energy of scattered electron simply becomes $\varepsilon_{sc.} = \varepsilon' - \varepsilon_{ej.}$. Note that the energies are in eV, except for Eqs. (3.34) and (3.35) for which the unit conversion between eV and J shall be carried out.

For cases involving large numbers of superparticles, the classical MCC method can be rather time-consuming as it involves the computationally expensive operations of calculating the kinetic energies, collision probabilities, post-collision velocities, and angles of each particle participating in the collision event. In an attempt to resolve this, the *null-collision method* is used. This method is based on the idea of obtaining a constant total collision frequency by the addition of a new collisional process (null collision) and was first introduced by Skullerud [56] for the problem of determining the free times between collisions for ion motion in a gas that is subjected to a constant electric field. Since then, the method has been adopted and further improved in various PIC/MCC and swarm studies (e.g., [57], [95], [118], [120], [123], [124]) and has become a standard method for improving the performance of the codes implemented for those studies. In this thesis study, the procedure given in [120] is followed to implement the null-collision method. The constant total collision frequency is obtained through

$$\nu_c = \max\left(n_g \sigma_T v\right) = n_g \max\left(\sigma_T v\right), \tag{3.39}$$

since in all cases of the study the background gas density is assumed to be spatially and temporally uniform. The main strength of the method comes from the fact that the check for whether a particle collides in each time interval is performed for only a subset of all particles rather than all of them. This portion is determined from

$$P_{null} = 1 - \exp\left(-\nu_c \Delta t\right). \tag{3.40}$$

This portion of particles is randomly chosen among all particles without duplicates; i.e., there are no particles that are checked more than once whether they participate in collisions, and hence any particle can only experience a collision once at most within one time step. Once those particles are chosen, a random number is compared with fractional collision frequencies of each collision type and the constant collision frequency. Let

$$q_i \equiv \frac{\sum_{k=1}^{i} \nu_k}{\nu_c}, \tag{3.41}$$

where the subscript i designates the type of collision. If the relation $q_{i-1} < R \leqslant q_i$ holds for the random number R, then the i-th collision event occurs, where the ordering of collision events is done according to the threshold energies of collision types in an ascending manner. For a total of M collision types, if

$$\frac{\sum_{k=1}^{M} \nu_k}{\nu_c} < R, \tag{3.42}$$

then the null collision occurs. In that case, no real collision takes place and the iteration continues with the next particle. Even though the null-collision method introduces the random and not duplicated selection of colliding particles as an extra routine, depending on the value of P_{null}, the reduction of the floating point operations compared to the classical MCC method is generally rather high.

3.3 Electron Transport in Steady State Townsend Discharge

In order to verify the MCC part of the code, the electron swarm study of steady state Townsend discharge by Donko [95] is considered as a case study. This involves the consideration of electrons as particles within a homogeneous electric field configuration with uniform background argon gas. In [95], primary electrons are released from the cathode one by one. On its journey from cathode to anode, collisions of a primary electron with neutral argon gas atoms are handled. In the case of impact ionization, the position, time and velocity information of new electrons are recorded and the primary electron is continued to be followed until it reaches and is absorbed by the anode. Then, secondary electrons that were kept in the *stack* are followed one by one in the order that they were recorded until they end up on and absorbed by the anode, as well. When all the secondary electrons reach and are absorbed by the anode, the next primary electron is released from the cathode and the entire procedure is repeated each time for every primary electron. In this thesis study, on the other hand, all primary electrons are emitted from the cathode at once initially and all particles, including the secondary electrons emerging from impact ionization events, are followed from cathode through the anode simultaneously. It is important to notice that since in this study the electric field within the discharge region is homogeneous and hence the Poisson equation is not coupled to the system, there is not any interaction between the electrons. Hence, it makes no difference whether the particles are released all together, or one by one and that makes this study a good candidate for a first case study for verification of the MCC implementation of the code. For that purpose, the conditions given in Table 3.1 are considered.

Table 3.1: Parameters for SSTD simulation.

Parameter	**Symbol**	**Value**
Reduced electric field (Td)	E/N	500
Pressure (Torr)	p	1
Background gas temperature (K)	T	300
Time step size (s)	Δt	10^{-12}
Number of grid points	N_G	201
Number of primary superelectrons	$N_{el.}$	$200,000$

To establish a steady state, 1000 superelectrons are also released from the cathode per each 400 iterations, in addition to the primary ones emitted initially. Note that these are arbitrary values that were selected after a couple of tests, and there are not any exclusive reasons for selecting them. Different values do not yield any distinguishable swarm parameter outputs. Rather, the steady state is established at different particle number values. All primary particles are emitted from the cathode with 1 eV energy isotropically over a hemisphere facing to the anode (cathode is situated at the left side of the discharge region). The spherical coordinates of the LAB frame utilized in the study is given in Figure 3.2. So, the velocity initialization of the particles is done as follows:

$$
\begin{aligned}
v_x &= v\cos(R_\theta), \\
v_y &= v\sin(R_\theta)\cos(R_\phi), \\
v_z &= v\sin(R_\theta)\sin(R_\phi),
\end{aligned}
\tag{3.43}
$$

where, $v = \sqrt{2e/m_e}$ is the speed value of electrons corresponding to 1 eV of kinetic energy, and R_θ and R_ϕ are the random numbers for θ angle in $[-\pi/2, \pi/2]$ interval and ϕ angle in $[0, 2\pi]$ interval, respectively.

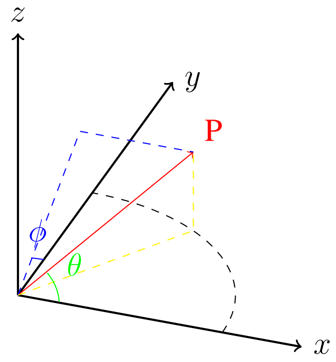

Figure 3.2: Spherical coordinates used in SSTD study

The plasma-chemical model (given in Table 3.2) includes excitation and impact ionization as inelastic collision processes, and an effective momentum transfer as elastic collision processes between electrons and background neutral Ar atoms. Cross sections of these processes are retrieved from the LXCat website (Phelps database) [125].

The simulation was first run serially on a PC with Intel® Core™ i7-1065G7 CPU processor with classical MCC method utilized for collisions. The implementation of this code was not completed because it took quite a long time. After the 24-hour run, the simulation was not even half finished. Since the run times of successive iterations are exponentially increasing, it was predicted that it would take several days to complete the whole simulation. Then, the null collision method was associated and the code was parallelized with Intel® MPI library. The implementation of the latter took about 4 hours with 4 cores on the same PC. About 390 million collision events occurred and 6.3 million electrons were absorbed by the anode. Collision probabilities are kept below about 0.02 for both procedures. In the null-collision method, $P_{null} \simeq 0.01$; this means that only about 1% of all electrons are checked for collisions at each time step. The steady state was reached at about $t = 30$ to $t = 50$ ns depending on the density and frequency of additional primary electron emission from the cathode and the data collection for measurement of various transport parameters was carried out from 80 to 100 ns. It is observed from the execution times of serial and parallel versions of the code that even for such a simple case involving only electrons as particles, considering only one excitation and impact ionization events of inelastic processes, and achieving the steady state in such a short physical time duration, classical MCC method may become computationally rather expensive and the code has to be parallelized for more complex simulations.

Table 3.2: Plasma-chemical model of the SSTD simulation.

Process	**Reaction**	**Threshold Energy (eV)**
Elastic Scattering	$e^- + Ar \rightarrow Ar + e^-$	–
Excitation	$e^- + Ar \rightarrow Ar^* + e^-$	11.5
Ionization	$e^- + Ar \rightarrow Ar^+ + e^- + e^-$	15.8

At the end of the simulation, transport parameters of the mean energy $\langle \varepsilon \rangle$, the drift velocity v_d, and the Townsend ionization coefficient α are taken as output. In Figure 3.3, results of those parameters obtained from the parallel computation is illustrated against the results of the study in [95]. α is obtained from the relation $\alpha(x) = \Gamma^{-1}(x)\ \mathrm{d}\Gamma(x)/\mathrm{d}x$, where Γ is the electron flux, as given in [95]. The derivative is taken by using the second order central differences scheme. The small differences in the results might be emerged from the use of different seed values for random numbers, from the differences in data collection methods, or from different approaches that might be utilized throughout the simulations. It is also important to note that there might be some errors resulting from the retrieval of results of [95]. The reference data in Figure 3.3 were extracted from figures illustrated in [95] using GRABIT [126] code implemented in the MATLAB® environment because no source of data for the given results was found. Again, the maximum relative errors could not

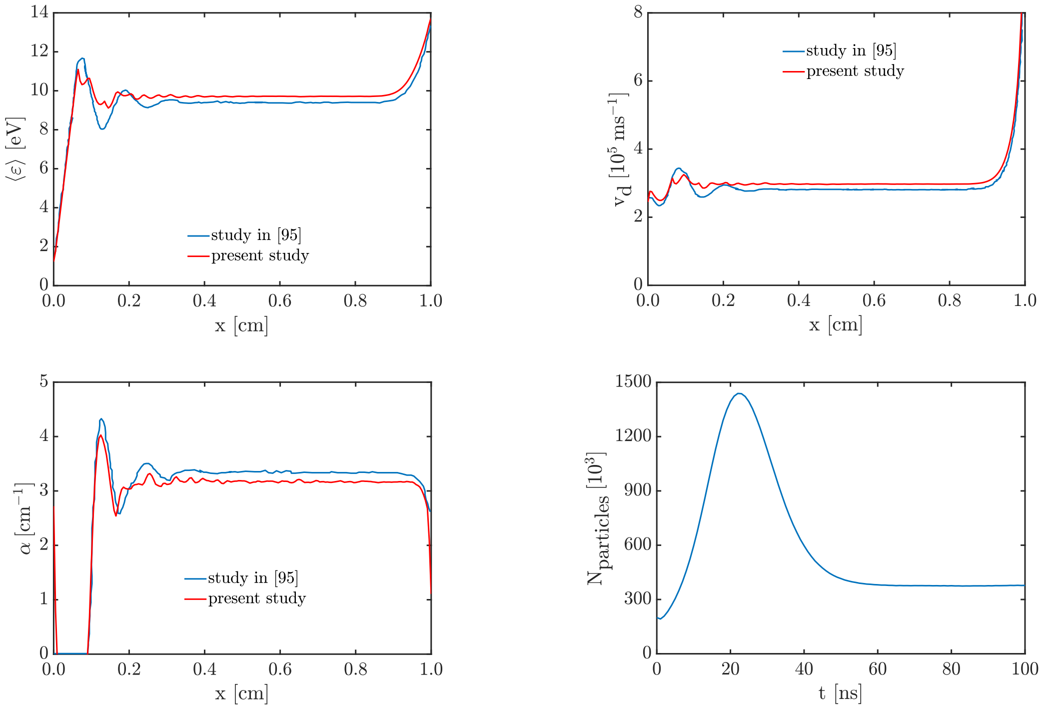

Figure 3.3: Computed transport parameters in comparison to those from [95]

be calculated due to the lack of reference data, yet an analysis over the use of error bars gives quantitative results. Utilization of error bars on the graphs revealed that the maximum relative errors were obtained around the region where $x/L = 0.2$ as about 15%. For the analysis of the Townsend ionization coefficient, discharge region that is near the cathode is not considered since the periodic and discrete electron emission disturbs the electron flux in that area, which results as an abrupt jump in the value of α that is not actually coming from the ionization events. Comparisons including the error bars are given in Figure 3.4. In Figure 3.5, on the other hand, velocity distribution functions (VDF) of electrons obtained from the present study at various regions are illustrated as color maps. A comparison to the same results taken from the original study [95] in Figure 3.6 reveals a good agreement between the distributions by making allowances for minor differences in the color bar assignments.

The physical picture obtained from Figures 3.3 and 3.5 indicates some interesting features about the swarm parameters. The most conspicuous result is that the transport parameters are not constant through the discharge region, even though the electric field was considered to be uniform in the entire region. In fact, as also pointed out

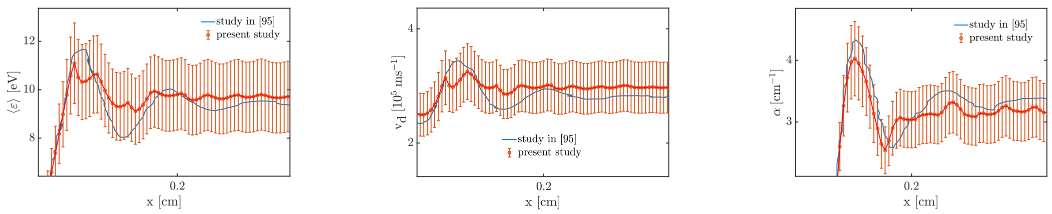

Figure 3.4: Error bars are utilized to obtain the maximum relative errors in transport parameter results in comparison to results from [95]. Error bars correspond to 15% of the data obtained in the thesis study.

in [95], there seem to be three distinct regions of the discharge where the transport parameters show different behaviours: (i) non-equilibrium region with $x/L \lesssim 0.4$, (ii) equilibrium region with $0.4 \leq x/L \leq 0.9$, and (iii) near-anode region with $x/L \gtrsim 0.9$. The transport parameters in the region (i) are noticeably far from equilibrium. The VDF in this region starts with the shape of a single ring at the position $x/L = 0.050$ and evolves first into concentric rings and then into a continuous circle of several layers with various widths and colors. The nearly monochromatic single ring shows that the electron energies are almost isotropic as a result of numerous elastic collisions at $x/L = 0.050$. As electrons move further from the cathode, they gain sufficient energies for excitation and impact ionization events, and hence the isotropy in the energies of electrons breaks down. This manifests itself in Figures 3.5 and 3.6 as a transformation from ring structure to circle structure for $x/L = 0.100$ to $x/L = 0.250$. The VDFs in equilibrium region (ii) illustrate a circular structure with a more pronounced distribution around the centre. It is also observed that the centre point starts to slide horizontally to the direction of anode as a result of the drift. In region (iii), the effect of the absorbing anode is reflected on the transport parameters and VDF. As a result of the absorption on the anode, the number of electrons moving in the cathode direction decreases. Since all electrons reaching the anode are absorbed and neither reflections nor ion-induced secondary electron emissions from the boundaries are included in the study, this behaviour is markedly observed as an asymmetry in the VDF at $x/L = 0.990$. A comparison of VDFs at $x/L = 0.800$ and $x/L = 990$ reveals the apparent reduction of electrons moving in the negative x direction. This reduction results in an increase in the drift velocity v_d at that region. The depletion of slow electrons in the negative x direction causes an increase in the mean energy $\langle \varepsilon \rangle$, whereas the Townsend ionization coefficient α decreases since also the number of high energy electrons diminish.

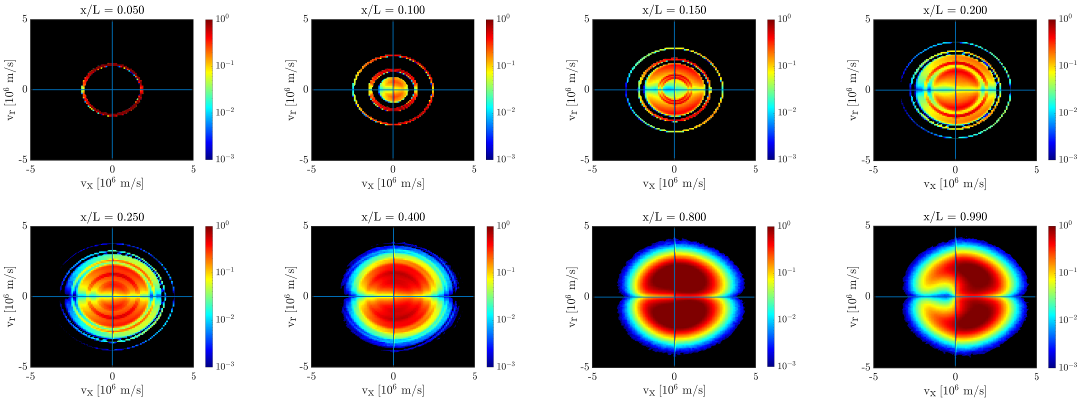

Figure 3.5: Electron VDFs at various positions of discharge region obtained from SSTD simulations of this thesis study. The scales of color bars are logaritmic.

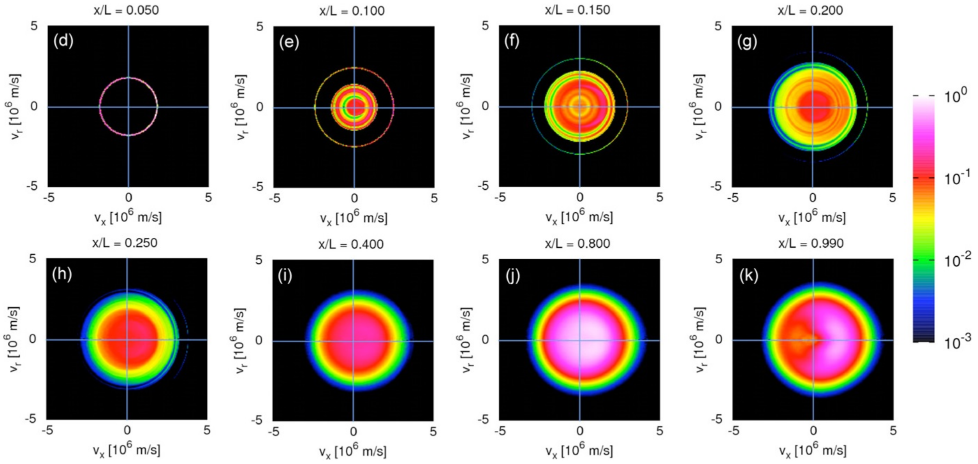

Figure 3.6: Electron VDFs at various regions of the discharge obtained from the simulations in [95].

Results presented in this chapter suggest that the developed MCC model can be adapted to the self-consistent fully kinetic code for further simulations.

CHAPTER 4

PIC/MCC SIMULATIONS OF RADIOFREQUENCY CAPACITIVELY COUPLED PLASMA

4.1 Modelling of RF CCP and the Need for A Kinetic Model

RF CCP is a common type of low-pressure plasma discharge in which the plasma is sustained by coupling the electrical power to the plasma directly through electrodes of an appropriate material. As a result of this coupling mechanism, a sheath region of high voltage is formed between electrodes and the main body of plasma. Then, the alternating currents crossing between these regions produce the main heating mechanisms that sustain the plasma, i.e., stochastic heating in the sheath region, and ohmic heating in the bulk of plasma [127]. Even though the frequencies of voltages applied to the electrodes may range from several kHz to several thousand MHz, the most common frequency used, especially in industrial plasma, is 13.56 MHz, in accordance with the international frequency allocation regulations [22]. RF CCP is used in various fields, such as thin film deposition, etching, microelectronics, and space propulsion systems [13], [128], [129]. Hence, such an important plasma requires reliable methods of modelling. Over the years, numerous models and simulations have been built, e.g., [67], [68], [95], [103], [120], [130]–[135]. Some of those models and simulations implement particle methods, whereas others perform fluid or hybrid methods with different boundary conditions. Even though fluid models may adequately represent the characteristics of RF CCPs qualitatively in some cases, comparisons to the PIC/MCC model yield quantitative errors of up to 60% for parameters such as the plasma density and the average ion fluxes, as well as the overestimation of plasma sheath width [131]. Hence, a rigorous quantitative analysis of RF CCP requires the implementation of particle methods. PIC/MCC methods arise as a reliable option for that purpose, such that from the prevalence of studies over the last decades, one can reasonably claim that they have become the standard methods of especially low-pressure RF CCP simulations. Owing to the recent advancements of computational technologies, advanced simulations may even be conducted through personal computers.

4.2 Ion-Neutral Collisions

In order to implement a low-pressure RF CCP simulation, the codes developed in Chapters 2 and 3 are to be combined with the Poisson solver coupled into the system with one electrode grounded and the other subjected to a sinusoidal voltage of the form $V(t) = V_A \cos(\omega t)$, where V_A is the voltage amplitude. Moreover, the method needs to be improved by including ion-neutral collisions, and the code should be adapted as per that. Unlike electron-neutral collisions, the cold gas approximation is not applicable to ion-neutral collision events since the velocities of ions and neutrals become comparable to each other. Hence, during an ion-neutral collision event, the velocities of both species should be taken into account and the collision probability given in Chapter 3 in Eq. (3.22) should be updated by including the relative velocity of the colliding particles:

$$P(\Delta t) = 1 - \exp\left[-n_g \left|v_r\right| \sigma_T \left(\left|v_r\right|\right) \Delta t\right]. \tag{4.1}$$

The collisions events are handled in the centre of mass frame in the ion-neutral collisions, as well. In Chapter 3, the derivations for the post-collisional velocities were already conducted for the general case. Inserting the ion mass and velocity into Eqs. (3.28) and (3.29) yields the post-collision velocities for ion-neutral collisions:

$$\mathbf{v}_i' = \mathbf{v}_{CoM} + \frac{m_n}{m_i + m_n}\mathbf{v}_r', \tag{4.2}$$

$$\mathbf{v}_n' = \mathbf{v}_{CoM} - \frac{m_i}{m_i + m_n}\mathbf{v}_r'. \tag{4.3}$$

Here, only elastic collisions are considered for ion-neutral pairs and the scattering of colliding pairs consists of isotropic and backward scattering, as suggested by Phelps in [136]. For the cross-sections, the approximated analytical formulas given in [136] are used to establish a lookup table (LUT) for CoM energies from 0 up to 10^3 eV with an increment of 10^{-3} eV through linear interpolation, as done in eduPIC code [87]. When this table is assigned to an array at the beginning of the code, it reduces the run time significantly by eliminating the need for calculating the cross-section in every time step for each collision event. Rather, the index of the energy is calculated based on the relative speed of the colliding particles and then the corresponding value is taken from the LUT. Hence, this is adapted to the code developed in this thesis study. For electrons-neutral collisions, the LUTs are generated for energies obtained from the LAB frame velocities. For ion-neutral collisions, on the other hand, the LUTs are generated for energies in the CoM frame velocities.

For the isotropic scattering collision, the scattering angle χ is calculated in the same way as for electrons through Eq. (3.31), whereas for the backward scattering collision, χ is simply taken as π. The azimuth angle in both cases is determined through Eq. (3.32).

4.3 A Case Study: Comparison to eduPIC Single-Frequency RF CCP Simulation Results

In this section, the developed code is implemented for the single-frequency RF CCP simulation carried out through eduPIC code in [87]. Simulation parameters (given in Table 4.1) are taken to be identical to those used in the eduPIC code to obtain comparable results.

The plasma-chemical processes include elastic, excitation, and ionization collisions for electron-neutral collisions (same as in Table 3.2) and isotropic scattering, and backward scattering for ion-neutral collisions. The cross-sections for electron-neutral collisions are taken from [125] and LUTs are established for electron-neutral and ion-neutral collisions by following the procedure reported in Sec. 4.2. Null-collision method is utilized for both electron-neutral and ion-neutral collisions, where $P_{\text{null}} =$

Table 4.1: Basic parameters of single-frequency RF CCP simulation.

Parameter	**Symbol**	**Value**
Voltage amplitude	V_A	250 V
Frequency	f	13.56 MHz
Superparticle weighting	W	7×10^4
Discharge gap	L	25 mm
Background gas (Ar) pressure	p	10 Pa
Background gas (Ar) temperature	T_g	350 K
Number of grid points	N	400
Number of time steps within 1 RF cycle	N_T	4000

1.26×10^{-2} for the former and $P_{\text{null}} = 2.00 \times 10^{-2}$ for the latter.

For the random numbers, the Mersenne Twister 19937 generator of Intel® oneAPI Math Kernel Library is utilized with random seeds. To decrease the process time, random numbers are created initially and assigned to an array of size 100 million at the cost of increasing the complexity of the code as it requires the tracing of indices and rebuilding new arrays with different seeds when all the elements of arrays are used. Particles reaching the boundaries are completely absorbed and the arrays keeping the information of particles are reallocated in the code.

The stability and accuracy conditions given in [87] are also followed by checking if (i) $\Delta x/\lambda_D \lesssim 1$, (ii) $\omega_{pe}\Delta t_e < 0.2$, and (iii) $P_{\text{coll.}} \cong 0.05$. The inspection of these conditions after the steady-state is achieved yielded values of 0.723 for the condition (i), 0.090 for the condition (ii), and about 0.005 in electron-neutral collisions and 0.02 in ion-neutral collisions for the condition (iii), respectively. In [87], it is suggested to check the CFL condition based on the comparison of the electron energies against a maximum energy for which the CFL condition is satisfied. For this case study, it is advised to observe whether the value of EEPF in the centre of the plasma satisfies $f(\varepsilon_{max}) \lesssim 10^{-6}$ eV$^{-3/2}$. Judging by the match of EEPF values in Figure 4.3a, evidently the CFL condition is also met in this study.

The simulation is run for the conditions given in Table 4.1 for 2500 RF cycles. For

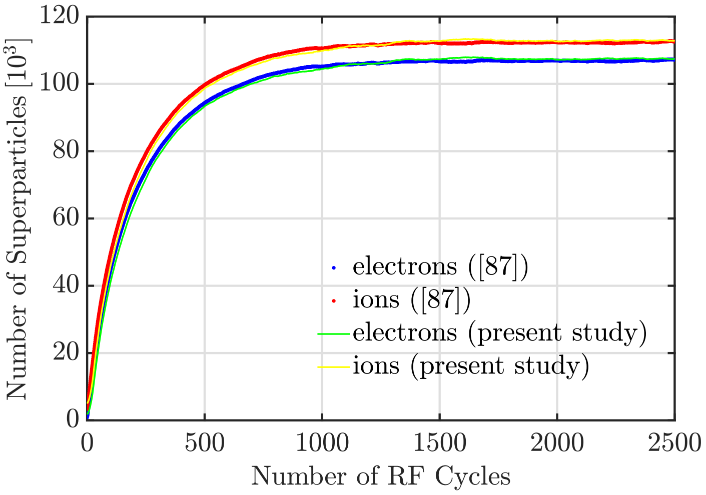

Figure 4.1: The evolution of superparticles against RF cycles as compared to the results from [87].

$N_T = 4000$, this corresponds to $dt_e = T/N_T = 1.8437 \times 10^{-11}$sec. of time step size and about 0.184 ms of simulation in real time. The initial number of superparticles is taken as 2500 for both electrons and ions. The steady-state [1] is achieved at RF cycle of around 1500, as it was the case in [87] as well. To collect some data and check for stability and accuracy conditions, the simulation is continued to run for another 1000 RF cycles. The comparison of superparticle evolution against the RF cycle number is given in Figure 4.1.

In Figure 4.2, the time-averaged electron and ion number densities with respect to the position in discharge region are plotted and compared against the result from [87]. The maximum relative error of number densities obtained in the present study with respect to the results from [87] are calculated as 1.41% for electrons and 1.56% for ions. In Figure 4.2, the overlap of electron and ion density curves in the middle of discharge region indicates the behavior of quasi-neutrality, whereas the depletion of electrons near the both electrodes points out the development of plasma sheaths.

In Figure 4.3, time-averaged distribution functions of electrons and ions are depicted and compared to the relevant results from [87]. Figure 4.3a illustrates the electron energy probability function (EEPF) distribution at the centre of discharge such that

---

[1] Note that the condition for achieving the steady-state is considered to be that the number of superparticles does not significantly change, but rather fluctuates around some value.

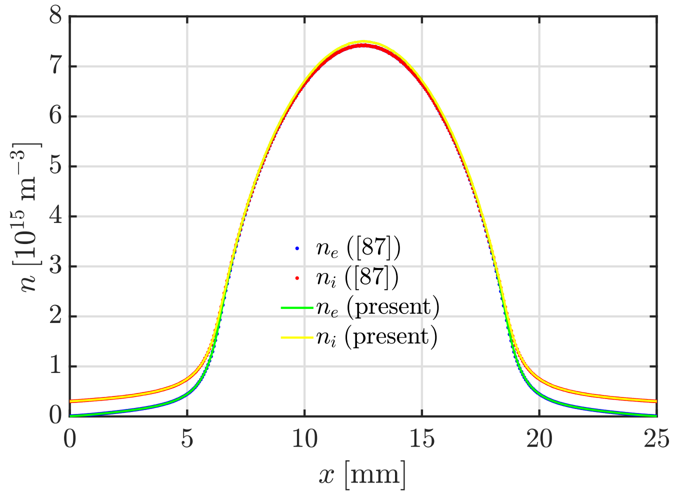

Figure 4.2: Time-averaged electron and ion number densities with respect to the position in discharge region as compared to the results from [87].

the ratio x/L satisfies $0.45 < x/L < 0.55$. Note that EEPF is normalized according to $\int f(\varepsilon)\sqrt{\varepsilon}d\varepsilon = 1$. Figure 4.3b, on the other hand, shows the ion flux-energy distribution function (IFEDF) at the powered electrode, i.e., where $x = 0$. Note also that IFEDF is normalized according to $\int F(\varepsilon)d\varepsilon = 1$. In Figure 4.3a, a well-known classical behavior of EEPF of low-pressure RF CCP argon discharge is observed. The evolution of EEPF for various pressures in a RF CCP argon discharge with frequency of 13.56 MHz is experimentally given in [137]. In Figure 4.3b, some characteristic series of peaks are observed in the IFEDF distribution, which are attributed to the predominance of the secondary ions resulting from the charge-exchange procedure of ion-neutral collisions [138], [139].

In Figure 4.4, various characteristics of the discharge are shown in the form of colormaps that are obtained via MATLAB®. Following the results given in [87], both spatial and temporal (i.e., spatio-temporal) distributions of electron number density (n_e), ion number density (n_i), potential (Φ), electric field (E), electron current density (j_e), ion current density (j_i), electron power density (P_e), ion power density (P_i), the mean energy of electrons ($\langle\varepsilon_e\rangle$), the mean energy of ions ($\langle\varepsilon_i\rangle$), and the rate of ionization or ionization source function ($R_{ion.}$) are regenerated consistently in the same format and demonstrated in parts from (a) to (k) of Figure 4.4, respectively. Horizontal uniformity of various color layers, corresponding to various positions, in

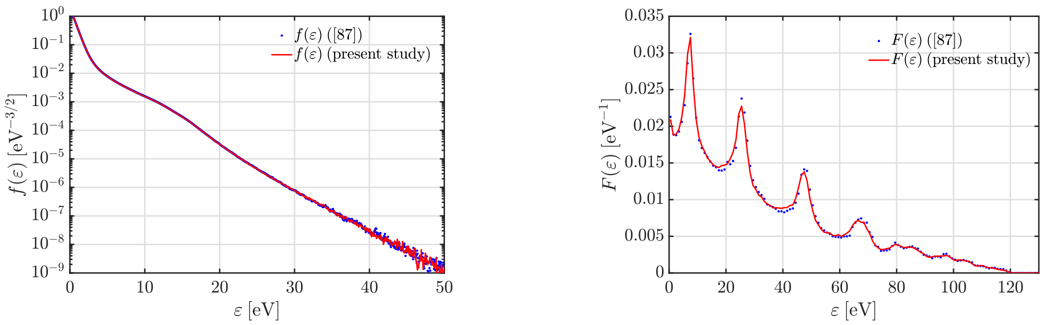

(a) The time-averaged electron energy probability function (EEPF) at the centre of discharge region as compared to the result from [87].

(b) The time-averaged Ar$^+$ ion flux - energy distribution function (IFEDF) at the powered (left) electrode as compared to the result from [87].

Figure 4.3: Time-averaged distribution functions of electrons and ions. EEPF is binned with 2000 data points corresponding to a resolution of 0.05 eV, whereas IFEDF is binned with 200 data points corresponding to a resolution of 1 eV as in [87]. Discharge conditions are given in Table 4.1.

(b) reveals the time-independent behavior of ion density, whereas the white spaces in (a) correspond to the electron depletion regions and thereby indicate the sheath region. Observe that these regions overlap with the extrema of electric field values shown with dark shades of blue and red colors in (d). The relatively uniform and darkest red distributions in (a) and (b), and white spaces in (d) together mark the quasi-neutrality in the bulk of plasma region. In consistency with this, it can be seen in (e) that the electron current density is zero in the electron depletion regions (shown with white color) and maximum in the bulk of plasma region, being in the direction of powered electrode for the first half of the period and of grounded electrode for the second half of the period. The ion current density in (f), on the other hand, starts from around zero in the centre of discharge region and reaches its maximum value toward both electrodes, almost time-independently. These two images are consistent with the very high and low mobilities of electrons and ions, respectively. In (g) and (h), the behavior of power absorption of electrons and Ar$^+$ ions is demonstrated. Negative values for electrons, shown with blue color, represent the power loss.

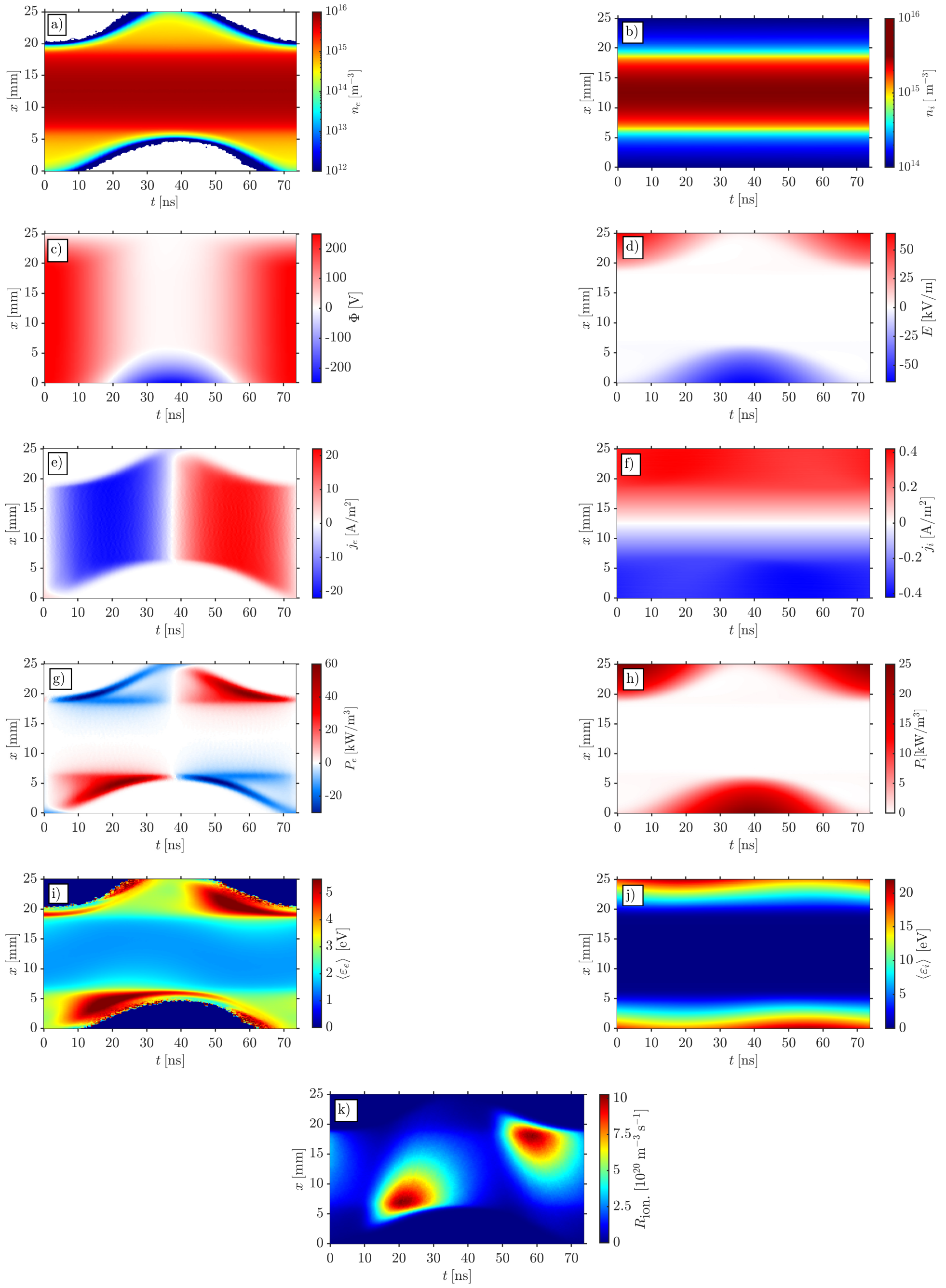

Figure 4.4: The spatio-temporal distributions of the (a) electron number density (n_e), (b) ion number density (n_i), (c) potential (Φ), (d) electric field (E), (e) electron current density (j_e), (f) ion current density (j_i), (g) electron power density (P_e), (h) ion power density (P_i), (i) electron mean energy ($\langle\varepsilon_e\rangle$), (j) ion mean energy ($\langle\varepsilon_i\rangle$), and (k) rate of ionization ($R_{ion.}$) obtained in the present study. On the horizontal axis is the time through one RF period and on the vertical axis is the distance from the powered electrode. The discharge conditions are given in Table 4.1.

In each electrode, it is observed that the electron power absorption increases as the sheath expands and decreases to negative values as the sheath collapses. It is also observed that the power absorption of ions increase at those times when the ions are moving toward to electrodes within the sheath regions. In (i) it is seen that the maximum electron mean energies occur around at the edges of expanding sheath regions of specific times, consistently with the maximum power absorption of electrons. Clearly, an increase in the absorbed power gives rise to the mean energies. Some high mean energy regions are also observed within the collapsing sheath regions, which are attributed to the electric field reversals within the sheath regions [87], [140]. Outside the sheath regions, the mean energy of electrons attains a fairly constant value, around 1.5 eV, over the entire period. In (j), on the other hand, the mean energy of Ar^+ ions is observed as layers of colors with different widths from centre to the boundaries of discharge region. In the bulk of the plasma, the ions have mean energies near zero, whereas in sheath regions they attain increasing energies towards the boundaries and attaining maximum values around 20 eV in the collapsing sheath regions. Finally, in (k), it is observed that the regions where the maximum ionization occurs overlap with those regions where the maximum power absorption and consequently high mean energies occur. Intriguingly, a comparison of (g) or (i) with (k) reveals that the region of maximum ionization rate is extended over a larger distance. This shows that the simulation successfully displays the effect of energetic electrons coming out of the sheath regions, of which the fluid models fail to show.

4.4 Benchmarking the Code

Benchmarking any computational simulation is undoubtedly an indispensable stage in the process before claiming the accuracy and validity of the simulation and using it for further investigations. One recent and widely referred benchmark study for low-pressure RF CCP simulation is conducted by Turner *et al.* in [68]. In this study, they introduced a benchmark problem with well-defined physical and numerical conditions. Then, they applied five independently established different simulations to that problem, some developed in different programming languages and even with different architectures, and compared the results of various parameters by determining whether those different simulations generate statistically indistinguishable outputs. They also examined the effects of various numerical parameters to specify any remaining ambiguity of the benchmark data and shared all output data in the electronic supplement of their paper. Hence, it is an excellent reference study for validation and verification of the model developed in the present study.

Turner et al. [68] developed their benchmark study for low-pressure capacitive discharge in helium, at a sinusoidally varying voltage of frequency 13.56 MHz, so that the simulations would be associated with experiments of Godyak *et al.* [141]. Hence, the code developed in this study is rearranged to conform with this benchmark study. The conditions are taken to be identical in terms of physical and computational parameters. The details of the benchmark conditions are already given in [68], yet some of the basic parameters are illustrated in Table 4.2. In all simulation cases, data collection for these parameters is conducted for the last 32 RF cycles of the simulation.

Table 4.2: Basic parameters of benchmark in [68].

Parameter	**Symbol**	**Case 1**	**Case 2**	**Case 3**
Discharge gap	L [cm]	6.7	6.7	6.7
Background gas pressure	p [Torr]	0.03	0.1	0.3
Background gas temperature	T [K]	300	300	300
Discharge voltage	V [V]	450	200	150
Simulation time	t [s]	$1280/f$	$5120/f$	$5120/f$
Cell size	Δx [m]	$L/128$	$L/256$	$L/512$
Time step size	Δt [s]	$(400f)^{-1}$	$(800f)^{-1}$	$(1600f)^{-1}$
Particle weight	W	26172	52344	52344

In the benchmark study, Biagi-v7.1 database [142] is used for electron-neutral collisions. In the present study, the same cross section set is utilized implementing linear interpolation for intermediate values of electron energy. LUTs are constructed, via another Fortran code, for energies from 0 to 1000 eV, with a resolution of 0.001 eV, and supplied to the programme code just as in the previously applied procedure. The Biagi-v7.1 database includes one cross-section set for the elastic momentum transfer process, two sets for the excitation (singlet and triplet) process, and one set for the ionization process, all of which suppose that the collisions result in isotropic scattering in the centre of mass frame. Hence, the portion of the programme code which deals with collisions is adapted to follow that presumption. The plasma-chemical model for electron-neutral collisions is given in Table 4.3.

Table 4.3: Plasma-chemical model of the electron-neutral collisions in the benchmark study.

Process	**Reaction**	**Threshold Energy (eV)**
Elastic Scattering	$e^- + He \rightarrow He + e^-$	–
Excitation (Triplet)	$e^- + He \rightarrow He^*(2^3S_1) + e^-$	19.82
Excitation (Singlet)	$e^- + He \rightarrow He^*(2^1S_0) + e^-$	20.61
Ionization	$e^- + He \rightarrow He^+ + e^- + e^-$	24.587

Table 4.4: Relative errors for some basic physical parameters of the discharge in comparison to reference values given in [68]. The values of the ion density n_i and the electron temperature T_e are evaluated at the centre of the discharge region. S_e and S_i are the line integrals of electrical power of electrons and ions through the discharge region, respectively. Ion current J_i is calculated at the grounded electrode.

Physical Parameter	**Relative Error (%)**		
	Case 1	**Case 2**	**Case 3**
n_i	1.43	0.966	0.552
k_BT_e	4.38	0.213	0.506
S_e	2.92	1.55	3.05
S_i	2.32	2.31	1.88
J_i	0.457	0.465	0.513

In the case of an ionization collision, the residual energy is shared in half by the scattered and ejected (i.e., newly created) electrons. For ion-neutral collisions, on the other hand, the benchmark study used Phelps' proposal [136] of approximating the anisotropic scattering by two components: isotropic scattering component and backward scattering component. Corresponding cross section data set for He are available in [143] as well as an analytical expression as a function of relative energy of the colliding partners, in the centre of mass frame. The latter is utilized in the present study. Note that all cross section data assume collisions of ions and neutrals in the centre of mass frame, as well.

Table 4.5: Relative errors for some basic numerical parameters of the discharge in comparison to reference values given in [68]. The time-averaged values are taken at the centre of the discharge, except N_P. N_P is the total number of super particles in the discharge region.

Numerical Parameter	**Relative Error (%)**		
	Case 1	**Case 2**	**Case 3**
$\omega_p \Delta t$	2.48	0.667	< 0.001
$\lambda_D / \Delta x$	0.269	0.467	0.376
N_D	12.0	9.93	21.3
N_P	1.43	1.27	1.21

The handling of the ion-neutral collisions is done according to the procedure given in Section 4.2. In the determination of the deflection angles and relative velocities of electron-neutral collisions, the procedure given in Section 3.2 is followed. The only difference is in the sharing of the residual energy between the scattered and ejected electrons in the ionization case, as mentioned above.

The results for some basic physical parameters are illustrated in Table 4.4 along with the corresponding values given in the reference benchmark study in [68]. Note that n_i is the value of ion density at the middle of the discharge region, S_e and S_i are the line integrals of electrical power of electrons and ions, and J_i is the ion current density at the grounded electrode. All these values are calculated at the end of simulation.

In Table 4.5, on the other hand, the results for some basic numerical parameters are given. Similarly, all the values there belong to the middle of the discharge region as well. Time-averaged values of density and mean electron energy in the middle of discharge region are used to calculate the plasma frequency, Debye length, and the

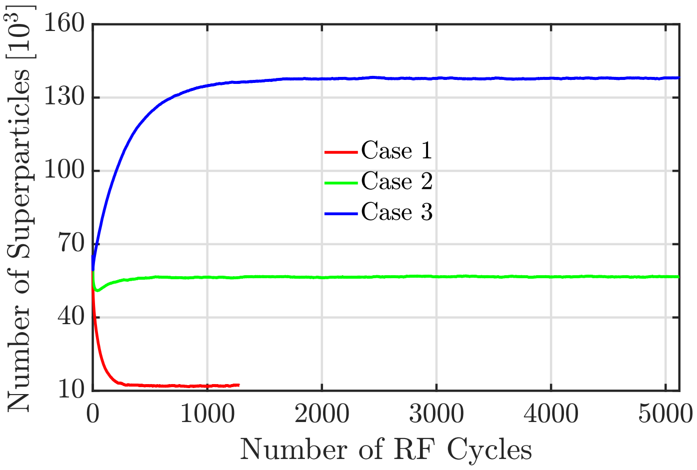

Figure 4.5: Time evolution of number of superparticles.

related numerical parameters. ν_e and ν_i, as given in the reference benchmark study, are taken as the maximum electron and ion collision frequencies for the null collision procedure in the present study. N_D is the number of superparticles per Debye length.

In Figure 4.6, ion number densities are compared with the reference study [68] results. In that reference study [68], originally, the results of five different codes were compared with each other. It was shown that the results of each code demonstrated a fluctuation around some value, called mean value. Thus, for benchmarking purposes, error bar representations of the results for one standard deviation of the fluctuations were given. Corresponding data were also given in the electronic supplement of the study. Hence, for comparison, mean ion densities and population standard deviation are taken as reference given in that electronic supplement. The curves given in Figure 4.6 suggest a good agreement in ion densities. In order to provide a more convincing result, this agreement can also be shown quantitatively by calculating the maximum relative errors in ion densities with respect to the mean ion densities given in the electronic supplement. In Table 4.6 are the results for such an evaluation which exhibit maximum relative errors of about 3% for each case. The correspondence of the results will also be shown statistically below.

In Figures 4.7, 4.8, and 4.9, period-averaged values of the ionization source term $R_{ion.}$, power density of electrons P_e, and power density of ions P_i are compared, respectively. In these figures a good agreement of the curves is observed, as well. In

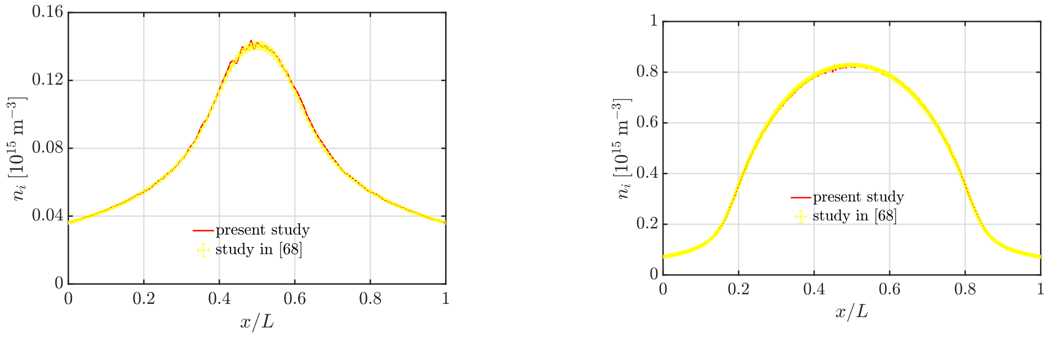

(a) Case 1

(b) Case 2

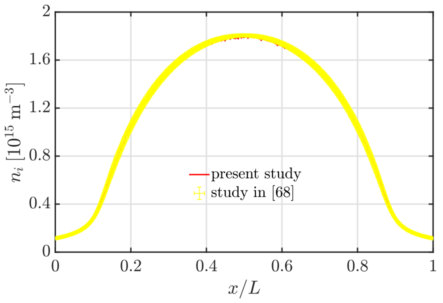

(c) Case 3

Figure 4.6: Distribution of ion number densities in comparison to results from [68].

each of these figures, it is obvious that ionization source and power densities tend to concentrate in sheath regions as the pressure is increased.

In Figure 4.10, temporally and spatially averaged results of electron energy probability function (EEPF) are compared. A good agreement is obtained in all figures and cases. Note that EEPF is normalized as $\int_0^\infty f(\varepsilon)\sqrt{\varepsilon}d\varepsilon = 1$. It is observed in Figure 4.10 that the shape of EEPF becomes less like a Maxwellian one as the pressure increases. This suggests that it is less likely for approximate models, such as fluid model, to yield sufficiently accurate results and the need for a kinetic model becomes more pronounced as the pressure increases.

Let us now evaluate the correspondence of reference benchmark [68] and current study results on a statistical basis. Due to the stochastic nature of PIC/MCC method, even the same codes may yield somehow different results when implemented in various computers. Hence, it is suggested in [68] that to compare various implementa-

Table 4.6: The maximum relative errors in ion number densities with respect to the reference values from [68].

	Maximum relative error in ion number densities ($\%$)
Case 1	2.98
Case 2	2.77
Case 3	3.06

tions with the benchmark study, a test of *statistical distinguishability* can be applied. According to that, ion densities are considered as random variables. As long as these densities at each grid points can be expressed with an average value and a standard deviation, a suitable distribution can be constructed against which any other results can be compared. These average and standard deviation values are obtained by using the results of one of the programme codes taking part in the study and presented in the electronic supplement of [68]. In this analysis, the ratios of deviation squares to the expectation of these deviation squares are summed through all grid points. This value is represented by a so-called X^2 value. Then, after normalization process, a distribution function $f(X^2)$ is obtained for each case. If the X^2 values obtained from any other simulation results fall into these distributions, then the results of that simulation are said to be statistically indistinguishable from those of the benchmark study in [68].

In Table 4.7 , X^2 values obtained in the present study are given along with the interval of values corresponding to 99% of the area under the distributions obtained in [68]. The results suggest a strong evidence that the programme code developed in the present study gives results that are statistically indistinguishable from the results of the benchmark study in [68].

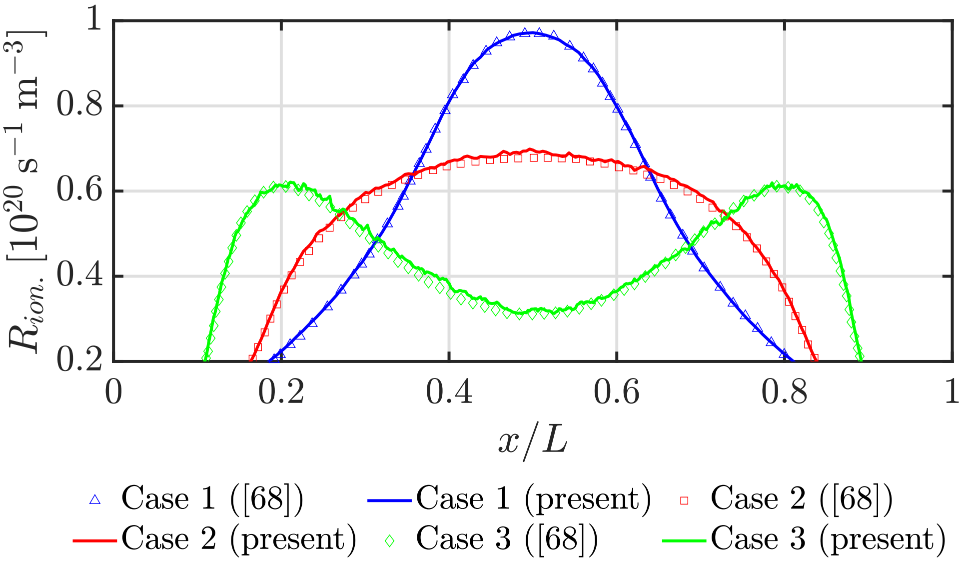

Figure 4.7: Temporally averaged ionization source terms in comparison to results from [68].

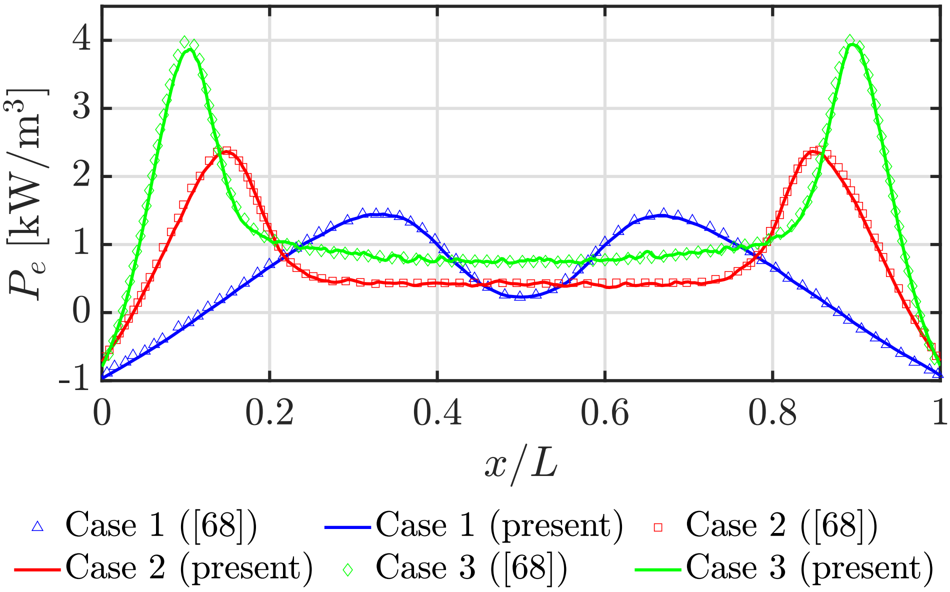

Figure 4.8: Temporally averaged electron power densities in comparison to results from [68].

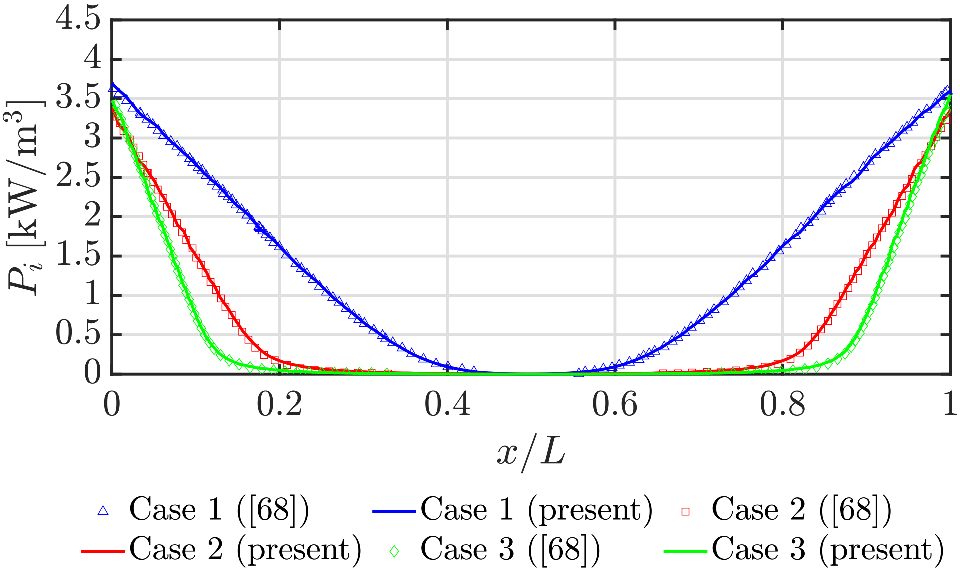

Figure 4.9: Temporally averaged ion power densities in comparison to results from [68].

Table 4.7: Comparison of X^2 values for the statistical distinguishability test with benchmark study from [68]. Given in the second line are the ranges of values that cover 99% of the area under the X^2 distributions given in [68].

	Case 1	**Case 2**	**Case 3**
Current study	94	351	689
Benchmark study [68]	$48 - 405$	$160 - 548$	$382 - 798$

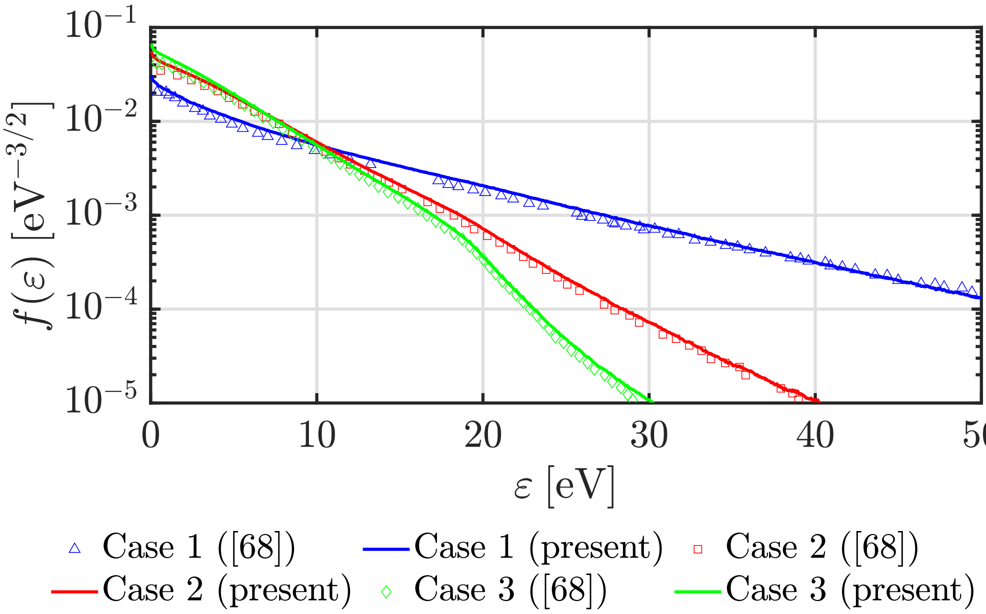

Figure 4.10: Temporally and spatially averaged electron energy probability functions in comparison to results from [68].

CHAPTER 5

CONCLUSIONS

In this thesis, the main motivation is to develop and verify a Particle-in-cell/Monte Carlo Collision (PIC/MCC) simulation procedure and code in Fortran programming language. To this end, a modular approach is followed. That is, the procedure is broken up into smaller and simpler subsections. Each subsection is carefully constructed and verified independently before combining the all.

First, the PIC module of the simulation is developed and tested for the two-stream instability (TSI) problem given in [94]. Electron distributions in the phase space that are obtained in [94] and the present study are compared. Time evolution of several parameters are also investigated. It is also checked if an instability develops when theoretically no instability expected. A good agreement is observed with the results of [94] and the analytical results.

Next, the MCC module of the method is considered. After the theoretical and numerical background is presented the code is verified with the electron transport in steady-state Townsend discharge (SSTD) with constant electric field, given in [95]. Even though the approaches of the two studies are different, similar results are obtained. Error bar analyses of the transport parameters showed that the results are not different more than 15%. Electron velocity distribution function (VDF) results yielded similar behaviours, as well.

Finally, all developed and verified modules are combined into a self-consistent PIC/MCC numerical code. The code is first verified with the eduPIC code results for the radiofrequency capacitively coupled plasma (RF CCP) in argon discharge given in [87]. The results of the two studies showed excellent conformity. Furthermore, the code is benchmarked with the simulations of RF CCP in helium for various conditions given in [68]. Relative errors for the physical and numerical parameters of the present study in comparison to the reference study are given. Ion number densities are also tested in a statistical distinguishability test that is suggested in [68]. According to that, it is shown that the simulation results obtained in the present study are drawn from the same distribution of the reference study and thus it is concluded that the numerical code developed in this thesis study is successfully verified and can be used for further implementations in future works.

REFERENCES

[1] A. Grzybowski and K. Pietrzak, “Jan evangelista purkynje (1787–1869)”, *Journal of Neurology*, vol. 261, no. 10, pp. 2048–2050, Oct. 2014.

[2] I. Langmuir, “Oscillations in ionized gases”, *Proceedings of the National Academy of Sciences*, vol. 14, no. 8, pp. 627–637, 1928.

[3] W. Crookes, “On radiant matter”, *Journal of the Franklin Institute*, vol. 108, no. 5, pp. 305–316, 1879, ISSN: 0016-0032. DOI: `https://doi.org/10.1016/0016-0032(79)90319-3`. [Online]. Available: `https://www.sciencedirect.com/science/article/pii/0016003279903193`.

[4] D. A. Gurnett and A. Bhattacharjee, “Characteristic parameters of a plasma”, in *Introduction to Plasma Physics: With Space, Laboratory and Astrophysical Applications*, 2nd ed. Cambridge University Press, 2017, p. 10. DOI: `10.1017/9781139226059.003`.

[5] L. Tonks and I. Langmuir, “Oscillations in ionized gases”, *Phys. Rev.*, vol. 33, pp. 195–210, 2 Feb. 1929. DOI: `10.1103/PhysRev.33.195`. [Online]. Available: `https://link.aps.org/doi/10.1103/PhysRev.33.195`.

[6] M. M. Hatami, M. Tribeche, and A. A. Mamun, “Debye length and electric potential in magnetized nonextensive plasma”, *Physics of Plasmas*, vol. 25, no. 9, p. 094 502, 2018. DOI: `10.1063/1.5036760`. eprint: `https://doi.org/10.1063/1.5036760`. [Online]. Available: `https://doi.org/10.1063/1.5036760`.

[7] U. S. Inan and M. Gołkowski, “Introduction”, in *Principles of Plasma Physics for Engineers and Scientists*. Cambridge University Press, 2010, p. 4. DOI: `10.1017/CBO9780511761621.002`.

[8] H. Alfven and G. Arrhenius, “Plasma physics and hetegony”, in *Evolution of the Solar System*. University Press of the Pacific, 2004, p. 252, ISBN: 9781410218841. [Online]. Available: `https://books.google.com.tr/books?id=v1CCPwAACAAJ`.

[9] “Particle drifts in uniform fields”, in *Introduction to Plasma Physics*. Taylor & Francis Group, 1995, ch. 2, p. 24, ISBN: 978-0-7503-0183-1. [Online]. Available: `https://doi.org/10.1201/9780367806958`.

[10] J. Ongena, R. Koch, R. Wolf, and H. Zohm, “Magnetic-confinement fusion”, *Nature Physics*, vol. 12, no. 5, pp. 398–410, May 2016. DOI: `10.1038/nphys3745`. [Online]. Available: `https://doi.org/10.1038/nphys3745`.

[11] M. Barbarino, “A brief history of nuclear fusion”, *Nature Physics*, vol. 16, no. 9, pp. 890–893, Jun. 2020. DOI: `10.1038/s41567-020-0940-7`. [Online]. Available: `https://doi.org/10.1038/s41567-020-0940-7`.

[12] F. F. Chen, “Introduction”, in *Introduction to Plasma Physics and Controlled Fusion*. Cham: Springer International Publishing, 2016, p. 6, ISBN: 978-3-319-22309-4. DOI: `10.1007/978-3-319-22309-4_1`. [Online]. Available: `https://doi.org/10.1007/978-3-319-22309-4_1`.

[13] A. J. L. Michael A. Lieberman, *Principles of Plasma Discharges and Materials Processing*, Second Edition. Hoboken, New Jersey: John Wiley & Sons, Ltd, 2005. DOI: `https://doi.org/10.1002/0471724254`. [Online]. Available: `https://onlinelibrary.wiley.com/doi/book/10.1002/0471724254`.

[14] R. Snoeckx and A. Bogaerts, “Plasma technology – a novel solution for co2 conversion?”, *Chem. Soc. Rev.*, vol. 46, pp. 5805–5863, 19 2017. DOI: `10.1039/C6CS00066E`. [Online]. Available: `http://dx.doi.org/10.1039/C6CS00066E`.

[15] E. Gomez, D. A. Rani, C. R. Cheeseman, D. Deegan, M. Wise, and A. R. Boccaccini, “Thermal plasma technology for the treatment of wastes: a critical review”, en, *J Hazard Mater*, vol. 161, no. 2-3, pp. 614–626, Apr. 2008.

[16] Y. Raizer, V. Kisin, and J. Allen, *Gas Discharge Physics*. Springer Berlin Heidelberg, 2011, ISBN: 9783642647604. [Online]. Available: `https://books.google.com.tr/books?id=zd-KMAEACAAJ`.

[17] S. T. Surzhikov, *A Mathematical Introduction*. Berlin, Boston: De Gruyter, 2020, ISBN: 9783110648836. DOI: `doi:10.1515/9783110648836`. [Online]. Available: `https://doi.org/10.1515/9783110648836`.

[18] J. T. Gudmundsson and A. Hecimovic, "Foundations of dc plasma sources", *Plasma Sources Science and Technology*, vol. 26, no. 12, p. 123 001, Nov. 2017. DOI: `10.1088/1361-6595/aa940d`. [Online]. Available: `https://dx.doi.org/10.1088/1361-6595/aa940d`.

[19] A. von Keudell and V. S.-v. der Gathen, "Foundations of low-temperature plasma physics—an introduction", *Plasma Sources Science and Technology*, vol. 26, no. 11, p. 113 001, Oct. 2017. DOI: `10.1088/1361-6595/aa8d4c`. [Online]. Available: `https://dx.doi.org/10.1088/1361-6595/aa8d4c`.

[20] D. Xiao, *Gas Discharge and Gas Insulation*. Springer Berlin, Heidelberg, 2016, ISBN: 978-3-662-48041-0. [Online]. Available: `https://doi.org/10.1007/978-3-662-48041-0`.

[21] B. M. Smirnov, *Theory of Gas Discharge Plasma*. Springer Cham, 2015, ISBN: 978-3-319-11065-3. [Online]. Available: `https://doi.org/10.1007/978-3-319-11065-3`.

[22] A. Bogaerts, E. Neyts, R. Gijbels, and J. van der Mullen, "Gas discharge plasmas and their applications", *Spectrochimica Acta Part B: Atomic Spectroscopy*, vol. 57, no. 4, pp. 609–658, 2002, ISSN: 0584-8547. DOI: `https://doi.org/10.1016/S0584-8547(01)00406-2`. [Online]. Available: `https://www.sciencedirect.com/science/article/pii/S0584854701004062`.

[23] S. Wilczek, J. Schulze, R. P. Brinkmann, Z. Donkó, J. Trieschmann, and T. Mussenbrock, "Electron dynamics in low pressure capacitively coupled radio frequency discharges", *Journal of Applied Physics*, vol. 127, no. 18, p. 181 101, 2020. DOI: `10.1063/5.0003114`. eprint: `https://doi.o`

rg/10.1063/5.0003114. [Online]. Available: https://doi.org/10.1063/5.0003114.

[24] M. A. Lieberman, “Plasma discharges for materials processing and display applications”, in *Advanced Technologies Based on Wave and Beam Generated Plasmas*, H. Schlüter and A. Shivarova, Eds. Dordrecht: Springer Netherlands, 1999, pp. 1–22, ISBN: 978-94-017-0633-9. DOI: 10.1007/978-94-017-0633-9_1. [Online]. Available: https://doi.org/10.1007/978-94-017-0633-9_1.

[25] H. Zeghioud, P. Nguyen-Tri, L. Khezami, A. Amrane, and A. A. Assadi, “Review on discharge plasma for water treatment: mechanism, reactor geometries, active species and combined processes”, *Journal of Water Process Engineering*, vol. 38, p. 101 664, 2020, ISSN: 2214-7144. DOI: https://doi.org/10.1016/j.jwpe.2020.101664. [Online]. Available: https://www.sciencedirect.com/science/article/pii/S2214714420305420.

[26] W. Y. L. Ling, S. Zhang, H. Fu, *et al.*, “A brief review of alternative propellants and requirements for pulsed plasma thrusters in micropropulsion applications”, *Chinese Journal of Aeronautics*, vol. 33, no. 12, pp. 2999–3010, 2020, ISSN: 1000-9361. DOI: https://doi.org/10.1016/j.cja.2020.03.024. [Online]. Available: https://www.sciencedirect.com/science/article/pii/S1000936120302065.

[27] S. N. Bathgate, M. M. M. Bilek, and D. R. McKenzie, “Electrodeless plasma thrusters for spacecraft: a review”, *Plasma Science and Technology*, vol. 19, no. 8, p. 083 001, Jun. 2017. DOI: 10.1088/2058-6272/aa71fe. [Online]. Available: https://dx.doi.org/10.1088/2058-6272/aa71fe.

[28] F. Taccogna and L. Garrigues, “Latest progress in hall thrusters plasma modelling”, *Reviews of Modern Plasma Physics*, vol. 3, pp. 1–63, 1 Jul. 2019, ISSN: 2367-3192. DOI: 10.1007/S41614-019-0033-1. [Online]. Available: https://link.springer.com/article/10.1007/s41614-019-0033-1.

[29] K. Polzin, A. Martin, J. Little, C. Promislow, B. Jorns, and J. Woods, “State-of-the-art and advancement paths for inductive pulsed plasma thrusters”, *Aerospace*, vol. 7, no. 8, 2020, ISSN: 2226-4310. DOI: `10.3390/aerospace7080105`. [Online]. Available: `https://www.mdpi.com/2226-4310/7/8/105`.

[30] K. Hara, “An overview of discharge plasma modeling for hall effect thrusters”, *Plasma Sources Science and Technology*, vol. 28, no. 4, p. 044 001, Apr. 2019. DOI: `10.1088/1361-6595/ab0f70`. [Online]. Available: `https://dx.doi.org/10.1088/1361-6595/ab0f70`.

[31] J.-P. Boeuf, “Tutorial: physics and modeling of hall thrusters”, *Journal of Applied Physics*, vol. 121, no. 1, p. 011 101, 2017. DOI: `10.1063/1.4972269`. eprint: `https://doi.org/10.1063/1.4972269`. [Online]. Available: `https://doi.org/10.1063/1.4972269`.

[32] A. I. Morozov and V. V. Savelyev, “Fundamentals of stationary plasma thruster theory”, in *Reviews of Plasma Physics*, B. B. Kadomtsev and V. D. Shafranov, Eds. Boston, MA: Springer US, 2000, pp. 203–391, ISBN: 978-1-4615-4309-1. DOI: `10.1007/978-1-4615-4309-1_2`. [Online]. Available: `https://doi.org/10.1007/978-1-4615-4309-1_2`.

[33] I. Adamovich, S. Agarwal, E. Ahedo, *et al.*, “The 2022 plasma roadmap: low temperature plasma science and technology”, *Journal of Physics D: Applied Physics*, vol. 55, no. 37, p. 373 001, Jul. 2022. DOI: `10.1088/1361-6463/ac5e1c`. [Online]. Available: `https://dx.doi.org/10.1088/1361-6463/ac5e1c`.

[34] A. V. Kazak, A. A. Kirillov, L. V. Simonchik, *et al.*, “Bactericidal components in helium and air plasma jets of a dielectric barrier discharge”, *Journal of Applied Spectroscopy*, vol. 88, no. 2, pp. 293–298, May 2021.

[35] S. Bekeschus, T. von Woedtke, S. Emmert, and A. Schmidt, “Medical gas plasma-stimulated wound healing: evidence and mechanisms”, *Redox Biology*, vol. 46, p. 102 116, 2021, ISSN: 2213-2317. DOI: `https://doi.org/10.1016/j.redox.2021.102116`. [Online]. Available: `https://www.sciencedirect.com/science/article/pii/S2213231721002755`.

[36] I. Rafatov and A. Kudryavtsev, “Modeling approaches for gas discharge plasmas”, in *Introduction to Simulation Methods for Gas Discharge Plasmas*, ser. 2053-2563, IOP Publishing, 2020, 1-1 to 1–17, ISBN: 978-0-7503-2360-4. DOI: `10.1088/978-0-7503-2360-4ch1`. [Online]. Available: `https://dx.doi.org/10.1088/978-0-7503-2360-4ch1`.

[37] J. A. Rossmanith and D. C. Seal, “A positivity-preserving high-order semi-lagrangian discontinuous galerkin scheme for the vlasov–poisson equations”, *Journal of Computational Physics*, vol. 230, no. 16, pp. 6203–6232, 2011, ISSN: 0021-9991. DOI: `https://doi.org/10.1016/j.jcp.2011.04.018`. [Online]. Available: `https://www.sciencedirect.com/science/article/pii/S0021999111002579`.

[38] V. Kolobov and R. Arslanbekov, “Simulation of electron kinetics in gas discharges”, *IEEE Transactions on Plasma Science*, vol. 34, no. 3, pp. 895–909, 2006. DOI: `10.1109/TPS.2006.875850`.

[39] G. J. M. Hagelaar, “Coulomb collisions in the boltzmann equation for electrons in low-temperature gas discharge plasmas”, *Plasma Sources Science and Technology*, vol. 25, no. 1, p. 015015, Dec. 2015. DOI: `10.1088/0963-0252/25/1/015015`. [Online]. Available: `https://dx.doi.org/10.1088/0963-0252/25/1/015015`.

[40] C. Yuan, E. A. Bogdanov, S. I. Eliseev, and A. A. Kudryavtsev, “1d kinetic simulations of a short glow discharge in helium”, *Physics of Plasmas*, vol. 24, no. 7, p. 073507, 2017. DOI: `10.1063/1.4990030`. eprint: `https://doi.org/10.1063/1.4990030`. [Online]. Available: `https://doi.org/10.1063/1.4990030`.

[41] H. C. Kim, F. Iza, S. S. Yang, M. Radmilović-Radjenović, and J. K. Lee, “Particle and fluid simulations of low-temperature plasma discharges: benchmarks and kinetic effects”, *Journal of Physics D: Applied Physics*, vol. 38, no. 19, R283, Sep. 2005. DOI: `10.1088/0022-3727/38/19/R01`. [Online]. Available: `https://dx.doi.org/10.1088/0022-3727/38/19/R01`.

[42] A. Bogaerts, R. Gijbels, and W. Goedheer, “Comparison between a radio-frequency and direct current glow discharge in argon by a hybrid monte

carlo–fluid model for electrons, argon ions and fast argon atoms", *Spectrochimica Acta Part B: Atomic Spectroscopy*, vol. 54, no. 9, pp. 1335–1350, 1999, ISSN: 0584-8547. DOI: `https://doi.org/10.1016/S0584-8547(99)00080-4`. [Online]. Available: `https://www.sciencedirect.com/science/article/pii/S0584854799000804`.

[43] E. Eylenceoğlu, I. Rafatov, and A. A. Kudryavtsev, "Two-dimensional hybrid monte carlo–fluid modelling of dc glow discharges: comparison with fluid models, reliability, and accuracy", *Physics of Plasmas*, vol. 22, no. 1, p. 013 509, 2015. DOI: `10.1063/1.4906361`. eprint: `https://doi.org/10.1063/1.4906361`. [Online]. Available: `https://doi.org/10.1063/1.4906361`.

[44] J. P. Boeuf and L. C. Pitchford, "Field reversal in the negative glow of a dc glow discharge", *Journal of Physics D: Applied Physics*, vol. 28, no. 10, p. 2083, Oct. 1995. DOI: `10.1088/0022-3727/28/10/013`. [Online]. Available: `https://dx.doi.org/10.1088/0022-3727/28/10/013`.

[45] A. Derzsi, P. Hartmann, I. Korolov, J. Karácsony, G. Bánó, and Z. Donkó, "On the accuracy and limitations of fluid models of the cathode region of dc glow discharges", *Journal of Physics D: Applied Physics*, vol. 42, no. 22, p. 225 204, Oct. 2009. DOI: `10.1088/0022-3727/42/22/225204`. [Online]. Available: `https://dx.doi.org/10.1088/0022-3727/42/22/225204`.

[46] O. Buneman, "Dissipation of currents in ionized media", *Phys. Rev.*, vol. 115, pp. 503–517, 3 Aug. 1959. DOI: `10.1103/PhysRev.115.503`. [Online]. Available: `https://link.aps.org/doi/10.1103/PhysRev.115.503`.

[47] J. Dawson, "One-dimensional plasma model", *The Physics of Fluids*, vol. 5, no. 4, pp. 445–459, 1962. DOI: `10.1063/1.1706638`. eprint: `https://aip.scitation.org/doi/pdf/10.1063/1.1706638`. [Online]. Available: `https://aip.scitation.org/doi/abs/10.1063/1.1706638`.

[48] C. Birdsall, "Particle-in-cell charged-particle simulations, plus monte carlo collisions with neutral atoms, pic-mcc", *IEEE Transactions on Plasma Science*, vol. 19, no. 2, pp. 65–85, 1991. DOI: `10.1109/27.106800`.

[49] R. W. Hockney and J. W. Eastwood, *Computer simulation using particles*. Bristol: Hilger, 1988.

[50] J. M. Dawson, "Thermal relaxation in a one-species, one-dimensional plasma", *The Physics of Fluids*, vol. 7, no. 3, pp. 419–425, 1964. DOI: `10.1063/1.1711214`. eprint: `https://aip.scitation.org/doi/pdf/10.1063/1.1711214`. [Online]. Available: `https://aip.scitation.org/doi/abs/10.1063/1.1711214`.

[51] R. W. Hockney, "A fast direct solution of poisson's equation using fourier analysis", *Journal of the ACM (JACM)*, vol. 12, no. 1, pp. 95–113, 1965.

[52] P. L. Auer, H. Hurwitz, and R. W. Kilb, "Large-amplitude magnetic compression of a collision-free plasma. ii. development of a thermalized plasma", *The Physics of Fluids*, vol. 5, no. 3, pp. 298–316, 1962. DOI: `10.1063/1.1706615`. eprint: `https://aip.scitation.org/doi/pdf/10.1063/1.1706615`. [Online]. Available: `https://aip.scitation.org/doi/abs/10.1063/1.1706615`.

[53] A. Hasegawa and C. K. Birdsall, "Sheet-current plasma model for ion-cyclotron waves", *The Physics of Fluids*, vol. 7, no. 10, pp. 1590–1600, 1964. DOI: `10.1063/1.1711064`. eprint: `https://aip.scitation.org/doi/pdf/10.1063/1.1711064`. [Online]. Available: `https://aip.scitation.org/doi/abs/10.1063/1.1711064`.

[54] P. Burger, "Elastic collisions in simulating one-dimensional plasma diodes on the computer", *The Physics of Fluids*, vol. 10, no. 3, pp. 658–666, 1967. DOI: `10.1063/1.1762162`. eprint: `https://aip.scitation.org/doi/pdf/10.1063/1.1762162`. [Online]. Available: `https://aip.scitation.org/doi/abs/10.1063/1.1762162`.

[55] R. Shanny, J. M. Dawson, and J. M. Greene, "One-dimensional model of a lorentz plasma", *The Physics of Fluids*, vol. 10, no. 6, pp. 1281–1287, 1967. DOI: `10.1063/1.1762273`. eprint: `https://aip.scitation.org`

/doi/pdf/10.1063/1.1762273. [Online]. Available: https://aip.scitation.org/doi/abs/10.1063/1.1762273.

[56] H. R. Skullerud, “The stochastic computer simulation of ion motion in a gas subjected to a constant electric field”, *Journal of Physics D: Applied Physics*, vol. 1, no. 11, p. 1567, Nov. 1968. DOI: 10.1088/0022-3727/1/11/423. [Online]. Available: https://dx.doi.org/10.1088/0022-3727/1/11/423.

[57] S. L. Lin and J. N. Bardsley, “Monte carlo simulation of ion motion in drift tubes”, *The Journal of Chemical Physics*, vol. 66, no. 2, pp. 435–445, 1977. DOI: 10.1063/1.433988. eprint: https://doi.org/10.1063/1.433988. [Online]. Available: https://doi.org/10.1063/1.433988.

[58] T. Takizuka and H. Abe, “A binary collision model for plasma simulation with a particle code”, *Journal of Computational Physics*, vol. 25, no. 3, pp. 205–219, 1977, ISSN: 0021-9991. DOI: https://doi.org/10.1016/0021-9991(77)90099-7. [Online]. Available: https://www.sciencedirect.com/science/article/pii/0021999177900997.

[59] J. Eastwood, R. Hockney, and D. Lawrence, “P3m3dp—the three-dimensional periodic particle-particle/ particle-mesh program”, *Computer Physics Communications*, vol. 19, no. 2, pp. 215–261, 1980, ISSN: 0010-4655. DOI: https://doi.org/10.1016/0010-4655(80)90052-1. [Online]. Available: https://www.sciencedirect.com/science/article/pii/0010465580900521.

[60] R. Procassini, C. K. Birdsall, E. Morse, and B. Cohen, “A relativistic monte carlo binary collision model for use in plasma particle simulation codes”, EECS Department, University of California, Berkeley, Tech. Rep. UCB/ERL M87/24, May 1987. [Online]. Available: http://www2.eecs.berkeley.edu/Pubs/TechRpts/1987/861.html.

[61] R. W. Boswell and I. J. Morey, “Self-consistent simulation of a parallel-plate rf discharge”, *Applied Physics Letters*, vol. 52, no. 1, pp. 21–23, 1988. DOI: 10.1063/1.99327. eprint: https://doi.org/10.1063/1.99327. [Online]. Available: https://doi.org/10.1063/1.99327.

[62] M. Surendra, D. B. Graves, and G. M. Jellum, “Self-consistent model of a direct-current glow discharge: treatment of fast electrons”, *Phys. Rev. A*, vol. 41, pp. 1112–1125, 2 Jan. 1990. DOI: `10.1103/PhysRevA.41.1112`. [Online]. Available: `https://link.aps.org/doi/10.1103/PhysRevA.41.1112`.

[63] M. Surendra and D. Graves, “Particle simulations of radio-frequency glow discharges”, *IEEE Transactions on Plasma Science*, vol. 19, no. 2, pp. 144–157, 1991. DOI: `10.1109/27.106808`.

[64] D. Vender and R. Boswell, “Numerical modeling of low-pressure rf plasmas”, *IEEE Transactions on Plasma Science*, vol. 18, no. 4, pp. 725–732, 1990. DOI: `10.1109/27.57527`.

[65] D. Vender, “Numerical studies of the low pressure rf plasma”, Ph.D. dissertation, The Australian National University, 1990.

[66] C. Birdsall and A. Langdon, *Plasma Physics via Computer Simulation* (Series in Plasma Physics and Fluid Dynamics). Taylor & Francis, 2004, ISBN: 9780750310253. [Online]. Available: `https://books.google.com.tr/books?id=S2lqgDTm6a4C`.

[67] M. Surendra, “Radiofrequency discharge benchmark model comparison”, *Plasma Sources Science and Technology*, vol. 4, no. 1, p. 56, Feb. 1995. DOI: `10.1088/0963-0252/4/1/007`. [Online]. Available: `https://dx.doi.org/10.1088/0963-0252/4/1/007`.

[68] M. M. Turner, A. Derzsi, Z. Donkó, *et al.*, “Simulation benchmarks for low-pressure plasmas: capacitive discharges”, *Physics of Plasmas*, vol. 20, no. 1, p. 013 507, 2013. DOI: `10.1063/1.4775084`. eprint: `https://doi.org/10.1063/1.4775084`. [Online]. Available: `https://doi.org/10.1063/1.4775084`.

[69] D. Sydorenko, A. Smolyakov, I. Kaganovich, and Y. Raitses, “Kinetic simulation of secondary electron emission effects in hall thrusters”, *Physics of Plasmas*, vol. 13, no. 1, p. 014 501, 2006. DOI: `10.1063/1.2158698`. eprint: `https://doi.org/10.1063/1.2158698`. [Online]. Available: `https://doi.org/10.1063/1.2158698`.

[70] F. Taccogna, R. Schneider, S. Longo, and M. Capitelli, “Kinetic simulations of a plasma thruster”, *Plasma Sources Science and Technology*, vol. 17, no. 2, p. 024 003, May 2008. DOI: `10.1088/0963-0252/17/2/024003`. [Online]. Available: `https://dx.doi.org/10.1088/0963-0252/17/2/024003`.

[71] T. Lafleur, S. D. Baalrud, and P. Chabert, “Theory for the anomalous electron transport in hall effect thrusters. ii. kinetic model”, *Physics of Plasmas*, vol. 23, no. 5, p. 053 503, 2016. DOI: `10.1063/1.4948496`. eprint: `https://doi.org/10.1063/1.4948496`. [Online]. Available: `https://doi.org/10.1063/1.4948496`.

[72] V. Georgieva, A. Bogaerts, and R. Gijbels, “Numerical investigation of ion-energy-distribution functions in single and dual frequency capacitively coupled plasma reactors”, *Phys. Rev. E*, vol. 69, p. 026 406, 2 Feb. 2004. DOI: `10.1103/PhysRevE.69.026406`. [Online]. Available: `https://link.aps.org/doi/10.1103/PhysRevE.69.026406`.

[73] J. K. Lee, O. V. Manuilenko, N. Y. Babaeva, H. C. Kim, and J. W. Shon, “Ion energy distribution control in single and dual frequency capacitive plasma sources”, *Plasma Sources Science and Technology*, vol. 14, no. 1, p. 89, Jan. 2005. DOI: `10.1088/0963-0252/14/1/012`. [Online]. Available: `https://dx.doi.org/10.1088/0963-0252/14/1/012`.

[74] S. Wang, X. Xu, and Y.-N. Wang, “Numerical investigation of ion energy distribution and ion angle distribution in a dual-frequency capacitively coupled plasma with a hybrid model”, *Physics of Plasmas*, vol. 14, no. 11, p. 113 501, 2007. DOI: `10.1063/1.2780136`. eprint: `https://doi.org/10.1063/1.2780136`. [Online]. Available: `https://doi.org/10.1063/1.2780136`.

[75] Z. Donkó, A. Derzsi, M. Vass, J. Schulze, E. Schuengel, and S. Hamaguchi, “Ion energy and angular distributions in low-pressure capacitive oxygen rf discharges driven by tailored voltage waveforms”, *Plasma Sources Science and Technology*, vol. 27, no. 10, p. 104 008, Oct. 2018. DOI: `10.1088/1361-6595/aae5c3`. [Online]. Available: `https://dx.doi.org/10.1088/1361-6595/aae5c3`.

[76] D. O'Connell, R. Zorat, A. R. Ellingboe, and M. M. Turner, "Comparison of measurements and particle-in-cell simulations of ion energy distribution functions in a capacitively coupled radio-frequency discharge", *Physics of Plasmas*, vol. 14, no. 10, p. 103 510, 2007. DOI: `10.1063/1.2795634`. eprint: `https://doi.org/10.1063/1.2795634`. [Online]. Available: `https://doi.org/10.1063/1.2795634`.

[77] T. Lafleur, P. Chabert, and J. P. Booth, "Electron heating in capacitively coupled plasmas revisited", *Plasma Sources Science and Technology*, vol. 23, no. 3, p. 035 010, May 2014. DOI: `10.1088/0963-0252/23/3/035010`. [Online]. Available: `https://dx.doi.org/10.1088/0963-0252/23/3/035010`.

[78] G.-H. Liu, Y.-X. Liu, D.-Q. Wen, and Y.-N. Wang, "Heating mode transition in capacitively coupled cf4 discharges: comparison of experiments with simulations", *Plasma Sources Science and Technology*, vol. 24, no. 3, p. 034 006, May 2015. DOI: `10.1088/0963-0252/24/3/034006`. [Online]. Available: `https://dx.doi.org/10.1088/0963-0252/24/3/034006`.

[79] J. Schulze, Z. Donkó, T. Lafleur, S. Wilczek, and R. P. Brinkmann, "Spatio-temporal analysis of the electron power absorption in electropositive capacitive rf plasmas based on moments of the boltzmann equation", *Plasma Sources Science and Technology*, vol. 27, no. 5, p. 055 010, May 2018. DOI: `10.1088/1361-6595/aabebc`. [Online]. Available: `https://dx.doi.org/10.1088/1361-6595/aabebc`.

[80] M. Vass, S. Wilczek, T. Lafleur, R. P. Brinkmann, Z. Donkó, and J. Schulze, "Electron power absorption in low pressure capacitively coupled electronegative oxygen radio frequency plasmas", *Plasma Sources Science and Technology*, vol. 29, no. 2, p. 025 019, Feb. 2020. DOI: `10.1088/1361-6595/ab5f27`. [Online]. Available: `https://dx.doi.org/10.1088/1361-6595/ab5f27`.

[81] Z. Donkó, J. Schulze, U. Czarnetzki, and D. Luggenhölscher, "Self-excited nonlinear plasma series resonance oscillations in geometrically symmetric capacitively coupled radio frequency discharges", *Applied Physics Letters*,

vol. 94, no. 13, p. 131 501, 2009. DOI: 10.1063/1.3110056. eprint: https://doi.org/10.1063/1.3110056. [Online]. Available: https://doi.org/10.1063/1.3110056.

[82] E. Schüngel, S. Brandt, I. Korolov, A. Derzsi, Z. Donkó, and J. Schulze, "On the self-excitation mechanisms of plasma series resonance oscillations in single- and multi-frequency capacitive discharges", *Physics of Plasmas*, vol. 22, no. 4, p. 043 512, 2015. DOI: 10.1063/1.4918702. eprint: https://doi.org/10.1063/1.4918702. [Online]. Available: https://doi.org/10.1063/1.4918702.

[83] O. V. Proshina, T. V. Rakhimova, A. S. Kovalev, *et al.*, "Experimental and pic mcc study of electron cooling—re-heating and plasma density decay in low pressure rf ccp argon afterglow", *Plasma Sources Science and Technology*, vol. 29, no. 1, p. 015 015, Jan. 2020. DOI: 10.1088/1361-6595/ab5adb. [Online]. Available: https://dx.doi.org/10.1088/1361-6595/ab5adb.

[84] M. Daksha, A. Derzsi, S. Wilczek, *et al.*, "The effect of realistic heavy particle induced secondary electron emission coefficients on the electron power absorption dynamics in single- and dual-frequency capacitively coupled plasmas", *Plasma Sources Science and Technology*, vol. 26, no. 8, p. 085 006, Jul. 2017. DOI: 10.1088/1361-6595/aa7c88. [Online]. Available: https://dx.doi.org/10.1088/1361-6595/aa7c88.

[85] B. Horváth, M. Daksha, I. Korolov, A. Derzsi, and J. Schulze, "The role of electron induced secondary electron emission from sio2 surfaces in capacitively coupled radio frequency plasmas operated at low pressures", *Plasma Sources Science and Technology*, vol. 26, no. 12, p. 124 001, Nov. 2017. DOI: 10.1088/1361-6595/aa963d. [Online]. Available: https://dx.doi.org/10.1088/1361-6595/aa963d.

[86] B. Horváth, J. Schulze, Z. Donkó, and A. Derzsi, "The effect of electron induced secondary electrons on the characteristics of low-pressure capacitively coupled radio frequency plasmas", *Journal of Physics D: Applied Physics*, vol. 51, no. 35, p. 355 204, Aug. 2018. DOI: 10.1088/1361-6463/aad

47b. [Online]. Available: `https://dx.doi.org/10.1088/1361-6463/aad47b`.

[87] Z. Donkó, A. Derzsi, M. Vass, *et al.*, "eduPIC: an introductory particle based code for radio-frequency plasma simulation", *Plasma Sources Science and Technology*, vol. 30, no. 9, p. 095 017, Sep. 2021. DOI: `10.1088/1361-6595/ac0b55`. [Online]. Available: `https://doi.org/10.1088/1361-6595/ac0b55`.

[88] Z. Juhasz, J. Ďurian, A. Derzsi, Š. Matejčík, Z. Donkó, and P. Hartmann, "Efficient gpu implementation of the particle-in-cell/monte-carlo collisions method for 1d simulation of low-pressure capacitively coupled plasmas", *Computer Physics Communications*, vol. 263, p. 107 913, 2021, ISSN: 0010-4655. DOI: `https://doi.org/10.1016/j.cpc.2021.107913`. [Online]. Available: `https://www.sciencedirect.com/science/article/pii/S0010465521000503`.

[89] M. Y. Hur, J. S. Kim, I. C. Song, J. P. Verboncoeur, and H. J. Lee, "Model description of a two-dimensional electrostatic particle-in-cell simulation parallelized with a graphics processing unit for plasma discharges", *Plasma Research Express*, vol. 1, no. 1, p. 015 016, Mar. 2019. DOI: `10.1088/2516-1067/ab0918`. [Online]. Available: `https://dx.doi.org/10.1088/2516-1067/ab0918`.

[90] H. Shah, S. Kamaria, R. Markandeya, M. Shah, and B. Chaudhury, "A novel implementation of 2d3v particle-in-cell (pic) algorithm for kepler gpu architecture", in *2017 IEEE 24th International Conference on High Performance Computing (HiPC)*, 2017, pp. 378–387. DOI: `10.1109/HiPC.2017.00050`.

[91] A. Fierro, J. Dickens, and A. Neuber, "Graphics processing unit accelerated three-dimensional model for the simulation of pulsed low-temperature plasmas", *Physics of Plasmas*, vol. 21, no. 12, p. 123 504, 2014. DOI: `10.1063/1.4903330`. eprint: `https://doi.org/10.1063/1.4903330`. [Online]. Available: `https://doi.org/10.1063/1.4903330`.

[92] J. Claustre, B. Chaudhury, G. Fubiani, M. Paulin, and J. P. Boeuf, "Particle-in-cell monte carlo collision model on gpu—application to a low-temperature

magnetized plasma", *IEEE Transactions on Plasma Science*, vol. 41, no. 2, pp. 391–399, 2013. DOI: `10.1109/TPS.2012.2234402`.

[93] E. National Academies of Sciences and Medicine, *Plasma Science: Enabling Technology, Sustainability, Security, and Exploration*. Washington, DC: The National Academies Press, 2021, ISBN: 978-0-309-67760-8. DOI: `10.17226/25802`. [Online]. Available: `https://nap.nationalacademies.org/catalog/25802/plasma-science-enabling-technology-sustainability-security-and-exploration`.

[94] R. Fitzpatrick, *Computational physics*, Accessed: 03/03/2021, 2006. [Online]. Available: `https://farside.ph.utexas.edu/teaching/329/329.html`.

[95] Z. Donkó, "Particle simulation methods for studies of low-pressure plasma sources", *Plasma Sources Science and Technology*, vol. 20, p. 024 001, 2 Apr. 2011, ISSN: 09630252. DOI: `10.1088/0963-0252/20/2/024001`.

[96] "The vlasov equation", in *Introduction to Plasma Physics*. Taylor & Francis Group, 1995, ch. 22, pp. 387–394, ISBN: 978-0-7503-0183-1. [Online]. Available: `https://doi.org/10.1201/9780367806958`.

[97] C. K. Birdsall and D. Fuss, "Clouds-in-clouds, clouds-in-cells physics for many-body plasma simulation", *Journal of Computational Physics*, vol. 3, no. 4, pp. 494–511, 1969, ISSN: 0021-9991. DOI: `https://doi.org/10.1016/0021-9991(69)90058-8`. [Online]. Available: `https://www.sciencedirect.com/science/article/pii/0021999169900588`.

[98] M. Vass, P. Palla, and P. Hartmann, "Revisiting the numerical stability/accuracy conditions of explicit PIC/MCC simulations of low-temperature gas discharges", *Plasma Sources Science and Technology*, vol. 31, no. 6, p. 064 001, Jun. 2022. DOI: `10.1088/1361-6595/ac6e85`. [Online]. Available: `https://doi.org/10.1088/1361-6595/ac6e85`.

[99] E. M. Baroody, "A theory of secondary electron emission from metals", *Phys. Rev.*, vol. 78, pp. 780–787, 6 Jun. 1950. DOI: `10.1103/PhysRev.78.780`. [Online]. Available: `https://link.aps.org/doi/10.1103/PhysRev.78.780`.

[100] Z. Donkó, “Apparent secondary-electron emission coefficient and the voltage-current characteristics of argon glow discharges”, *Phys. Rev. E*, vol. 64, p. 026 401, 2 Jul. 2001. DOI: `10.1103/PhysRevE.64.026401`. [Online]. Available: `https://link.aps.org/doi/10.1103/PhysRevE.64.026401`.

[101] D. Mariotti, J. A. McLaughlin, and P. Maguire, “Experimental study of breakdown voltage and effective secondary electron emission coefficient for a micro-plasma device”, *Plasma Sources Science and Technology*, vol. 13, no. 2, p. 207, Feb. 2004. DOI: `10.1088/0963-0252/13/2/003`. [Online]. Available: `https://dx.doi.org/10.1088/0963-0252/13/2/003`.

[102] I. Korolov, A. Derzsi, Z. Donkó, E. Schüngel, and J. Schulze, “The influence of electron reflection/sticking coefficients at the electrodes on plasma parameters in particle-in-cell simulations of capacitive radio-frequency plasmas”, *Plasma Sources Science and Technology*, vol. 25, no. 1, p. 015 024, Jan. 2016. DOI: `10.1088/0963-0252/25/1/015024`. [Online]. Available: `https://dx.doi.org/10.1088/0963-0252/25/1/015024`.

[103] A. Sun, M. M. Becker, and D. Loffhagen, “Pic/mcc simulation of capacitively coupled discharges in helium: boundary effects”, *Plasma Sources Science and Technology*, vol. 27, no. 5, p. 054 002, May 2018. DOI: `10.1088/1361-6595/aac30a`. [Online]. Available: `https://dx.doi.org/10.1088/1361-6595/aac30a`.

[104] K. Schlegel and H. Thiemann, “Particle-in-cell plasma simulations of the modified two-stream instability”, *Ann. Geophys.*, vol. 12, pp. 1091–1100, 11 1994, ISSN: 1432-0576. [Online]. Available: `https://link.springer.com/article/10.1007/s00585-994-1091-3`.

[105] M. E. Dieckmann, P. K. Shukla, and L. O. C. Drury, “Particle-in-cell simulation studies of the non-linear evolution of ultrarelativistic two-stream instabilities”, *Mon. Not. R. Astron. Soc*, vol. 367, pp. 1072–1082, 2006. DOI: `10.1111/j.1365-2966.2006.10000.x`. [Online]. Available: `https://academic.oup.com/mnras/article/367/3/1072/1040044`.

[106] W. Mingyu, L. Quanming, Z. Jie, W. Peiran, and W. Shui, "Electromagnetic particle-in-cell simulations of electron holes formed during the electron two-stream instability", *Plasma Science and Technology*, vol. 15, pp. 17–24, 1 2013. DOI: `10.1088/1009-0630/15/1/04`.

[107] M. Ghorbanalilu, E. Abdollahzadeh, and S. H. E. Rahbari, "Particle-in-cell simulation of two stream instability in the non-extensive statistics", *Laser and Particle Beams, Cambridge University Press*, vol. 32, pp. 399–407, 2014. DOI: `10.1017/S0263034614000275`. [Online]. Available: `https://doi.org/10.1017/S0263034614000275`.

[108] R. Fitzpatrick, *Computational physics*, Accessed: 03/03/2021, 2006. [Online]. Available: `https://farside.ph.utexas.edu/teaching/329/329.html`.

[109] *Intel oneapi math kernel library developer reference 2021.4*, Accessed: 29/09/2021, 2021. [Online]. Available: `https://www.intel.com/content/www/us/en/develop/documentation/onemkl-developer-reference-fortran/top.html`.

[110] E. Erden and I. Rafatov, "Particle in cell/monte carlo collision method for simulation of rf glow discharges: effect of super particle weighting", *Contributions to Plasma Physics*, vol. 54, no. 7, pp. 626–634, 2014. DOI: `https://doi.org/10.1002/ctpp.201300047`. eprint: `https://onlinelibrary.wiley.com/doi/pdf/10.1002/ctpp.201300047`. [Online]. Available: `https://onlinelibrary.wiley.com/doi/abs/10.1002/ctpp.201300047`.

[111] A. Sun, M. M. Becker, and D. Loffhagen, "Pic/mcc simulation of capacitively coupled discharges: effect of particle management and integration", *Computer Physics Communications*, vol. 206, pp. 35–44, 2016, ISSN: 0010-4655. DOI: `https://doi.org/10.1016/j.cpc.2016.05.003`. [Online]. Available: `https://www.sciencedirect.com/science/article/pii/S0010465516301199`.

[112] M. M. Turner, "Kinetic properties of particle-in-cell simulations compromised by monte carlo collisions", *Physics of Plasmas*, vol. 13, no. 3, p. 033 506, 2006. DOI: `10.1063/1.2169752`. eprint: `https://doi.org/10.1`

063/1.2169752. [Online]. Available: https://doi.org/10.1063/1.2169752.

[113] V. Vahedi, G. DiPeso, C. K. Birdsall, M. A. Lieberman, and T. D. Rognlien, "Capacitive rf discharges modelled by particle-in-cell monte carlo simulation. i. analysis of numerical techniques", *Plasma Sources Science and Technology*, vol. 2, no. 4, p. 261, Nov. 1993. DOI: 10.1088/0963-0252/2/4/006. [Online]. Available: https://dx.doi.org/10.1088/0963-0252/2/4/006.

[114] H. Karimabadi, J. Driscoll, Y. Omelchenko, and N. Omidi, "A new asynchronous methodology for modeling of physical systems: breaking the curse of courant condition", *Journal of Computational Physics*, vol. 205, no. 2, pp. 755–775, 2005, ISSN: 0021-9991. DOI: https://doi.org/10.1016/j.jcp.2004.12.003. [Online]. Available: https://www.sciencedirect.com/science/article/pii/S0021999104004917.

[115] H. Okuda and C. K. Birdsall, "Collisions in a plasma of finite-size particles", *The Physics of Fluids*, vol. 13, no. 8, pp. 2123–2134, 1970. DOI: 10.1063/1.1693210. eprint: https://aip.scitation.org/doi/pdf/10.1063/1.1693210. [Online]. Available: https://aip.scitation.org/doi/abs/10.1063/1.1693210.

[116] A. B. Langdon and C. K. Birdsall, "Theory of plasma simulation using finite-size particles", *The Physics of Fluids*, vol. 13, no. 8, pp. 2115–2122, 1970. DOI: 10.1063/1.1693209. eprint: https://aip.scitation.org/doi/pdf/10.1063/1.1693209. [Online]. Available: https://aip.scitation.org/doi/abs/10.1063/1.1693209.

[117] H. Okuda, "Verification of theory for plasma of finite-size particles", *The Physics of Fluids*, vol. 15, no. 7, pp. 1268–1274, 1972. DOI: 10.1063/1.1694076. eprint: https://aip.scitation.org/doi/pdf/10.1063/1.1694076. [Online]. Available: https://aip.scitation.org/doi/abs/10.1063/1.1694076.

[118] K. Nanbu, "Probability theory of electron-molecule, ion-molecule, molecule-molecule, and coulomb collisions for particle modeling of materials process-

ing plasmas and cases”, *IEEE Transactions on plasma science*, vol. 28, no. 3, pp. 971–990, 2000.

[119] L. Ding, M. Sudakov, and S. Kumashiro, “A simulation study of the digital ion trap mass spectrometer”, *International Journal of Mass Spectrometry*, vol. 221, no. 2, pp. 117–138, 2002, ISSN: 1387-3806. DOI: `https://doi.org/10.1016/S1387-3806(02)00921-1`. [Online]. Available: `https://www.sciencedirect.com/science/article/pii/S1387380602009211`.

[120] V. Vahedi and M. Surendra, “A monte carlo collision model for the particle-in-cell method: applications to argon and oxygen discharges”, *Computer Physics Communications*, vol. 87, no. 1, pp. 179–198, 1995, Particle Simulation Methods, ISSN: 0010-4655. DOI: `https://doi.org/10.1016/0010-4655(94)00171-W`. [Online]. Available: `https://www.sciencedirect.com/science/article/pii/001046559400171W`.

[121] A. Okhrimovskyy, A. Bogaerts, and R. Gijbels, “Electron anisotropic scattering in gases: a formula for monte carlo simulations”, *Phys. Rev. E*, vol. 65, p. 037 402, 3 Feb. 2002. DOI: `10.1103/PhysRevE.65.037402`. [Online]. Available: `https://link.aps.org/doi/10.1103/PhysRevE.65.037402`.

[122] C. B. Opal, W. K. Peterson, and E. C. Beaty, “Measurements of secondary-electron spectra produced by electron impact ionization of a number of simple gases”, *The Journal of Chemical Physics*, vol. 55, no. 8, pp. 4100–4106, 1971. DOI: `10.1063/1.1676707`. eprint: `https://doi.org/10.1063/1.1676707`. [Online]. Available: `https://doi.org/10.1063/1.1676707`.

[123] K. Koura, “Null-collision technique in the direct-simulation monte carlo method”, *The Physics of Fluids*, vol. 29, no. 11, pp. 3509–3511, 1986. DOI: `10.1063/1.865826`. eprint: `https://aip.scitation.org/doi/pdf/10.1063/1.865826`. [Online]. Available: `https://aip.scitation.org/doi/abs/10.1063/1.865826`.

[124] M. Brennan, "Optimization of monte carlo codes using null collision techniques for experimental simulation at low e/n", *IEEE Transactions on Plasma Science*, vol. 19, no. 2, pp. 256–261, 1991. DOI: `10.1109/27.106822`.

[125] *Phelps database*, Retrieved: 05/11/2021. [Online]. Available: `www.lxcat.net`.

[126] J. Doke. "Grabit matlab central file exchange". (), [Online]. Available: `https://www.mathworks.com/matlabcentral/fileexchange/7173-grabit`. Retrieved on November 5, 2021.

[127] "Capacitive discharges", in *Principles of Plasma Discharges and Materials Processing*. John Wiley & Sons, Ltd, 2005, ch. 11, pp. 387–460, ISBN: 9780471724254. DOI: `https://doi.org/10.1002/0471724254.ch11`. eprint: `https://onlinelibrary.wiley.com/doi/pdf/10.1002/0471724254.ch11`. [Online]. Available: `https://onlinelibrary.wiley.com/doi/abs/10.1002/0471724254.ch11`.

[128] T. Makabe and Z. Petrovic, *Plasma Electronics: Applications in Microelectronic Device Fabrication*, First Edition. CRC Press, 2006. DOI: `https://doi.org/10.1201/9781420012279`.

[129] A. Quraishi and I. Kronhaus, "Modelling of capillary capacitively coupled radio frequency thruster", *Journal of Physics D: Applied Physics*, vol. 54, no. 42, p. 425 201, Aug. 2021. DOI: `10.1088/1361-6463/ac16a5`. [Online]. Available: `https://dx.doi.org/10.1088/1361-6463/ac16a5`.

[130] L. L. Alves and L. Marques, "Fluid modelling of capacitively coupled radiofrequency discharges: a review", *Plasma Physics and Controlled Fusion*, vol. 54, no. 12, p. 124 012, Nov. 2012. DOI: `10.1088/0741-3335/54/12/124012`. [Online]. Available: `https://dx.doi.org/10.1088/0741-3335/54/12/124012`.

[131] M. M. Becker, H. Kählert, A. Sun, M. Bonitz, and D. Loffhagen, "Advanced fluid modeling and pic/mcc simulations of low-pressure ccrf discharges", *Plasma Sources Science and Technology*, vol. 26, no. 4, p. 044 001, Mar. 2017. DOI: `10.1088/1361-6595/aa5cce`. [Online]. Available: `https://dx.doi.org/10.1088/1361-6595/aa5cce`.

[132] E. Kawamura, C. K. Birdsall, and V. Vahedi, “Physical and numerical methods of speeding up particle codes and paralleling as applied to rf discharges”, *Plasma Sources Science and Technology*, vol. 9, no. 3, p. 413, Aug. 2000. DOI: `10.1088/0963-0252/9/3/319`. [Online]. Available: `https://dx.doi.org/10.1088/0963-0252/9/3/319`.

[133] T. Lafleur and R. W. Boswell, “Particle-in-cell simulations of hollow cathode enhanced capacitively coupled radio frequency discharges”, *Physics of Plasmas*, vol. 19, no. 2, p. 023 508, 2012. DOI: `10.1063/1.3685709`. eprint: `https://doi.org/10.1063/1.3685709`. [Online]. Available: `https://doi.org/10.1063/1.3685709`.

[134] A. Quraishi, O. Hamo, and I. Kronhaus, “Plasma simulation benchmark for ccrf discharge with secondary electron emission”, *IEEE Transactions on Plasma Science*, vol. 48, no. 1, pp. 109–118, 2020. DOI: `10.1109/TPS.2019.2958972`.

[135] J. Schulze, E. Schüngel, Z. Donkó, and U. Czarnetzki, “Charge dynamics in capacitively coupled radio frequency discharges”, *Journal of Physics D: Applied Physics*, vol. 43, no. 22, p. 225 201, May 2010. DOI: `10.1088/0022-3727/43/22/225201`. [Online]. Available: `https://dx.doi.org/10.1088/0022-3727/43/22/225201`.

[136] A. V. Phelps, “The application of scattering cross sections to ion flux models in discharge sheaths”, *Journal of Applied Physics*, vol. 76, no. 2, pp. 747–753, 1994. DOI: `10.1063/1.357820`. eprint: `https://doi.org/10.1063/1.357820`. [Online]. Available: `https://doi.org/10.1063/1.357820`.

[137] V. A. Godyak and R. B. Piejak, “Abnormally low electron energy and heating-mode transition in a low-pressure argon rf discharge at 13.56 mhz”, *Phys. Rev. Lett.*, vol. 65, pp. 996–999, 8 Aug. 1990. DOI: `10.1103/PhysRevLett.65.996`. [Online]. Available: `https://link.aps.org/doi/10.1103/PhysRevLett.65.996`.

[138] C. Wild and P. Koidl, “Ion and electron dynamics in the sheath of radio-frequency glow discharges”, *Journal of Applied Physics*, vol. 69, no. 5, pp. 2909–2922, 1991. DOI: `10.1063/1.348601`. eprint: `https://doi`

.org/10.1063/1.348601. [Online]. Available: https://doi.org/10.1063/1.348601.

[139] E. Schüngel, Z. Donkó, and J. Schulze, “A simple model for ion flux-energy distribution functions in capacitively coupled radio-frequency plasmas driven by arbitrary voltage waveforms”, *Plasma Processes and Polymers*, vol. 14, no. 4-5, p. 1 600 117, 2017. DOI: https://doi.org/10.1002/ppap.201600117. eprint: https://onlinelibrary.wiley.com/doi/pdf/10.1002/ppap.201600117. [Online]. Available: https://onlinelibrary.wiley.com/doi/abs/10.1002/ppap.201600117.

[140] J. Schulze, Z. Donkó, B. G. Heil, *et al.*, “Electric field reversals in the sheath region of capacitively coupled radio frequency discharges at different pressures”, *Journal of Physics D: Applied Physics*, vol. 41, no. 10, p. 105 214, May 2008. DOI: 10.1088/0022-3727/41/10/105214. [Online]. Available: https://dx.doi.org/10.1088/0022-3727/41/10/105214.

[141] V. A. Godyak, R. B. Piejak, and B. M. Alexandrovich, “Measurement of electron energy distribution in low-pressure RF discharges”, *Plasma Sources Science and Technology*, vol. 1, no. 1, pp. 36–58, Mar. 1992. DOI: 10.1088/0963-0252/1/1/006. [Online]. Available: https://doi.org/10.1088/0963-0252/1/1/006.

[142] S. F. Biagi, *Biagi-v7.1 database*, Cross sections extracted from PROGRAM MAGBOLTZ, VERSION 7.1, retrieved from www.lxcat.net on March 13, 2022., Jun. 2004.

[143] A. V. Phelps, *Phelps database*, Retrieved from www.lxcat.net on March 13, 2022.